Democratic and Popular Republic of Algeria
Ministry of Higher Education and Scientific Research

Larbi TebessiUniversity, Tebessa, Algeria

Faculty of Exact Sciences and Science of Nature and Life
Department of Material Sciences

Thesis

Presented to obtain the degree of

Doctorate

Option:Physics of Materials.

Entitled:

Study of Physical Properties of Transition MetalsDieselenides of the SixthColomn.

Presentedby:
BRADJI Bouthaina

In front of the Jury committeecomposedof:

CHEMAM Faïçal	Professor	University of Tebessa	President
BENKHEDIR Mohammed Loutfi	Professor	University of Tebessa	Supervisor
CHAOUCHE Yassine	Professor	University of Tebessa	Examiner
ROUAG Nouari	Professor	University of Setif 1	Examiner

Defense date : July 14, 2025

Dedication

I would like to dedicate this work:

To my dear parents,

To my beloved husband, his family, and

my precious children,

To my cherished sisters and brothers,

To all my relatives and neighbors,

And to all my friends and colleagues,

With deep gratitude and affection.

BRADJI Bouthaina

Acknowledgements

This doctoral thesis was carried out at the Laboratory of Theoretical and Applied Physics (LPAT), Department of Physics, Faculty of Exact and Natural Sciences, University of Tébessa.

First and foremost, I would like to thank Almighty God for granting me the strength, patience, and determination to complete this work under the best possible conditions.

I express my sincere gratitude to my supervisor, ***Professor BENKHEDIR Mohammed Loutfi***, for their valuable guidance, continuous support, and insightful advice throughout this research.

My heartfelt thanks go to ***Professor BOUHELAL Mouna*** Director of the LPAT laboratory, for her encouragement and support during the completion of this work.

I would also like to warmly thank ***Professor BOUMAALI Abdelmalek***, Director of the research project, for his trust and scientific guidance.

Special thanks are due to ***Professor CHEMAM Faïçal***, who directed the LPAT laboratory for several years and served as the President of the thesis jury. His expertise, kindness, and critical evaluation have been of great importance to this work.

I am also very grateful to all the members of the jury ***Professor CHAOUECH Yassine*** of Tebessa University and ***Professor ROUAG Nouari*** of Setif University for their time, thoughtful comments, and valuable suggestions.

Finally, I express my sincere thanks to all my, family, friends, colleagues, and to everyone who helped me to accomplish this research work.

Abstract

We use first-principles calculations based on Density Functional Theory (DFT) to analyze the structural, electronic, and optical properties of a $MoSe_2$ monolayer, one of the prominent two-dimensional transition metal dichalcogenides (TMDCs) belonging to group VI of the periodic table. Our research focuses on both the pristine material and its behavior under various types of defects, such as a molybdenum vacancy, arsenic substitution at a Mo site, and arsenic interstitial doping.

To our knowledge, this work represents the first theoretical study of the latter two defects. The **Quantum ESPRESSO** package was used to perform the computations, employing the plane-wave pseudopotential approach.

To better understand the impact of these defects, we investigated structural optimization, formation energy, band structure, density of states, difference charge density, and a range of optical properties including dielectric function, refractive index, extinction coefficient, reflectivity, absorption coefficient, optical conductivity, and energy loss function. The study found that defect engineering significantly alters the electronic properties of $MoSe_2$, such as the band gap and the electronic states near the Fermi level. It also introduces localized states and causes shifts in various optical spectra, suggesting potential applications in optoelectronic devices.Moreover, our results are in good agreement with previously reported theoretical and experimental studies, which further validates the reliability of our findings. This study sheds light on the tunability of 2D TMDC materials through controlled defect introduction.

Keywords :TMDCs, $MoSe_2$ monolayer, 2D materials, Arsenic doping, DFT, Quantum ESPRESSO, Electronic properties, Optical properties, Optoelectronic applications.

Résumé

Nous utilisons des calculs ab initio basés sur la théorie de la fonctionnelle de la densité (DFT) pour analyser les propriétés structurelles, électroniques et optiques d'une monocouche de $MoSe_2$, l'un des dichalcogénures de métaux de transition (TMDCs) bidimensionnelsde la sixième colonne.

Notre étude porte à la fois sur le matériau parfait et sur son comportement en présence de différents types de défauts, tels qu'une vacance de molybdène, une substitution du molybdène par de l'arsenic, et un dopage interstitiel par l'arsenic. À notre connaissance, ce travail constitue la première étude théorique des deux derniers défauts.

Les calculs ont été effectués à l'aide du logiciel **Quantum ESPRESSO** selon l'approche des pseudopotentiels et des ondes planes. Afin de mieux comprendre l'effet de ces défauts, nous avons étudié l'optimisation structurale, l'énergie de formation, la structure de bande, la densité d'états, la densité de charge différentielle ainsi qu'un ensemble de propriétés optiques, notamment la fonction diélectrique, l'indice de réfraction, le coefficient d'extinction, la réflectivité, le coefficient d'absorption, la conductivité optique et la fonction de perte d'énergie.L'étude a révélé que l'ingénierie des défauts modifie considérablement les propriétés électroniques du $MoSe_2$, telles que la largeur de bande et les états électroniques proches du niveau de Fermi. Elle introduit également des états localisés et provoque un décalage dans les spectres des propriétés optiques, suggérant des applications potentielles dans les dispositifs optoélectroniques. De plus, nos résultats sont en bon accord avec les études théoriques et expérimentales précédentes, ce qui confirme la fiabilité de nos conclusions. Cette étude met en lumière la possibilité de moduler les propriétés des matériaux TMDC 2D par une introduction contrôlée de défauts.

Mots clés : TMDCs, Monocouche de $MoSe_2$,Matériaux 2D, Dopage à l'arsenic, DFT , Quantum ESPRESSO, Propriétés électroniques, Propriétés optiques, Applications optoélectroniques.

الملخص

نستخدم *حسابات المبدأ الأول المعتمد* على نظرية دالة الكثافة (DFT) لتحليل الخصائص البنيوية، الإلكترونية، والبصرية للطبقة الأحادية من $MoSe_2$ ، وهو أحد ثنائيات كالكوجينيد المعادن الانتقالية (TMDCs) ثنائية الأبعاد المنتمية إلى عناصر المجموعة السادسة في الجدول الدوري. تركز دراستنا على المادة في حالتها المثالية، بالإضافة إلى سلوكها في وجود أنواع مختلفة من العيوب مثل شغرة ذرة الموليبدينوم، استبدال ذرة الموليبدينوم بذرة زرنيخ، والإقحام البيني لذرة زرنيخ. وبحسب علمنا، يمثل هذا العمل أول دراسة نظرية لهذين العيبين الأخيرين .تم إجراء الحسابات باستخدام برنامج**Quantum ESPRESSO**وفق نهج الموجات المستوية والجهد الكاذب.

لفهم تأثير هذه العيوب بشكل أعمق، قمنا بدراسة تحسين البنية، طاقة التكوين، بنية النطاق، كثافة الحالات، كثافة الشحنة الفرقية، ومجموعة من الخصائص البصرية التي تشمل: دالة العزل الكهربائي، معامل الانكسار، معامل الانقراض، الانعكاسية، معامل الامتصاص، التوصيلية البصرية، ودالة فقدان الطاقة.كشفت الدراسة أن هندسة العيوب تؤثر بشكل كبير على الخصائص الإلكترونية لـ**$MoSe_2$**، مثل فجوة الطاقة والحالات الإلكترونية القريبة من مستوى فيرمي.

كما تؤدي إلى ظهور حالات موضعية وتتسبب في انزياحات في أطياف الخصائص البصرية، مما يشير إلى إمكانية استخدامها في تطبيقات الأجهزة البصرية والإلكترونية. علاوة على ذلك، تتفق نتائجنا بشكل جيد مع الدراسات النظرية والتجريبية السابقة، مما يعزز من موثوقية الاستنتاجات المتوصَّل إليها. تسلط هذه الدراسة الضوء على إمكانية تعديل خصائص مواد TMDC ثنائية الأبعاد من خلال إدخال العيوب بشكل محكوم.

الكلمات المفتاحية: TMDCs، الطبقة الأحادية من$MoSe_2$ ، المواد ثنائية الأبعاد، تطعيم الزرنيخ، DFT، Quantum ESPRESSO، الخصائص الإلكترونية، الخصائص البصرية، التطبيقات البصرية والإلكترونية

Sommaire

Dedication.....I

Acknowledgements.....II

Abstract.....III

Résumé.....IV

الملخص.....V

Sommaire.....I

Liste of Figures.....I

Listeof tables.....I

General Introduction.....1

References.....5

CHAPTER I:

General Information on the Materials Studied

I-1-Introduction:.....8

I-2- Structure ofTransition Metal Dichalcogenide (TMDCs):.....8

I-2-1- Transition Metal Dieselenide of the Sixth Column:.....10

I-3- Fabrication of 2D TMDCs from Bulk Structure:.....10

I-3-1- Top-Down Methods:.....10

I-3-2- Bottom-Up Techniques:.....13

I-4- The band gap (Eg):.....16

I-4-1- Direct and indirect bandgap in semiconductor:.....16

I-4-2-Direct and Indirect Transitions:.....17

I-5- Point Defects:.....18

1-5-1-Vacancies :.....18

1-5-2-Interstitials:.....19

1-5-3- Antisite Defects:.....19

I-5-4- Substitute Atoms:.....19

I-6- Semiconductor Doping :.....19

I-6-1- n-Type Doping:.....20

I-6-2- p-Type Doping:.....20

1-7- Doping in 2D TMDC Monolayer Materials:.....21

I-8- Application of 2D TMDCs:.....22

I-8-1- Field-Effect Transistor (FET):.....22

I-8-2- Optoelectronic Applications:.....23

I-8-3- Energy Storage:.....26

I-8-4- Catalyst for Hydrogen Evolution Reaction (HER): **28**
I-8-5- Chemical Gas Sensors: **29**
I-8-6- Biomedical Applications: **30**
I-9- $MoSe_2$ Monolayer and Arsenic Doping: General Overview and Scientific Motivation : **31**
References: **33**

CHAPTER II:

Computational Methods

II-1-Introduction: **41**
II-2- Total Hamiltonian for the Crystal: **41**
II-3- Born-Oppenheimer Approximation: **42**
II-4- Hartree-Fock Approximation: **42**
II-5-Density Functional Theory (DFT): **44**
II-5-1-Thomas-Fermi Model: **44**
II-5-2- Dirac Model: **44**
II-5-3- Theorems of Hohenberg and Kohn: **45**
II-5-4- Kohn-Sham Equations **46**
II-5-5-Solutions of Kohn-Sham Equations **47**
II-5-6- Functional Exchange-Correlation: **48**
II-5-6-1- Local Density Approximation (LDA): **48**
II-5-6-2-Generalized Gradient Approximation (GGA) : **49**
II-5-5-1-a- Approximation PBE-GGA: **50**
II-6- The Plane Wave (PW): **50**
II-7-Pseudopotential Approximation: **51**
II-7-1- Norm-Conserving Pseudopotential (NC) **53**
II-7-2- Ultra-Soft Pseudopotential (US): **53**
II-7-3-Projected pseudo-potential PAW (Projector Augmented Wave): **53**
II-8- Plan Wave-Pseudopotential (PW-PP): **54**
II-9- Calculation Code: **54**
II-9-1- Structure of the Input Data in QUANTUM ESPRESSO Software: **56**
References: **59**

CHAPTER III :

Results and Discussion

III-1-Introduction **65**
III-2- Computational Details **65**
III-2- Test of Convergence: **66**
III-3- Structural Properties : **67**

III-4-Formation Energy of Structures with Defects:.....70
III-5- Electronic Properties:.....72
III-5-1-Band Structures.....72
III-5-2- Density of State and Partial Density of States (DOS and PDOS) 75
III-5-**3- Difference Charge Density.....80**
III-6- Optical Properties.....83
Conclusion 110

Liste of Figures

Figure I.1: Representation of TMDCs in periodic table, where the orange and yellow elements represent the metals and chalcogenes, respectively, that form TMDC materials. 9

Figure I.2: three-dimensional representation of a typical layered MX_2 structure, where green and purple spheres present M (metal) atoms and orange balls present X (chalcogene) atoms. 9

Figure I.3 : polytypes of lamellar TMDCs 10

Figure I.4: Schematic of mechanical exfoliation process for 2D materials using Scotch tape technique 11

Figure I.5 : Schematic representation of the main liquid exfoliation mechanisms, where (a), (b), and (c) correspond to ion intercalation, ion exchange, and ultrasonication exfoliation, respectively 12

Figure I.6: (a) Experimental setup for electrochemical exfoliation of bulk MoS_2 crystal, (b) Schematic presentation of the electrochemical exfoliation of bulk MoS_2 13

Figure I.7: Schematic illustration of the synthesis of TMDC monolayers via PVD method. 14

FigureI.8: Schematics of various methods used in TMD technology based on the CVD method in the gas phase, ...15

Figure I.9: Direct Band-Gap Semiconductor and indirect Band-Gap Semiconductor. 17

Figure I.10: Schematic showing (a) direct gap transition and (b) indirect gap transition. 18

Figure I.11: Types of point defects in crystals. 19

Figure I.12: Band structure for (a) n-type doping and (b) p-type doping.....20

Figure I.14 :(a) MoS_2-based FET, (b) Schematic representation of a MoS_2 –based FET 23

Figure I.15 :(a) Schematic illustrationofa monolayer $MoSe_2$-basedphototransistor exposed to a laser beam, (b) Schematic showing of the impact of incident photons on a multilayer MoS2-based phototransistor (n-channel) 24

Figure I.16 :(a) Schematic of a WSe_2-based solar cell, (b) photoluminescence spectrum of WSe_2-based solar cell, (c) variation of bias voltage (V) as a function of current (nA) in the dark , (d) the variation of bias voltage (V) as a function of current (n nA) under optical illumination 26

Figure I.17 : Schematic representation of HER mechanism in acidic and alkaline solutions 29

Figure I.18: Schematic represontation of the gas sensing mechanism in a MoS_2-based sensor,.....30

Figure I.19: various biomedical applications of TMDC nanoparticules. 31

Figure II.1: Schematic representation of the self-consistency cycle in Kohn-Sham density functional theory calculations. 48

Figure II-2: Schematic illustration of the pseudopotential concept, where ψ^{PS} , ψ^{AE} , , VPS , VAE and rcut corresponding the pseudo-wavefunction, all electron-wavefunction, pseudo-potential, all electron-potential and the cutoff radius, respectively. 52

Figure II-3: Schematic diagram of the QUANTUM ESPRESSO algorithm.....58

Figure III .1 : Convergence test of the total energy as a function of the number of k-points in the first Brillouin zone.....66

Figure III .2 : Convergence test of the total energy as a function of ecutoff energy.....67

Figure III. 3 : the structure of $MoSe_2$ monolayer where (a) top view of the supercelle, (b) side view of the supercell and (c) is the premative structure, the atom of Selenuim are shown with yellow and of the molebden with green.....68

Figure III .4: Variation of total energy as a function of volume for the primitive monolayer MoSe2...69

Figure III-5: Structure of the $MoSe_2$ monolayer supercell: (a) pristine structure, (b) As (Mo)-doped structure, (c) Mo vacancy, and (d) interstitial As. 70

Figure III-6: band structure of the primitive structure of MoSe2 where : (a) for bulk structure and (b) for a monolayer structure. 73

Figure III-7 :Band structure of (a) pure MoSe2 monolayer, (b) As(Mo)-doped structure, (c) Mo vacancy structure, and (d) As interstitial structure. 74

Figure III-8 : Density of states (DOS) and partial density of states (PDOS) of the pristine MoSe2 monolayer structure. 75

Figure III-9 : Density of states (DOS) and partial density of states (PDOS) of the As(Mo) doped structure.....76

Figure III-10 : Density of states (DOS) and partial density of states (PDOS) of the Mo vacancy structure.....76

Figure III-11 : Density of states (DOS) and partial density of states (PDOS) of the As interstitial structure.....77

Figure III-12 : Partial density of states (PDOS) in the As (Mo) doped system for: (a) Mo atom near the As position, (b) Se atom near the As position, (c) substitutional As atom, and (d) comparison of all previous cases.....77

Figure III-13 :Partial density of states (PDOS) in the As interstitial system for: (a) Mo atoms near the interstitial As, (b) Se atoms near the interstitial As, (c) interstitial As atom, and (d) comparison of all previous cases.....78

Figure III-14 :The distribution of electronic charge density isosurfaces of pure $MoSe_2$, where the blue regions represent electron depletion (loss of electrons), and the yellow regions indicate electron accumulation. 81

Figure III-15 :Electronic charge density difference of (a) the As(Mo)-doped system, (b) the Mo vacancy system, and (c) the interstitial As system. The blue regions represent electron depletion, while the yellow regions indicate electron accumulation. 82

Figure III-16 : Real part of the dielectric function for (a) the pristine MoSe2 monolayer structure, (b) the As(Mo) doped structure, (c) the Mo vacancy structure, and (d) the As interstitial structure. 86

Figure III-17 : Imaginary part of the dielectric function for (a) the pristine $MoSe_2$ monolayer structure, (b) the As(Mo)-doped structure, (c) the Mo vacancy structure, and (d) the interstitial As structure.....89

Figure III-18 : Refractive index as a function of photon energy for (a) pure $MoSe_2$ monolayer structure, (b) As(Mo)-doped structure, (c) Mo vacancy structure, and (d) As interstitial structure. 91

Figure III-19 : Extinction index as a function of photon energy of (a) pure $MoSe_2$ monolayer structure, (b) As(Mo)-doped structure, (c) Mo vacancy structure, and (d) As interstitial structure.....93

Figure III-20 : Reflectivity of : (a) pure $MoSe_2$ monolayer structure, (b) doped As(Mo) structure, (c) Mo vacancy structure and (d) As interstitial structure. 95

Figure III-21 : Absorption coefficient of : (a) pure $MoSe_2$ monolayer structure, (b) doped As(Mo) structure, (c) Mo vacancy structure (d) As Interstitial structure. 98

Figure III-22 : Optical conductivity of : (a) pure $MoSe_2$ monolayer structure, (b) doped As(Mo) structure, (c) Mo vacancy structure (d) As interstitial structure. 101

Figure III-23 : Energy loss function of : (a) pure $MoSe_2$ monolayer structure, (b) doped As(Mo) structure, (c) Mo vacancy structure (d) As interstitial. 102

Listeof tables

Table III.1: Structural parameters of 2H-$MoSe_2$, including the lattice constants a (A°) and c (A°), the monolayer thickness d_{Mo-Mo}(A°), and the bond length d_{Mo-Se}(A°).....68

Table III- 2: Chemical potentials of Mo, Se and As atoms expressed in (Ry). 71

Table III- 3: Formation energies of different structures under Se-rich conditions in (eV). 71

Table III-4: Energy gap values of bulk MoSe2 and its monolayer. 72

Table III-5 : band gap of different structures in (eV). 75

Table III-5: Static Dielectric Constant in the (xx), (yy) and (zz) directions.....87

Table III-6 : Maximum values of and their corresponding energies in the (xx), (yy) and (zz) directions.....87

Table III-7 : Maximum values of and their corresponding energies in the (xx), (yy) and (zz) directions.....89

Table III-8 : Maximum values for refractive index and their corresponding energies in the (xx), (yy) and (zz) directions.....92

Table III-9 : Maximum values of and their corresponding energies in the (xx), (yy) and (zz)directions.....94

Table III-10 : Static reflectivity , maximum values of and their corresponding energies in the (xx), (yy) and (zz) directions.....96

Table III-11 : The absorption edge (threshold) in the (xx), (yy) and (zz) directions and the Energy gap (eV). 99

Table III-12 : Maximum values of and their corresponding energies in the (xx), (yy) and (zz) directions.....100

Table III-13 : Maximum values of and their corresponding energies in the directions (xx), (yy) and (zz).....101

General Introduction

General Introduction

Since the groundbreaking work of Novoselov et al., which led to the 2010 Nobel Prize for the successful exfoliation of graphene in 2004[1], there has been a growing interest in graphene and other layered materials due to their distinctive structural and electronic properties [2][3].

Graphene, in particular, exhibits exceptionally high carrier mobility and extremely low resistivity at room temperature. However, its zero bandgap restricts its applications in electronic and optoelectronic devices[4].

Additionally, graphene has limitations in energy storage applications, such as low volumetric energy density and high initial irreversible capacity, which pose challenges in lithium-ion battery technology[5].

These constraints have led researchers to explore alternative two-dimensional (2D) materials with more tunable properties.

Among the promising 2D material candidates are transition metal dichalcogenides (TMDCs), which exhibit remarkable characteristics. TMDCs follow the general formula MX_2, where M represents a transition metal and X is a chalcogen[6].

Structurally, they possess a honeycomb arrangement similar to graphene when viewed from above but with a layered composition in which the transition metal atoms are sandwiched between two chalcogen layers[7].

These materials display diverse electronic behaviors, ranging from semiconducting (e.g., $MoSe_2$, MoS_2, WSe_2, WS_2) to metallic (e.g., TiS_2, VSe_2) and even superconducting properties (e.g., TaS_2, NbS_2)[8].

Such versatility makes TMDCs highly attractive for electronic and optoelectronic applications, especially semiconducting materials.

To enhance the physical properties of these materials and expand their potential applications, recent studies have focused extensively on the impact of point defects in semiconducting TMDCs.

A key feature of TMDCs is the tunability of their bandgap, which can be modified by factors such as layer thickness, strain, and chemical doping[9].

Chemical doping, in particular, plays a crucial role in tailoring material properties. It can occur through substitutional doping (where foreign atoms replace host atoms) or metastable doping (such as interstitial incorporation).

Metastable doping can be intentional or unintentional, influenced by environmental factors such as substrate interactions, metal contacts, and humidity[10].

While most studies focus on MoS_2, molybdenum diselenide$MoSe_2$ has gained significant attention due to its similar structure to MoS_2 but with intriguing properties and potential applications. This material exists in three primary phases: trigonal prismatic (2H), trigonal (3R), and octahedral (1T).

While the 2H and 3R phases exhibit semiconducting behavior, the 1T phase is metallic[11].

Furthermore, $MoSe_2$propertiescan be engineered through doping with transition metals, chalcogens, or other elements. In this work, we selected arsenic (As) as a dopant due to its potential to form new bonds with molybdenum and selenium atoms and its relatively small atomic size compared to molybdenum. We also examined the effect of Mo vacancies and compared them with arsenic substitution.

Generally, 2D TMDCs can be synthesized from their bulk counterparts using various experimental techniques, primarily categorized into top-down and bottom-up approaches[12].

Additionally, these materials can be studied through theoretical simulations, which offer a cost-effective and precise way to investigate their fundamental properties.

Density Functional Theory (DFT) serves as a first-principles computational framework for systematically investigating the structural, electronic, and optical properties of materials[13].

To enhance the accuracy and efficiency of the calculations, the plane-wave pseudopotential (PP-PW) approach, as implemented in the Quantum ESPRESSO package, is widely used for electronic structure calculations.

The pseudopotential approximation significantly reduces computational complexity by replacing the all-electron problem with an effective potential that accounts for core-electron interactions, enabling efficient calculations while preserving accuracy[14]. To achieve reliable electronic structure calculations, the selection of an appropriate exchange-correlation functional is crucial.

The Generalized Gradient Approximation (GGA), particularly the Perdew–Burke–Ernzerhof (PBE) functional, is commonly used as it offers a reasonable balance between computational cost and accuracy.

Additionally, a plane-wave basis set with a well-converged kinetic energy cutoff is typically employed.

The Brillouin zone is sampled using a Monkhorst-Pack k-point mesh to ensure proper convergence of the calculations.

This thesis aims to provide a deeper understanding of $MoSe_2$'s structural, electronic, and optical properties, particularly in the presence of defects and dopants, with implications for its integration into future nanoelectronic and optoelectronic devices.

To achieve these goals, the thesis is organized as follows:

- **Chapter 1**: Provides an overview of TMDCs, their properties, and the chemical methods used to synthesize 2D materials, as well as their potential applications.
- **Chapter 2**: Describes the computational methodology, including the implementation of DFT, the theoretical background, and the PP-PW approach within the Quantum ESPRESSO package.
- **Chapter 3**: Presents and discusses the results obtained for the structural, electronic, and optical properties of 2D $MoSe_2$ and investigates the effects of intrinsic defects on these properties. The defectsstudiedare:
  - Substitution of a Mo atom with an arsenic (As) atom.
  - A Mo vacancy structure, where a molybdenum atom is removed.
  - An interstitial As structure, where an arsenic (As) atom is positioned at the center of the hexagonal cell.

Finally, we compare our results with theoretical and experimental studies available in the literature. This work concludes with a general summary highlighting the principal results obtained.

References:

[1] A. H. Castro Neto, F. Guinea, N. M. R. Peres, K. S. Novoselov, and A. K. Geim, "The electronic properties of graphene," *Rev. Mod. Phys.*, vol. 81, no. 1, pp. 109–162, Jan. 2009, doi: 10.1103/RevModPhys.81.109.

[2] S. Haldar, H. Vovusha, M. K. Yadav, O. Eriksson, and B. Sanyal, "Systematic study of structural, electronic, and optical properties of atomic-scale defects in the two-dimensional transition metal dichalcogenides," *Phys. Rev. B*, vol. 92, no. 23, p. 235408, Dec. 2015, doi: 10.1103/PhysRevB.92.235408.

[3] J. T. Paul *et al.*, "Computational methods for 2D materials: discovery, property characterization, and application design," *J. Phys. Condens. Matter*, vol. 29, no. 47, p. 473001, Nov. 2017, doi: 10.1088/1361-648X/aa9305.

[4] K. S. Novoselov *et al.*, "Electric Field Effect in Atomically Thin Carbon Films," *Science (80-.).*, vol. 306, no. 5696, pp. 666–669, Oct. 2004, doi: 10.1126/science.1102896.

[5] A. Kausar, I. Ahmad, and T. D. Lam, "Graphene footprints in energy storage systems—An overview," *e-Prime - Adv. Electr. Eng. Electron. Energy*, vol. 6, p. 100361, Dec. 2023, doi: 10.1016/j.prime.2023.100361.

[6] J. Luxa, V. Mazánek, and Z. Sofer, "Transition Metal Dichalcogenides: Properties, Synthetic Routes and Applications," in *Concepts and Design of Materials Nanoarchitectonics*, The Royal Society of Chemistry, 2022, pp. 417–441. doi: 10.1039/9781788019613-00417.

[7] H. Terrones and M. Terrones, "Bilayers of transition metal dichalcogenides: Different stackings and heterostructures," *J. Mater. Res.*, vol. 29, no. 3, pp. 373–382, Feb. 2014, doi: 10.1557/jmr.2013.284.

[8] R. R. Nair *et al.*, "Fine Structure Constant Defines Visual Transparency of Graphene," *Science (80-.).*, vol. 320, no. 5881, pp. 1308–1308, Jun. 2008, doi:10.1126/science.1156965.

[9] A. V. Kolobov and J. Tominaga, "From 3D to 2D: Fabrication Methods," 2016, pp. 79–107. doi: 10.1007/978-3-319-31450-1_4.

[10] K. Zhang and J. Robinson, "Doping of Two-Dimensional Semiconductors: A Rapid Review and Outlook," *MRS Adv.*, vol. 4, no. 51–52, pp. 2743–2757, Oct. 2019, doi: 10.1557/adv.2019.391.

[11] Z. H. Khan, Ed., *Emerging Trends in Nanotechnology*. Singapore: Springer Singapore, 2021. doi: 10.1007/978-981-15-9904-0.

[12] J. Wang *et al.*, "Controlled growth of atomically thin transition metal dichalcogenides via chemical vapor deposition method," *Mater. Today Adv.*, vol. 8, p. 100098, Dec. 2020, doi: 10.1016/j.mtadv.2020.100098.

[13] D. Glossman-Mitnik, Ed., *Density Functional Theory - Recent Advances, New Perspectives and Applications*. IntechOpen, 2022. doi: 10.5772/intechopen.95698.

[14] "Atoms with plane waves: accurate pseudopotentials," in *Ab Initio Molecular Dynamics*, Cambridge University Press, 2009, pp. 136–174. doi: 10.1017/CBO9780511609633.005.

CHAPTER I:

General Information on the Materials Studied

I-1-Introduction:

After the scientific and technological revolution sparked by the discovery of graphene, due to its layered and two-dimensional structure, researchers have paid great attention to transition metal dichalcogenide (TMDC) materials.

Among these materials, transition metal diselenides have particularly attracted researchers' interest. These materials can exhibit metallic, semiconducting, or insulating behavior and are characterized by unique physical properties, especially in their semiconducting forms. They have been widely used in various scientific fields, including electronics, optics, chemistry, and biomedicine. Furthermore, their properties can be enhanced through various physical and chemical modifications, such as doping with different elements, making them a key focus of modern research.

In this section, we will provide an overview of TMDCs, including their general properties, structure, fabrication methods, and types of doping. Additionally, we will highlight their diverse and widespread applications.

I-2- Structure ofTransition Metal Dichalcogenide (TMDCs):

Transition metals dichalcogenides are layered compoundssimilar in structure to graphite, with the general formula MX_2 where, M is a transition metal of group IV_B, V_B or VI_B,and X is a chalcogen (S,Se,Te)[1].

Figure I.1 shows a presentation of the transition metal dichalcogenides in the periodic table, while **Figure I.2** presents their lamellar structure.

For bonding to occur between metal atoms and the chalcogen atoms, the metal donates four electrons to fill the bonding states, resulting in +4 charge, while the chalcogen carries a -2charge[2].

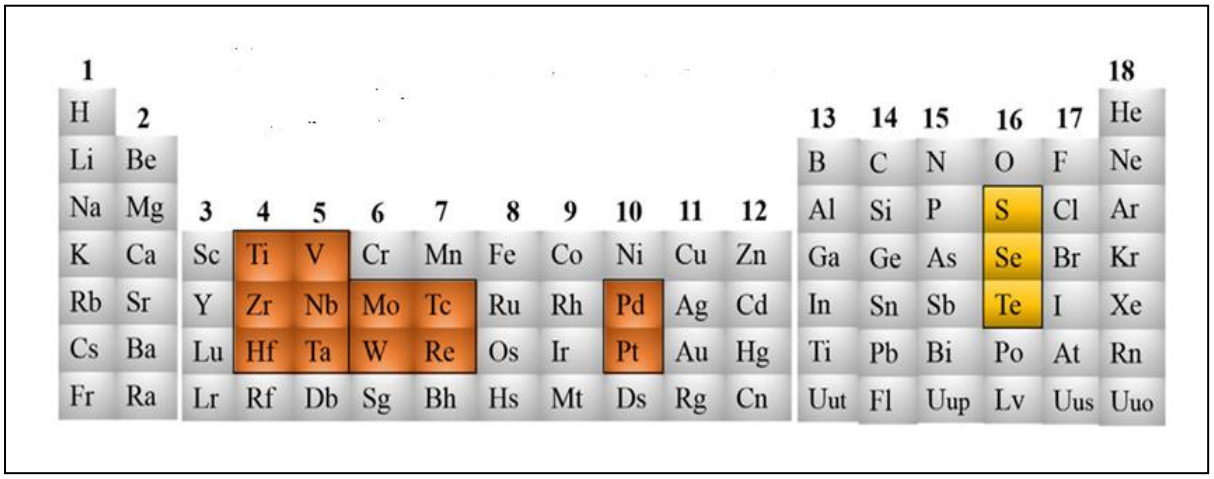


Figure I.1: Representation of TMDCs in periodic table, where the orange and yellow elements represent the metals and chalcogenes, respectively, that form TMDC materials[3].

The bond between atoms within the same layer is covalent in nature, while the layers are held together by weak Van der Waals (VdW) forces[4].

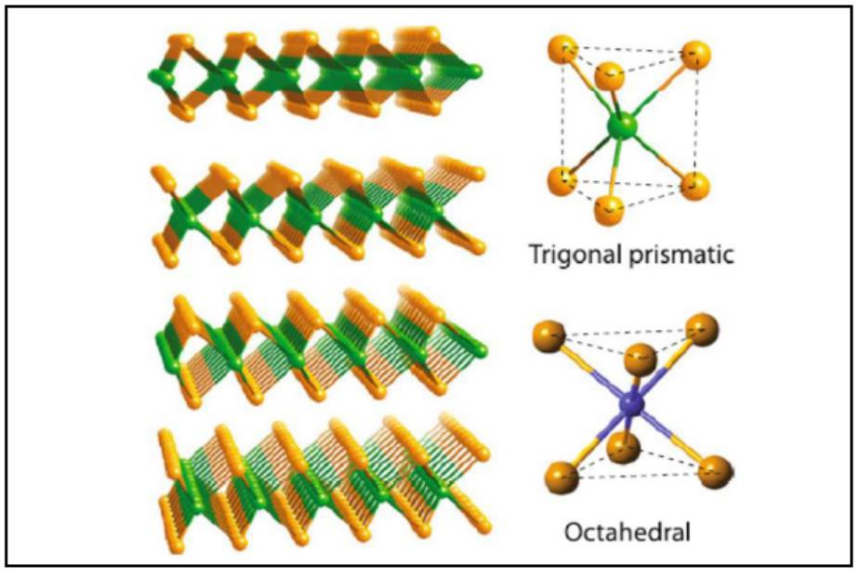


Figure I.2: three-dimensional representation of a typical layered MX_2 structure, where green and purple spheres present M (metal) atoms and orange balls present X (chalcogene) atoms.

TMDCs are classified into three different polytypes, primarlybasedon the number of layers as well as their symmetry (T :trigonal, H:hexagonal, R:rhomboheral), these polytypes are illustrated in **FigureI.3**,and examples for each type can also provided[5] :

- 1T such as $NbSe_2$, $TaSe_2$,…
- 2H such as $MoSe_2$, MoS_2,WSe_2,$MoTe_2$,….

- 3R such as MoS_2,$TaSe_2$,$NbSe_2$,…..

The TMDCs canintrinsecally exhibit a range of electronic properties including [6] :

- SemiconductorlikeMoS$_2$, MoSe$_2$, WS$_2$, WSe$_2$,…
- Metal like TiS$_2$, VSe$_2$,….
- Supraconductor like TaS$_2$, NbS$_2$,…..

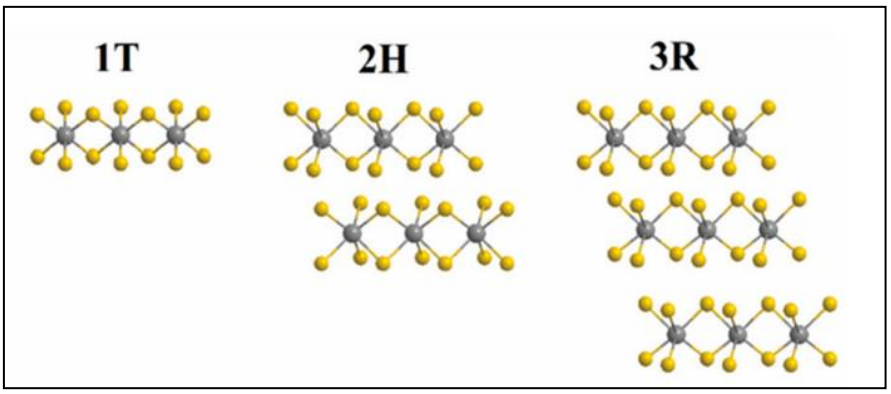


Figure I.3: polytypes of lamellar TMDCs [7].

I-2-1- Transition Metal Dieselenide of the Sixth Column:

These are TMDCs compounds with general formula MSe$_2$, where M is a transition metalfrom group VIBof the periodic table. They can be abbreviated as TMDs.

The elements in this category are: CrSe$_2$, MoSe$_2$, WSe$_2$, these compounds crystallize in the trigonal prismatic phases in their stable state. Additionaly, they are characterized by their semiconducting nature, which made them highly significant in scientific and technological research.

I-3- Fabrication of 2D TMDCs from Bulk Structure:

Experimentally, twomain methods are used to fabricate two-dimensional TMDCs[8, 9], which are:

I-3-1- Top-Down Methods:

This method involves exfoliating structures into low-layred or monolayer structures[10], Several techniques have been highlysuccefulin processing these materials[11], including :

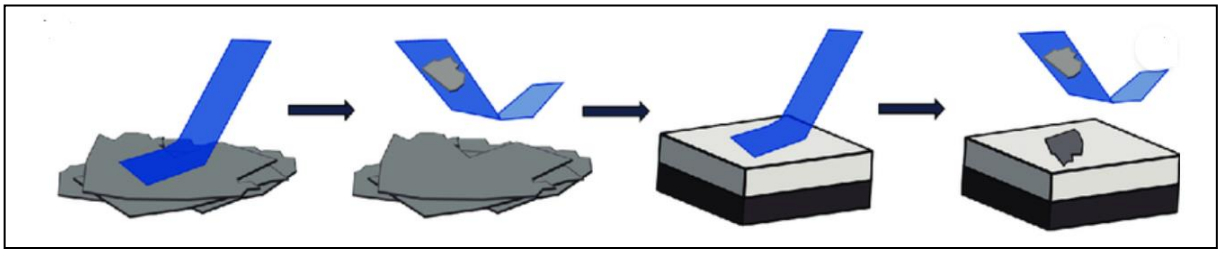
a- Mechanical Exfoliation:

This is the most efficient method for producing clean and highly crystalline nanosheets. In this process, stacked TMDC crystals are exfoliated using adhesive Scotch tape to obtain thin layers Then, the tap is applied to a substrate and rubbed to further split the layers[12].

Afterward, the tape is removed, leaving mono-layer and multi-layer TMDC nanosheets on the substrate.

However, this technique has a major drawback: it produces flakes with random thickness, size, and limited dimensions, making it ineffective for large-scale technological applications[13].

The stages of this technique are illustrated in**Figure I.4**.



FigureI.4: Schematic of mechanical exfoliation process for 2D materials using Scotch tape technique[14].

b- LiquidPhase Exfoliation :

This technique has been successfully used to separate graphene layers and later applied to TMDC materials[15].

It is a simple method that contributes to the relatively inexpensive production of vast quantities of 2D nanosheets, but it introduces defects and lowers the crystalline quality. The basic mechanisms of this method are illustrated in **Figure I.5** and can be described as follows:

- **Ion Intercalation (FigureI.5, a):**

In this method, the layers of the material are separated by first weakening the interlayer bonds through the insertion of ions, which expand the structure.

Then, ultrasonic or thermal agitation is applied to achieve complete layer separation. This process occurs in a liquid environment, such as water.

- **Ion Exchange (FigureI.5, b):**

This technique is used for compounds that contain interlayer ions, which help balance the surface charge of the layers. In this process, these ions are replaced by larger ions in a liquid environment.

Through agitation, the layers are separated, resulting in an exfoliated dispersion[15].

- **Liquid Exfoliation by Direct Ultrasonication (Figure I.5, c):**

In this technique, bulk layered materials are subjected to ultrasonication in a suitable solvent that is dispersive, polar, and has a well-defined surface energy.

To prevent reaggregation, the exfoliated nanosheets must be stabilized either by the solvent itself or through steric or electrostatic repulsion.

This technique has been instrumental in obtaining thin films, only a few nanometers thick, of graphene as well as WS_2 and MoS_2[16].

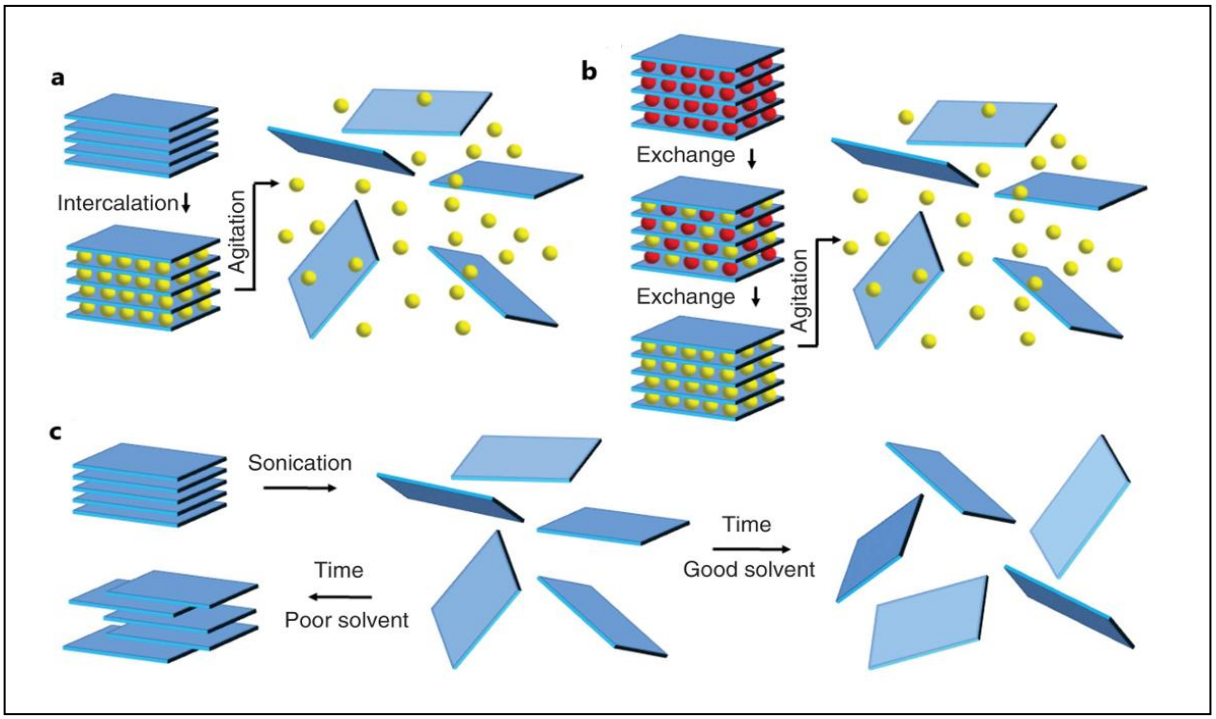


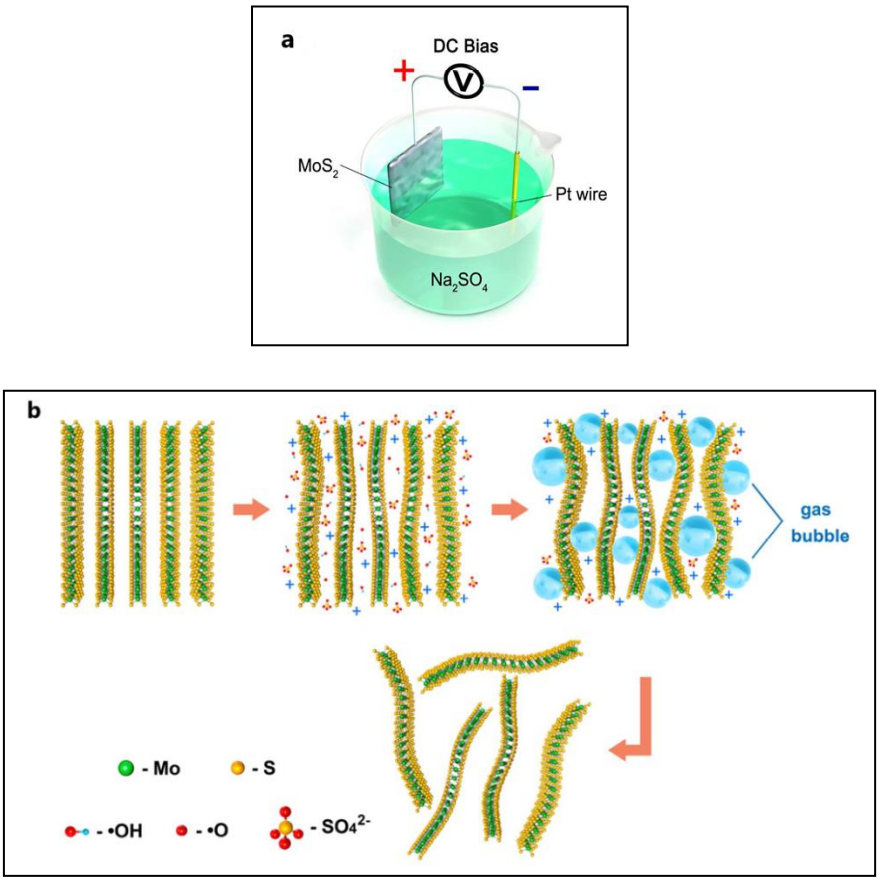
Figure I.5 : Schematic representation of the main liquid exfoliation mechanisms, where (a), (b), and (c) correspond to ion intercalation, ion exchange, and ultrasonication exfoliation, respectively[17].

c- Electrochemical Exfoliation :

This mechanism involves applying a positive current to an electrode made of bulk TMDC material targeted for exfoliation. During the process, water oxidation occurs, generating OH^- and O^-ions, along with other negatively charged ions present in the solution, such as SO_4^{2-}.

Theseanionsaccumulate at the electrode surface and intercalate between the layers of the TMDC material, weakening thevan der Waals forcesthat hold them together.

Subsequently, these anions undergo oxidation between the layers, producing O_2 and SO_2gases, which further separate the layers, leading to their dispersion in the solution[10].**Figure I.6** illustrates this mechanism for bulk MoS_2.



FigureI.6: (a) Experimental setup for electrochemical exfoliation of bulk MoS_2 crystal, (b) Schematic presentationof the electrochemical exfoliation of bulk MoS_2[10].

I-3-2- Bottom-Up Techniques:

This method is highly successful in producing nanosheets of TMDC materials, as it enables control over the number of layers obtained, unlike top-down techniques. Additionally, it yields large-area sheets suitable for technological applications[18].

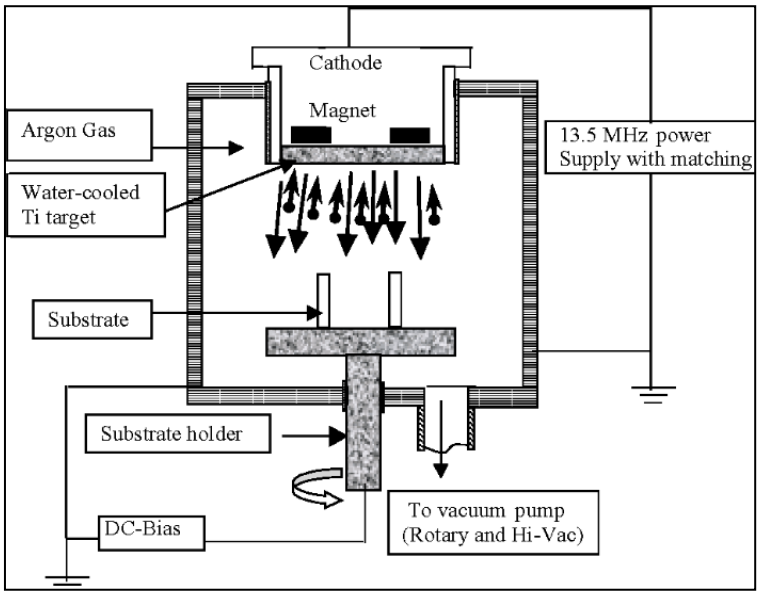
However, one of the challenges this method faces is the difficulty in controlling the reaction kinetics and energy.

Generally, a reaction occurs between the chalcogen and metal-containing precursors, and these reactions can take place in various physical states of matter[19]. This method includes several techniques, such as:

a- For Gas-Phase Synthesis :

It is the most commonly used method due to its relatively easy synthesis of TMDC nanomaterials. This approach simplifies the isolation of the resulting nanosheets from the reaction medium and helps prevent their reaggregation. It isprimarilydividedintotwo main techniques :

- **Physical Vapor Deposition (PVD) :** This technique relies on the deposition of material vapors onto a substrate[19, 20], as illustrated in **Figure I.7.**
- **Chemical Vapor Deposition (CVD)** : Various stages of this process[18], can be illustrated in **FigureI.8.**



FigureI.7: Schematic illustration of the synthesis of TMDC monolayers via PVD method.

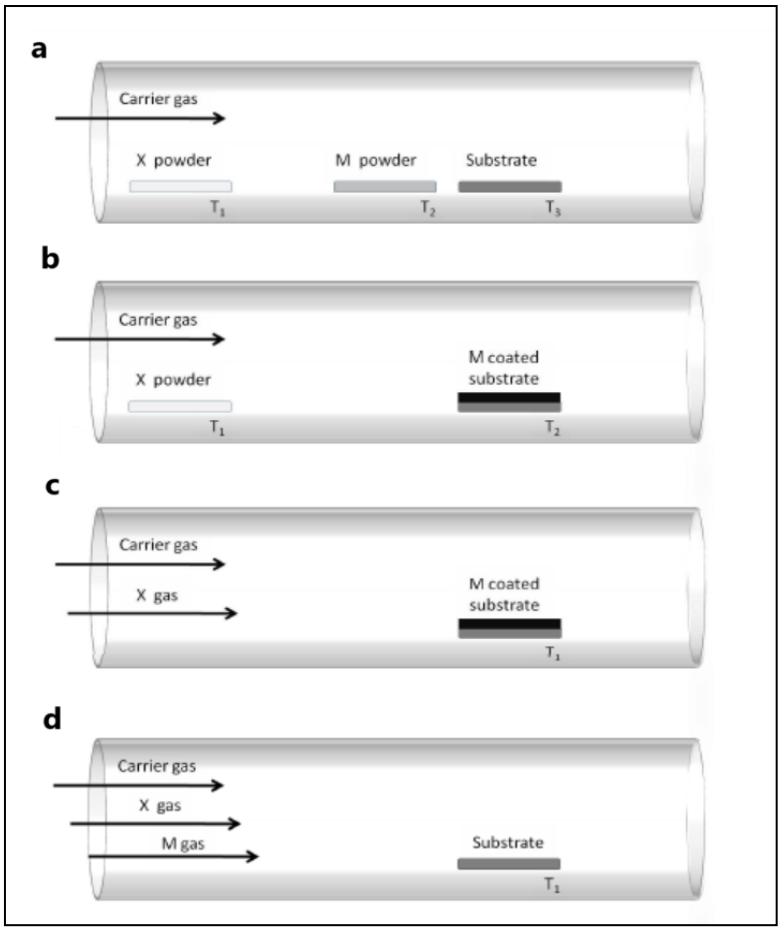


Figure I.8: Schematics of various methods used in TMD technology based on the CVD method in the gas phase,

where: (a)Both metal and the chacogen are in powder form, (b) The chalcogen is in powder form, while the metal or metal oxides deposited on the substrate, (c) the chalcogen is a gaseous precursors, while the metal or metal oxides are deposited on the substrate, (d) both the and chalcogen compounds exist as gaseous precursors[21].

b- For Liquid-Phase Syntheses :

This process is generally carried out throught in-solution thermal decomposition or by injecting a mixture of precursors into a hot solution, followed by isolating the nanosheets suspended in low-boiling solvents as emulsions[19].

Most studies have focused on the group lV and V sulfides or selenides, which are produced by sulfidation reactions with the metal chloride (MClx) in oleylamine[22].

As for group VI sulfides, this method is effective, as studied have yielded nanomaterials with a relatively small thickness (less than 15 nm)[23].

The limitation of this technique is the preparation of TMDC nanosheets with a significant thickness more than 10 nm or the formation of multilayer TMDCsheets[24, 25].

c- For Solid-Phase :

In these reactions, single-source precursor deposited onto a specific substrate and then slowly heated to melt the precursors, thus forming a TMDC nanomaterials within the molten mixture[19].

I-4- The Band Gap (Eg):

The quantum model of solid-state physics, specifically the molecular orbital theory, allows us to determine the possible energy values an electron can take, which are divided into two categories:

- The first category has lower energy, is occupied by electrons in fundamental state, and is called valence band.
- The second category has a higher energy, is vacant in fundamental state, and is called conduction band.

These two bands are separated by a forbidden energy band that an electron cannot occupy[26].

This gap is called the energy bandgap(Eg), and it is one of the most important quantities that determines the electronic properties of the material.

The energy gap dependes on the material:

- Absent in metals due to the overlap of the valence and conduction bands, allowing electrons to move freely between them.
- Very large in insulators, making the transition of electrons from the valence band to the conduction band nearly impossible.
- Small in semiconductors, allowing electrons to transit from the valence band to the conduction band when sufficie excitation is provided, enabling electrical conductivity[27].

I-4-1- Direct and Indirect Band Gap in Semiconductor:

From the energy dispersion graph $E=f(k)$(band structure), we can determine the extreme points of the conduction and valence bands.

The difference between the absolute minimum of the conduction band and the absolute maximum of the valence band represents the gap. Based on this, semiconductors can can be classified into two main types:

- **Direct gap:** Where the conduction band minimum and valence band maximum lie at the same point in k-space.
- **Indirect gap :** Where the conduction band minimum and valence band maximum lie at different points in k-space[28].

We can further illustrate the difference between these two gaps through the two structures shown in **Figure I.9.**

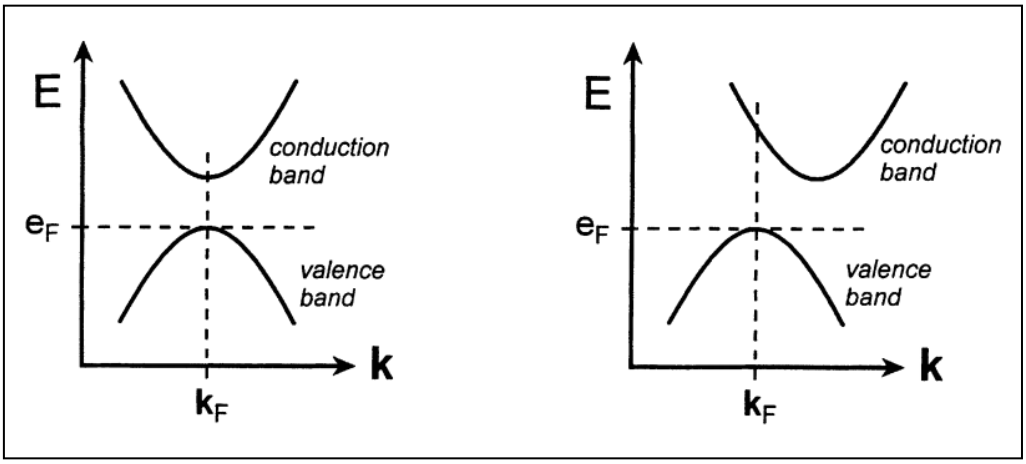


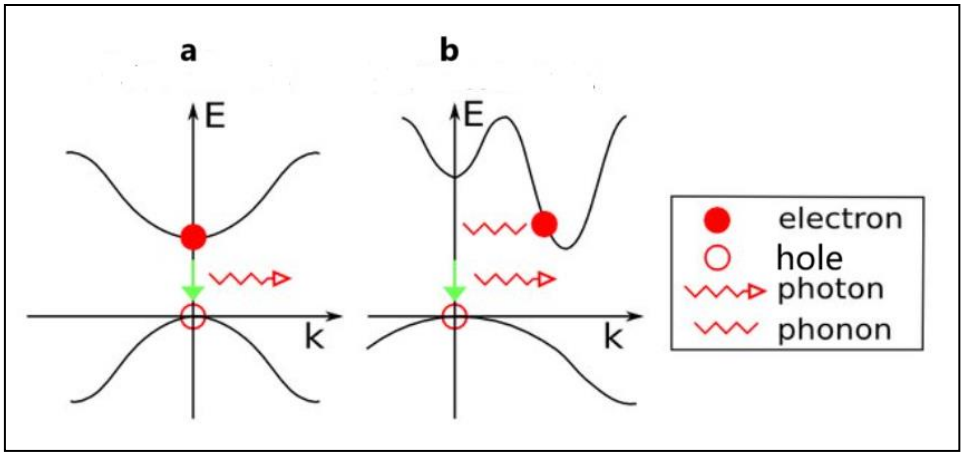
Figure I.9: Direct Band-Gap Semiconductor and indirect Band-Gap Semiconductor[29].

I-4-2-Direct and Indirect Transitions:

Transitions across the forbidden band are very important in the study of the optical properties of materials, as these transitions involve the recombination of electrons and holes[30], There are two cases for transitioning from the conduction band to the valence band :

- **Direct Transition :** This transition of an electron from the conduction band to the valence band is highly probable, as the recombination process involves only one photon, this is because the valence band maximum is at the same wave vector as the conduction band minimum[30], as shown in**Figure I.10,a.**
- **Indirect Transition:**This transition has a low probability, as two simultaneous quantas must be available for it to occur. These are(1) the emitted photon must have energy greater then E_g and a negligible wave vector, and(2) the emission or absorption of a phonon, as shown in **FigureI.10, b.**

A phonon represents a quantized vibration of the crystal lattice,resulting from the exchange of energy absorbed during the generation of electron-hole pair, or dissipated during recombination. It is characterized by a small energy change and a large wave vector[30, 26].



FigureI.10: Schematic showing (a) direct gap transition and (b) indirect gap transition[31].

I-5- Point Defects:

A real crystal is not free from defects, wich can include various types such as point defects, dislocations and grain boundaries[32].

However, point defects remain the most widespread in TMDC monolayer materials, especially in semiconductors, as they create new energy states within the band gap, affecting the physical properties of studied material[33].

Point defects arise during the growth process, the transfer of monolayers, or under the influence of high-energy electron radiation[34].

The percentage of these defects in the material also affects its physical properties[35]There are four types of point defects as shown in the **Figure I.11**, which are:

1-5-1-Vacancies :

This type of point defect occurs when a normally occupied lattice site remains vacant in otherwise an ideal crystal structure. Vacancies play a crucial role in thermal treatment of materials,facilitating atomic diffusion in the solid state by enabling the long-range movement of atoms.

1-5-2-Interstitials:

This defect occurs when an atom occupies a position within the crystal lattice that is normally unoccupied in an ideal crystal.

If the atom is the same type as those in the lattice, it is referred to as an intrinsic interstitial. This type of defect significant role in the formation of alloys.

1-5-3- AntisiteDefects:

This defect occurs when adjacent atoms of different types exchange positions within a crystal lattice.

Antisite defects are commonly observed in alloys and compounds with well ordred structures particularly when the constituent atoms have similar electronegativity.

I-5-4- Substitute Atoms:

This type of defect occurs when an atom outside the crystal system occupies a lattice site such defects play a crucial role in the doping of materials.

significantly altering their electrical and optical properties.

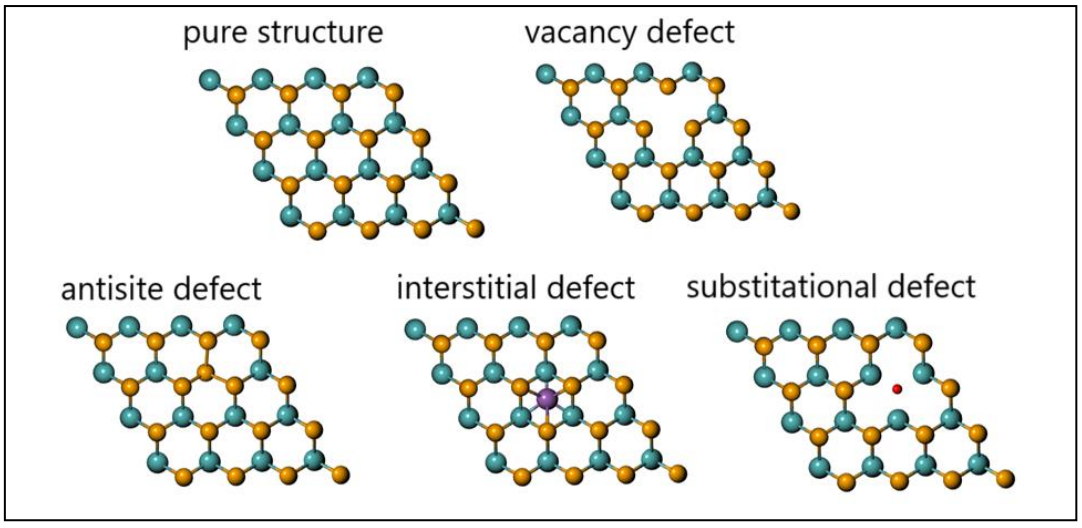


Figure I.11: Types of point defects in crystals.

I-6- Semiconductor Doping :

This process aims to modify the carrier concentration in semiconductor materials, thereby changing their electrical conductivity and overall electronic properties.

This is achieved through doping with carefully selected impurity atoms[36]. The doping method also influences the variation inphysical properties.

There are two primary types of doping, which are n-type and p-type[37].

I-6-1- n-Type Doping:

In this type of doping, the introduced atom acts as a donor, meaning it has more valence electrons than the host atoms, thereby increasing the material's conductivity.

In this case, an extra electron remains free and can transition to the conduction band with relatively low energy.

The energy gap is small because the donor level is positioned close to the edge of the conduction band, as illustrated in **Figure I.12,a**.

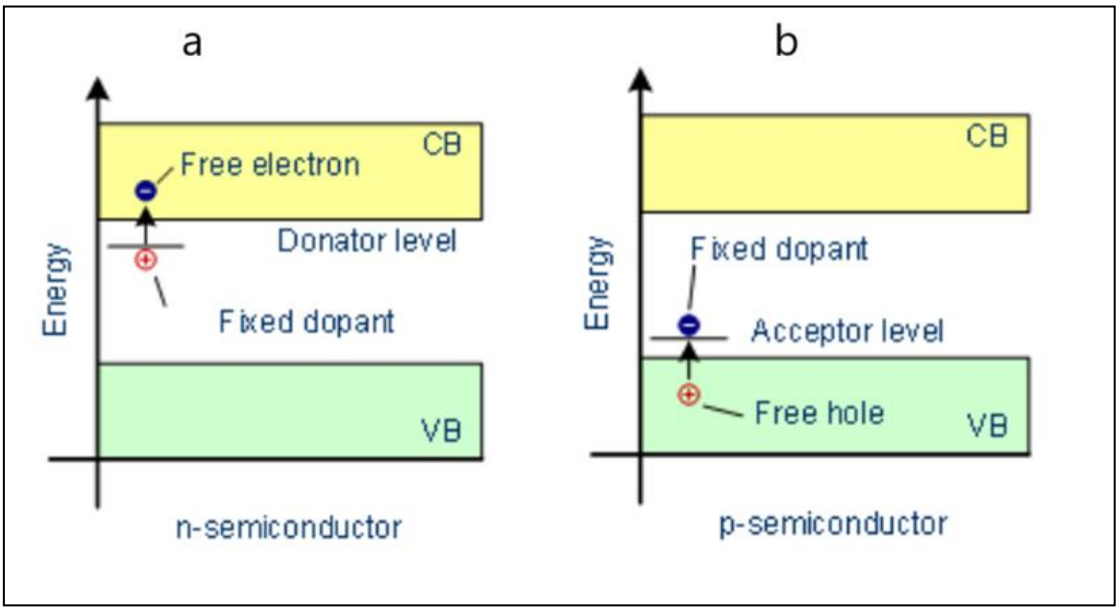
I-6-2- p-Type Doping:

This process is achieved by introducing atoms with fewer valence electrons than those of the host material, thereby creating holes in the semiconductor.

A hole can be filled by a lowenergy electron from the valence band, facilitating charge carrier movement.

In this case, the acceptor energy level is positioned close to the valence band.

FigureI.12,b illustrates the schematic band structure for this scenario.



FigureI.12: Band structure for (a) n-type doping and (b) p-type doping[38].

1-7- Doping in 2D TMDC Monolayer Materials:

The fundamental principles of doping discussed earlier also apply to two-dimensional semiconductors. Researchers have highlighted its significance in enhancing the electrical, optical, and magnetic properties of these materials, depending on the type of foreign atoms introduced.

This modification can be permanent, further increasing the relevance of these materials in modern technological applications.[37].

For example, a monolayer of MoS_2 is naturally an n-type semiconductor. However, when a Mo atom is substituted with an Nb atom, the material transitions to a p-type semiconductor[39].

In this context, there are two fundamental strategies for doping TMDC monolayers:

- Substitutional doping by replacing original atoms in the crystal lattice with foreign atoms.
- Metastable doping which arrises due to external environmental factors like the substrate, metals used as contacts, humidity,etc[40].

The theoretical study based on Density Function Theory (DFT), which will be discussed in the following section, provide a powerful tool for predicting and interpreting experimental results.

However, the study of TMDC monolayer materials presents several challenges, including the following:

- **Controlling Dopant Concentration:** Achieving precise control over dopant concentration remains a challenge, as it is highly dependent on the experimental setup and fabrication.
- **Considering Environmental Effects:** The influence of external factors, such as substrate interactions, temperature variations, and ambient conditions, must be carefully accounted for in theoretical and experimental studies.
- **Inducing Ferromagnetism:**The introduction of ferromagnetic properties through substitutional doping with elements such as Fe, Ni, and Cr at room temperature presents both opportunities and challenges in the design of spintronic devices.

I-8- Application of 2D TMDCs:

The structure of mono and multi-layered of TMDC materials, wich resemble graphene, along with their high surface-to- volume ratio, unique and optimizable properties, have enable their integration into various applications like electrical, optical, chemical, and even biological fields. Some of the most significant applications include the following:

I-8-1- Field-Effect Transistor (FET):

The first use of TMDC materials in transistors was in 2004, where thin layers of single-crystal WSe2were utilized. This implementation demonstrated a notable charge carrier mobility, comparable to that of silicon-based transistors[41].

Then, interest in TMDC-based FETs was revived following the discovery of graphene[42].The FET can used as an amplifier[43,44], an analog switch[45,46], in integrated circuits[43,47], oscillators[48].It is also characterized by its small size and low power consumption compared to the traditional transistor[49].The TMDC-based field-effect transistor (FET) consists of a thin channel of TMDC monolayer material connecting the source and drain region By applying a voltage to modulate the charge carrier concentration, the gate electrode regulates the conductivity of the channel[50], as shown in **Figure I.14,a** and **Figure I.14,b.**TMDC FETs usually behave in two modes: p-channel (p-type), where charge transport is dominated by holes, and n-channel (n-type), where electrons make up the majority of carriers. But some TMDC materials are ambipolar, which means that depending on the gate voltage, they can alternate between n-type and p-type conduction[51].

The choice of TMDCs as a channel materialsis attributed to their appropriate band gap and their thikness, which help mitigate short-channel effects, Additionally, TMDCs exhibit high carrier mobility, enabling fast switching speeds. For instance, MoS_2 has demonstrated a mobility of up to200 $cm^2V^{-1}s^{-1}$[42].

The first $MoSe_2$-base FET was also studied by Larentis et al[52],demonstratingpromising performance and favorable electricalcharacteristics.

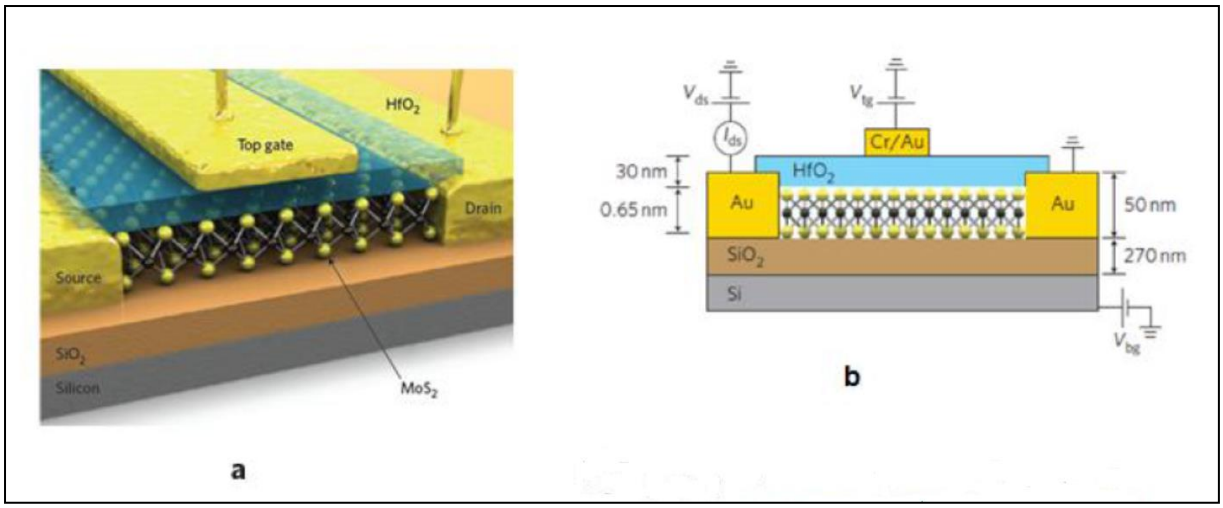


Figure I.14 :(a) MoS2-based FET, (b) Schematic representation of a MoS2 –based FET[53].

I-8-2- Optoelectronic Applications:

The unique properties of monolayer TMDC semiconductors, particularly MS_2 and MSe_2, make them highly promising for optoelectronic applications. These properties include the direct band gap**,** high photoelectron affinity, and the ability to tune the band gapandmodify electrical and optical properties through doping.

Such characteristics enable their use in a wide range of advanced optoelectronic devices, includingphotodetectors, light-emitting devices, and photovoltaic cells.The most notable of these devices are:

a- Phototransistors :

the first fabrication ofmonolayer $MoSe_2$ based phototransistor was reported by Xia et al[54],where the study revealed a relatively low photoresponsivity. Subsequently, a few-layer based phototransistorwas investigated byA. Abderrahmane et al[55], where they found a very high photoresponsitivity compared to all previous studies of 2D materials based potodetectors and estimated in demonstrating a significantly higher photoresponsivity compared to all previously reported 2D material-based photodetectors.

The photoresponsivity was estimated at 97,1 AW^{-1}at zero gate voltage, in addition to a high quantum efficiencyof 22,26%.Vertical heterostructures composed of graphene /MX_2materials /graphene have also demonstrated high quantum efficiency, reaching up to 85%[56].

The use of multilayer MX_2-based photodetectors enables the absorption of light across a wide range of wavelengths from the ultraviolet to the infrared, the **FigureI.15,a**present a schematic of $MoSe_2$-based phototransistor, while, the **FigureI,15,b**illustrates a schematicdiagram of multilayer MoS_2-based photodetector, The same principle is applied in the $MoSe_2$ and other TMDCs semiconductors.

The operating principle of photodetectors is generally based on the generation of bound excitons (electron-hole pairs), when incident photons with energy greater than the band gap of the semiconductor fall on the material.

These excitons are then separated by an electric field, leading to the generation of a photocurrent. This process is fundamental to the functionality of optoelectronic devices**,** enabling applications in imaging, sensing, and optical communication**.**

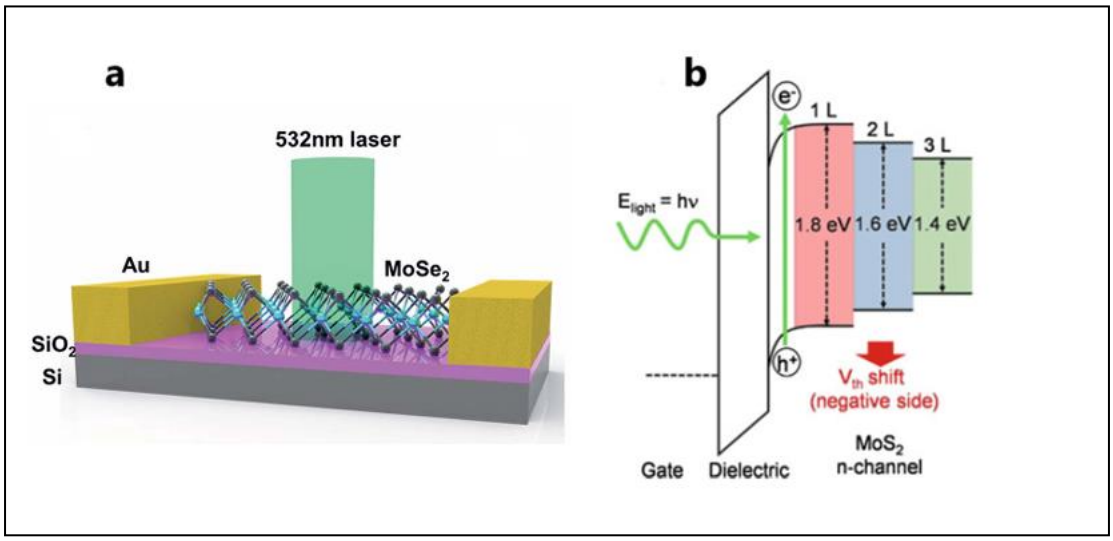


Figure I.15 :(a) Schematic illustrationofa monolayer $MoSe_2$-basedphototransistor exposed to a laser beam [54], (b) Schematic showing of the impact of incident photons on a multilayer MoS_2-based phototransistor (n-channel) [57].

b- Light-EmittingDiods (LEDs) :

The TMDCs semiconductor have been used in the fabrication of LEDs through electrical axcitation, thanks to the direct-gap property of the semiconductor monolayer TMDCs.

Researchers have developed and studied the LEDs based on monolayer TMDCs across a wide range of frequencies showed efficiencies of up 10%. Notabely, a monolayer$MoSe_2$-based light-emitting diode was fabricated byBritton W. H. Baugher et al[58].

c- Solar Cells :

Since their initial development in 1954[59], solar cells have attracted significant research interest, with continuous advancements aimed at enhancing their efficiency and reducing production costs.Solar cells based on TMDCs have sparked a significant revolution due to their exceptional optical properties, which can be further enhanced through doping[60], TMDC semiconductors typically exhibit a direct band gap ranging from 1.5 eV to 2 eV, which corresponds to a high absorption coefficient for visible light. Additionally, their ability to be deposited onto metals makes them promising candidates for use as ohmic back contacts or gate materials in solar cells.

FigureI.16,apresents a schematic representation of a WSe_2-based solar cell.**FigureI.16,b**illustrates the photoluminescence spectrum of the cell for single, bilayer and multilayer configurations, while **Figures I.16, c** and **FigureI.16,d** represent the variations in bias voltage (V) as a function of current (nA) in dark conditionsand under optical illumination, respectively.

The simulation of a $WTe_2/MoSe_2$–based gate yielded apower conversion efficiency(PCE) of 30.7%, surpassing the efficiency of previously studied systems[61].

The synthesis of Fe-doped $MoSe_2$on a SnO_2 substrate, which served as a counter electrode (CE) in dye-sensitized solar cells, demonstrated excellent performance in terms of electrocatalytic activity and reduced overpotential loss[62].

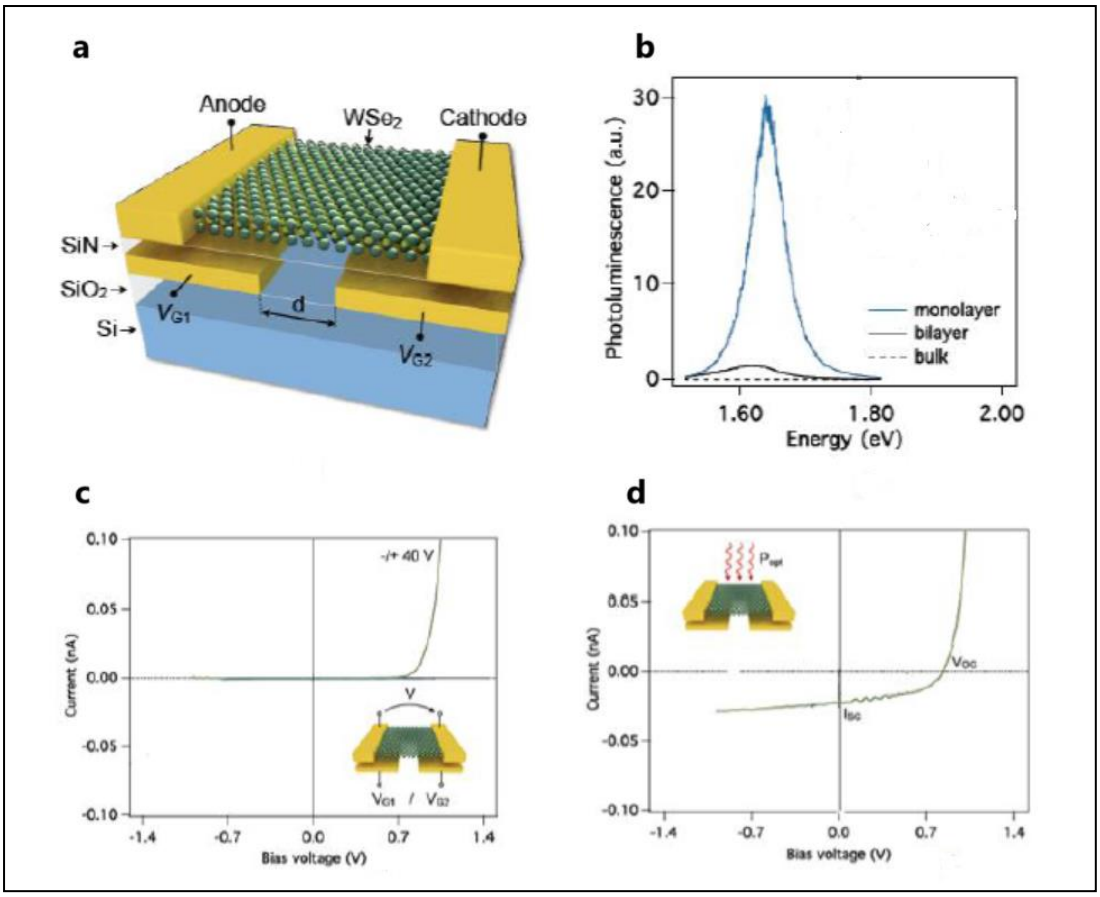


Figure I.16:(a) Schematic of a WSe_2-based solar cell, (b) photoluminescence spectrum of WSe_2-based solar cell, (c)variation of bias voltage (V) as a function of current (nA) in the dark , (d) the variation of bias voltage (V) as a function of current (nA) under optical illumination[63].

I-8-3- Energy Storage:

a- Lithuim-Ion Batteries (LIBs):

Lithium batteries are among the most attractive energy storage devices due to their rechargeability, environmental compatibility, high volumetric energy density, and relatively long service life. These batteries are widely used in various everyday devices, including mobile phones, laptops, drones, and other electronic applications.

The utilization of monolayer and multilayer TMDCs as electrode materials for lithium-ion batteries has garnered significant attention in recent years.However, their application as anodes has encountered several challenges, including low electrical conductivity, electrode fragmentation, and limitations in cycle stability[60].

MoS_2 was the first TMDC material used as an anode in lithium-ion batteries. Subsequently, $MoSe_2$ was introduced, demonstrating superior performance due to its larger

interlayer spacing compared to MoS_2, which facilitates better ion intercalation[64].Dhanasekaran Vikraman et al. successfully synthesized a large quantity of $MoSe_2$ for use as a cathode in lithium-ion batteries. Their study reported a high coulombic efficiency of 99% after 100 cycles and a discharge capacity of843 $mAhg^{-1}$ [65].

The storage mechanism in lithium-ion batteries is based on the intercalation of lithium ions (Li^+) between MX_2 layers[66], This process can be described by the following reaction:

$$MX_2 + 4Li^+ + 4e^- \leftrightarrow M + 4Li_2X \quad \text{(I-1)}$$

b- Sodium-Ion Batteries (SIBs) :

These batteries operate similarly to lithium-ion batteries but offer a more cost-effective alternative due to the abundance and lower cost of their raw materials. Additionally, the use of aluminum foil as an anode material contributes to their lightweight design and further reduces production costs. In this context, TMDC nanomaterials have demonstrated high efficiency in energy storage applications, achieving efficiencies of up to 98%[60].

c- Potassuim Ion Batteries (PIBs) :

Potassium-ion batteries offer several advantages, including lower cost compared to previously mentioned battery technologies and a low redox potential, which has attracted significant research interest.

JunMin Ge et al[67]made an anode on $MoSe_2$/N-C, which demonstrated a high discharge capacity of 258,02 $mAhg^{-1}$ after 300 cycles, along with a coulombic efficiency of one 100%. AdditionallyPIBsexhibit excellent stability under harsh conditions, operating efficiently within a thermal range of -10°C to 50°C[60].

d- Supercapacitor :

They are also called electrochemical capacitors (ECs) and are characterized by a longer cycle life, good performance at high and low temperatures, fast charging, low maintenance costs, and better efficiency than batteries.

However, they have a lower energy density than batteries.

These compounds can be classified into two categories based on their mechanism of action. The first category stores electrostatic charge in the form of a double layer, while the second category stores charge by attracting ions from the electrolyte to the surface of the electrode, where a redox reaction occurs. The latter is known as pseudo capacitors.

Initially, graphite was used as an electrode.To find electrodes with higher density and larger surface area, TMDCs were introduced.

The first study on TMDC-based electrodes was conducted in 2007 by Jia Mei Soon and Kian Ping Loh[68], who investigated the use of multi-layer as an electrode in supercapacitors. Subsequently, numerous studies have explored various TMDC compounds, including $MoSe_2$. In this context, SK Balasingam et al [69]examined the electrochemical performance of $MoSe_2$ nanosheets as an electrolyte material for supercapacitors, reporting high efficiency with a capacity retention of 75% after 10000 cycles.

I-8-4- Catalyst for Hydrogen Evolution Reaction (HER):

Hydrogen energy is among the most significant clean energy sources that have garnered considerable attention from researchers.

However, its widespread adoption faces several challenges, including a slow reaction rate, high production costs, and limited yield relative to demand[60, 70].

Therefore, it is essential to explore efficient hydrogen catalysts capable of addressing these limitations.

Recently, significant attention has been directed toward two-dimensional transition metal dichalcogenides (2D TMDCs) for their potential use as electrocatalysts in the hydrogen evolution reaction (HER). Studies have demonstrated that TMDCs in the 1T phase exhibit high efficiency in accelerating the HER[71, 72].

However, they are not effective in their pristine state; modifications such as introducing vacancies, activating heteroatoms, engineering grain boundaries, and constructing heterostructures are necessary to create active sites[73], facilitate hydrogen bubble pathways, and enhance electron mobility[74].

The mechanism of HER catalysis in both acidic and alkaline media is illustrated in **FigureI.17.**

Several studies have been conducted in this field, where Gholamvand et al[75] have demonstrated that enhanced $MoSe_2$ films are the best electrocatalyst for hydrogen evolution reaction. This is attributed to their ability to serve as a good source of OH- radicals, facilitated by the ease of surface oxidation[72].

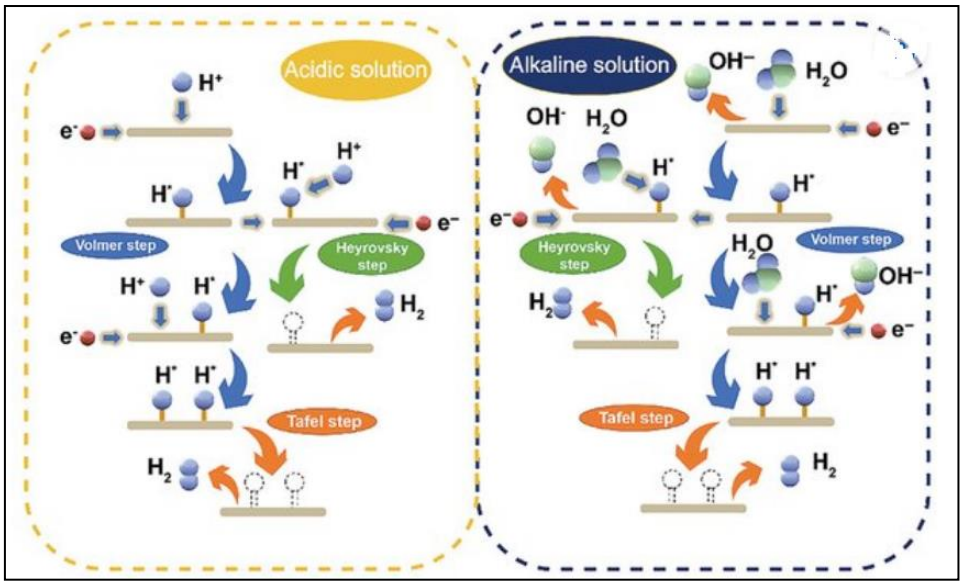


Figure I.17: Schematic representation of HER mechanism in acidic and alkaline solutions[76].

I-8-5- Chemical Gas Sensors:

The development of semiconductor-based toxic gas sensors, which traditionally operate at high temperatures, has advanced significantly following the fabrication of TMDC-based sensors capable of functioning at room temperature[77].

The detection of toxic gases relies on charge transfer between gas molecules and the reactive sites on the surfaces of TMDC materials through oxidation-reduction reactions. [78]

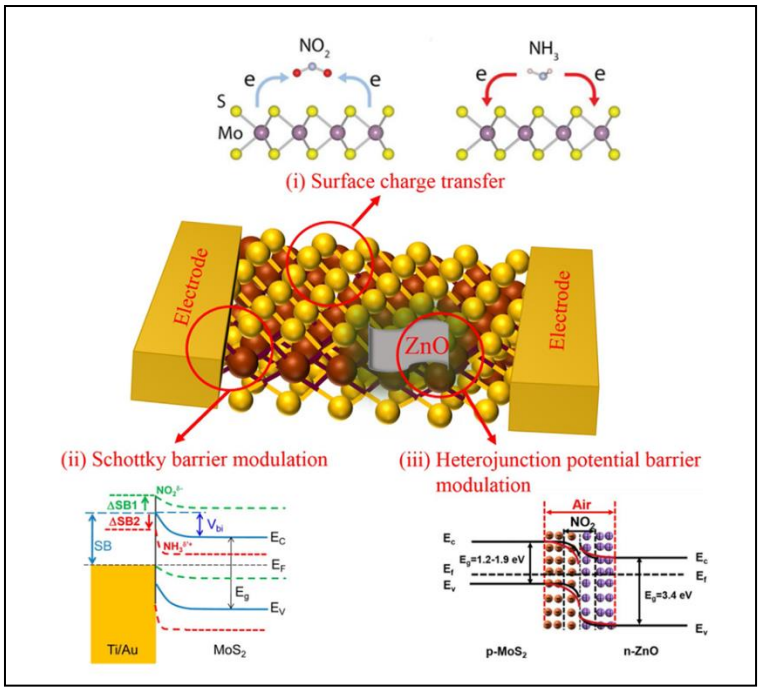
This interaction disturbs the surface charge of the material, thereby altering its conductivity.

For example, the NO_2 molecule acts as an oxidizing agent due to the presence of two unpaired electrons, whereas the NH_3 molecule functions as a reducing agent because of its ability to donate electrons from its lone pair. Meanwhile, the reactive sites on the TMDC surface facilitate electron transfer by either accepting or donating electrons[79].

The Schottky barrier and the potential barrier between the TMDC material and the electrode or metal oxide, respectively, contribute to enhancing sensor performance[3], The gas sensing mechanism is summarized in **Figure I.18.**

Dattatray J. Late and his colleagues utilized monolayer $MoSe_2$ as a gas sensor, demonstrating high performance at room temperature[80].

Similarly, Rahul Kumar et al[3]developed a $MoSe_2$-based epidermal gas sensor for the detection of toxic gases, specifically NO_2 and NH_3.

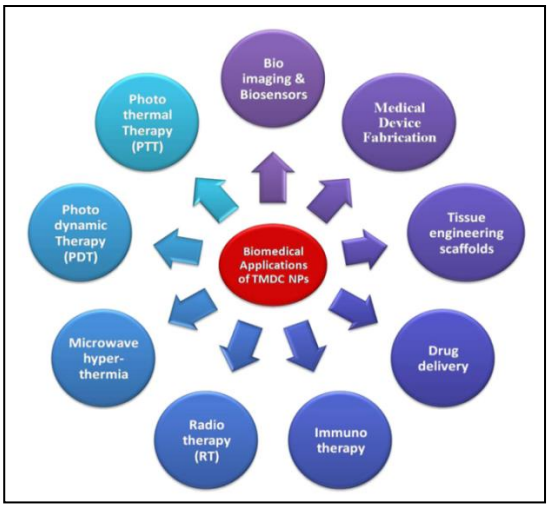


FigureI.18: Schematic represontation of the gas sensing mechanism in a MoS2-based sensor, (i)[81], (ii)[82], (iii)[83]

I-8-6- Biomedical Applications:

Two-dimensional TMDCs have been used as sensors in the biomedical field.Annu Mishra et al[84]employed fluorine-doped.

$MoSe_2$in the form of a nano broom for the detection of *Salmonella* bacteria, Additionally, a $MoSe_2$-based sensor was used by Azadeh Azadbakht et al[85] for the detection of kanamycin in milk, Several TMDC-based biosensors have also been developed for detecting analytes such as DNA, RNA, and dopamine[77], In addition to biosensors, TMDC nanomaterials have been extensively studied for various biomedical applications, which are summarized in **Figure I.19**.



FigureI.19: various biomedical applications of TMDC nanoparticules[77].

I-9- $MoSe_2$ Monolayer and Arsenic Doping: General Overview and Scientific Motivation :

As previously mentioned, two-dimensional (2D) materials have revolutionized the field of condensed matter physics and materials science due to their remarkable physical and chemical properties. Among these, transition metal dichalcogenides (TMDCs) have emerged as a particularly versatile class of layered materials[6].

In particular, transition metal diselenides ($TMdSe_2$) from group VI of the periodic table, such as $MoSe_2$ and WSe_2, have attracted significant interest due to their tunable band structures, layer-dependent electronic properties, and potential applications in nanoelectronics and optoelectronics[7].

Within this family, molybdenum diselenide ($MoSe_2$) stands out for its stable hexagonal crystal structure[5], moderate direct band gap in the monolayer form, and excellent photoresponsivity. These features make it highly suitable for applications in field-effect transistors, photodetectors, and solar energy [61, 62]conversion devices, as well as for more specific functionalities such as catalysis[70] and sensing[80]. Moreover, the electronic and optical properties of $MoSe_2$ are highly sensitive to external modifications, including mechanical strain, defect engineering, and chemical doping[41].

In this work, we investigate both substitutional and interstitial doping of $MoSe_2$ with arsenic atoms. Arsenic is selected due to its covalent radius being comparable to that of selenium and its potential to introduce localized electronic states within the band structure

features that could enhance charge carrier mobility and optical absorption. Furthermore, due to the small size of the arsenic atom compared to molybdenum and selenium, we compare its incorporation with the effect of a vacancy at the Mo site. The primary objective is to tailor the electronic and optoelectronic properties of $MoSe_2$ monolayers for enhanced device performance.

To the best of our knowledge, no previous theoretical or experimental studies have specifically addressed arsenic doping in monolayer $MoSe_2$, either by substitution at the Mo site or via interstitial configurations. Thus, our work fills an important gap by providing a detailed ab initio analysis using density functional theory (DFT). This investigation provides new insights into the structural, electronic, and optical modifications induced by arsenic incorporation.

To accurately predict and analyze these effects, we employ first-principles DFT calculations within the pseudopotential approximation wich is an approach that is well-suited to the simulation of low-dimensional materials. Chapter II presents the theoretical background and computational framework adopted in this study, including the foundational concepts of DFT, the treatment of exchange–correlation effects, the role of pseudopotentials in modeling electron–ion interactions and the computational package used to perform the simulations.

References:

[1] G. Kresse and J. Hafner, "Ab initio molecular dynamics for liquid metals," *Phys. Rev. B*, vol. 47, no. 1, pp. 558–561, Jan. 1993, doi: 10.1103/PhysRevB.47.558.

[2] M. Chhowalla, H. S. Shin, G. Eda, L.-J. Li, K. P. Loh, and H. Zhang, "The chemistry of two-dimensional layered transition metal dichalcogenide nanosheets," *Nat. Chem.*, vol. 5, no. 4, pp. 263–275, Apr. 2013, doi: 10.1038/nchem.1589.

[3] R. Kumar, N. Goel, M. Hojamberdiev, and M. Kumar, "Transition metal dichalcogenides-based flexible gas sensors," *Sensors Actuators, A Phys.*, vol. 303, p. 111875, 2020, doi: 10.1016/j.sna.2020.111875.

[4] J. A. Wilson and A. D. Yoffe, "The transition metal dichalcogenides discussion and interpretation of the observed optical, electrical and structural properties," *Adv. Phys.*, vol. 18, no. 73, pp. 193–335, May 1969, doi: 10.1080/00018736900101307.

[5] M. Yamamoto *et al.*, "Strong Enhancement of Raman Scattering from a Bulk-Inactive Vibrational Mode in Few-Layer MoTe 2," *ACS Nano*, vol. 8, no. 4, pp. 3895–3903, Apr. 2014, doi: 10.1021/nn5007607.

[6] R. R. Nair *et al.*, "Fine Structure Constant Defines Visual Transparency of Graphene," *Science (80-.).*, vol. 320, no. 5881, pp. 1308–1308, Jun. 2008, doi: 10.1126/science.1156965.

[7] Y. K. Gun, "Materials Advances and their applications," pp. 146–164, 2021, doi: 10.1039/d0ma00697a.

[8] H. Nam *et al.*, "MoS 2 Transistors Fabricated via Plasma-Assisted Nanoprinting of Few-Layer MoS 2 Flakes into Large-Area Arrays," *ACS Nano*, vol. 7, no. 7, pp. 5870–5881, Jul. 2013, doi: 10.1021/nn401093u.

[9] E. Varrla *et al.*, "Large-Scale Production of Size-Controlled MoS 2 Nanosheets by Shear Exfoliation," *Chem. Mater.*, vol. 27, no. 3, pp. 1129–1139, Feb. 2015, doi: 10.1021/cm5044864.

[10] N. Liu, P. Kim, J. H. Kim, J. H. Ye, S. Kim, and C. J. Lee, "Large-Area Atomically Thin MoS 2 Nanosheets Prepared Using Electrochemical Exfoliation," *ACS Nano*, vol. 8, no. 7, pp. 6902–6910, Jul. 2014, doi: 10.1021/nn5016242.

[11] X. Li *et al.*, "Large-Area Synthesis of High-Quality and Uniform Graphene Films on Copper Foils," *Science (80-.).*, vol. 324, no. 5932, pp. 1312–1314, Jun. 2009, doi: 10.1126/science.1171245.

[12] A. A. Pirzado *et al.*, "Few-layer graphene from mechanical exfoliation of graphite-

based materials: Structure-dependent characteristics," *ChemEngineering*, vol. 3, no. 2, pp. 1–10, 2019, doi: 10.3390/chemengineering3020037.

[13] K. S. Novoselov, "Nobel Lecture: Graphene: Materials in the Flatland," *Rev. Mod. Phys.*, vol. 83, no. 3, pp. 837–849, Aug. 2011, doi: 10.1103/RevModPhys.83.837.

[14] M. Yang, Z. Ye, M. A. Iqbal, H. Liang, and Y. J. Zeng, "Progress on two-dimensional binary oxide materials," *Nanoscale*, vol. 14, no. 27, pp. 9576–9608, 2022, doi: 10.1039/d2nr01076c.

[15] V. Nicolosi, M. Chhowalla, M. G. Kanatzidis, M. S. Strano, and J. N. Coleman, "Liquid Exfoliation of Layered Materials," *Science (80-.).*, vol. 340, no. 6139, Jun. 2013, doi: 10.1126/science.1226419.

[16] J. N. Coleman *et al.*, "Two-Dimensional Nanosheets Produced by Liquid Exfoliation of Layered Materials," *Science (80-.).*, vol. 331, no. 6017, pp. 568–571, Feb. 2011, doi: 10.1126/science.1194975.

[17] J. N. Coleman *et al.*, "023 Coleman2011.Pdf," *Science (80-.).*, vol. 331, no. February, pp. 568–571, 2011, [Online]. Available: http://science.sciencemag.org/

[18] M. Bosi, "Growth and synthesis of mono and few-layers transition metal dichalcogenides by vapour techniques: A review," *RSC Adv.*, vol. 5, no. 92, pp. 75500–75518, 2015, doi: 10.1039/c5ra09356b.

[19] J. R. Brent, N. Savjani, and P. O'Brien, "Synthetic approaches to two-dimensional transition metal dichalcogenide nanosheets," *Prog. Mater. Sci.*, vol. 89, pp. 411–478, 2017, doi: 10.1016/j.pmatsci.2017.06.002.

[20] A. Oasmaa, I. Fonts, M. R. Pelaez-Samaniego, M. E. Garcia-Perez, and M. Garcia-Perez, "Pyrolysis Oil Multiphase Behavior and Phase Stability: A Review," *Energy & Fuels*, vol. 30, no. 8, pp. 6179–6200, Aug. 2016, doi: 10.1021/acs.energyfuels.6b01287.

[21] M. Bosi, "Growth and synthesis of mono and few-layers transition metal dichalcogenides by vapour techniques: a review," *RSC Adv.*, vol. 5, no. 92, pp. 75500–75518, 2015, doi: 10.1039/C5RA09356B.

[22] C. D. Layered, "Well-De fi ned Colloidal 2 - D Layered Transition-Metal Chalcogenide Nanocrystals via Generalized Synthetic Protocols - 2012 - Layered.p.pdf," pp. 1–4, 2012.

[23] L. Cheng, W. Huang, Q. Gong, C. Liu, Z. Liu, and Y. Li, "Ultrathin WS 2 Nanoflakes as a High-Performance Electrocatalyst for the Hydrogen Evolution Reaction**," pp. 1–5, 2014, doi: 10.1002/anie.201402315.

[24] P. Sekar, E. C. Greyson, J. E. Barton, and T. W. Odom, "Synthesis of Nanoscale NbSe 2 Materials from Molecular Precursors," *J. Am. Chem. Soc.*, vol. 127, no. 7, pp. 2054–2055, Feb. 2005, doi: 10.1021/ja0428006.

[25] C. Altavilla, M. Sarno, and P. Ciambelli, "A Novel Wet Chemistry Approach for the Synthesis of Hybrid 2D Free-Floating Single or Multilayer Nanosheets of MS 2 @oleylamine (M═Mo, W)," *Chem. Mater.*, vol. 23, no. 17, pp. 3879–3885, Sep. 2011, doi: 10.1021/cm200837g.

[26] H. N. Christian Ngô, *Physique des semi-conducteurs*, 4th ed. Dunod, 2012.

[27] C. Kittel, *Physique de l'état solide*, Ed. Dunod. 1983.

[28] H. Mathieu, *Physique des Semiconducteurs et des Composants électronique*, 4eme ed. masson, 1998.

[29] D. Seo and R. Ho, "Indirect Band Gap," *Encycl. Inorg. Bioinorg. Chem.*, pp. 23–32, 2005, doi: 10.1002/9781119951438.eibd0414.

[30] J. S. J.Boucher, *Principes et fonctions de l'électronique intégrée*. Capadues, 1977.

[31] M. Jean-françois, "Conception d ' un circuit int ′ egr ′ e en SiC appliqu ′ e aux convertisseur de moyenne puissance Thèse Jean-François MOGNIOTTE," 2014.

[32] G. Aka, "partie B : Défauts ponctuels dans les solides: Modèle du cristal réel.," in *Chimie du solide*, école national supérieure de chimie de paris, Ed. paris, 2013.

[33] P. E. Batson, "Atomic and Electronic Structure of a Dissociated 60° Misfit Dislocation in Ge_X," *Phys. Rev. Lett.*, vol. 83, no. 21, pp. 4409–4412, Nov. 1999, doi: 10.1103/PhysRevLett.83.4409.

[34] W. Zhou *et al.*, "Intrinsic Structural Defects in Monolayer Molybdenum Disulfide," *Nano Lett.*, vol. 13, no. 6, pp. 2615–2622, Jun. 2013, doi: 10.1021/nl4007479.

[35] Y. C. Lin *et al.*, "Properties of individual dopant atoms in single-layer MoS2: Atomic structure, migration, and enhanced reactivity," *Adv. Mater.*, vol. 26, no. 18, pp. 2857–2861, 2014, doi: 10.1002/adma.201304985.

[36] E. Mooser, *Introduction à la Physique du solide*. Presses polytechniques et universitaires romandes, 1993.

[37] W. S. Kenneth A. Jackson, *Handbook of semiconductor technology*. Wiley-VCH, 2000.

[38] D. P. Bhandarkar and J. E. Juliussen, "Semiconductor technology," *ACM SIGARCH Comput. Archit. News*, vol. 7, no. 1, pp. 4–14, 1978, doi: 10.1145/859418.859419.

[39] J. Suh *et al.*, "Reconfiguring crystal and electronic structures of MoS2 by substitutional doping," *Nat. Commun.*, vol. 9, no. 1, pp. 1–7, 2018, doi: 10.1038/s41467-017-02631-9.

[40] K. Zhang and J. Robinson, "Doping of Two-Dimensional Semiconductors: A Rapid Review and Outlook," *MRS Adv.*, vol. 4, no. 51–52, pp. 2743–2757, Oct. 2019, doi: 10.1557/adv.2019.391.

[41] N. Izyumskaya, D. O. Demchenko, V. Avrutin, Ü. Özgür, and H. Morkoç, "Two-dimensional MoS2 as a new material for electronic devices," *Turkish J. Phys.*, vol. 38, no. 3, pp. 478–496, 2014, doi: 10.3906/fiz-1407-16.

[42] F. Schwierz, "Nanoelectronics: Flat transistors get off the ground," *Nat. Nanotechnol.*, vol. 6, no. 3, pp. 135–136, 2011, doi: 10.1038/nnano.2011.26.

[43] B. Radisavljevic, M. B. Whitwick, and A. Kis, "Integrated Circuits and Logic Operations Based on Single-Layer MoS 2," *ACS Nano*, vol. 5, no. 12, pp. 9934–9938, Dec. 2011, doi: 10.1021/nn203715c.

[44] B. Radisavljevic, M. B. Whitwick, and A. Kis, "Small-signal amplifier based on single-layer MoS 2," *Appl. Phys. Lett.*, vol. 101, no. 4, p. 043103, Jul. 2012, doi: 10.1063/1.4738986.

[45] M. Bucher, C. Lallement, F. Krummenacher, and C. Enz, "A MOS Transistor Model for Mixed Analog-digital Circuit Design and Simulation," *Des. Syst. a Chip*, pp. 49–95, 2006, doi: 10.1007/1-4020-7929-x_3.

[46] A. Horri, "Design of Flash analog-to-digital converter based on MoS2 FET," *Integration*, vol. 101, p. 102308, Mar. 2025, doi: 10.1016/j.vlsi.2024.102308.

[47] H. Wang *et al.*, "Integrated Circuits Based on Bilayer MoS 2 Transistors," *Nano Lett.*, vol. 12, no. 9, pp. 4674–4680, Sep. 2012, doi: 10.1021/nl302015v.

[48] S. Two-dimensional, D. Jariwala, V. K. Sangwan, L. J. Lauhon, T. J. Marks, and M. C. Hersam, "Emerging Device Applications for semiconducting 2D TMDCs," *ACS Nano*, vol. 8, no. 2, pp. 1102–1120, 2014, [Online]. Available: http://www.ncbi.nlm.nih.gov/pubmed/24476095

[49] C. Wang, Y. Song, and H. Huang, "Evolution Application of Two-Dimensional MoS2-Based Field-Effect Transistors," *Nanomaterials*, vol. 12, no. 18, 2022, doi: 10.3390/nano12183233.

[50] V. Podzorov, M. E. Gershenson, C. Kloc, R. Zeis, and E. Bucher, "High-mobility field-effect transistors based on transition metal dichalcogenides," *Appl. Phys. Lett.*, vol. 84, no. 17, pp. 3301–3303, 2004, doi: 10.1063/1.1723695.

[51] W. Shi *et al.*, "Superconductivity Series in Transition Metal Dichalcogenides by Ionic Gating," *Sci. Rep.*, vol. 5, pp. 1–10, 2015, doi: 10.1038/srep12534.

[52] S. Larentis, B. Fallahazad, E. Tutuc, S. Larentis, B. Fallahazad, and E. Tutuc, "Field-

effect transistors and intrinsic mobility in ultra-thin MoSe2 layers Field-effect transistors and intrinsic mobility in ultra-thin MoSe 2 layers," *Appl. Phys. Lett.*, vol. 223104, no. 2012, pp. 1–4, 2015, [Online]. Available: https://doi.org/10.1063/1.4768218%0Ahttp://aip.scitation.org/toc/apl/101/22

[53] B. Radisavljevic, A. Radenovic, J. Brivio, V. Giacometti, and A. Kis, "Single-layer MoS2 transistors," *Nat. Nanotechnol.*, vol. 6, no. 3, pp. 147–150, 2011, doi: 10.1038/nnano.2010.279.

[54] J. Xia *et al.*, "CVD synthesis of large-area, highly crystalline MoSe2 atomic layers on diverse substrates and application to photodetectors," *Nanoscale*, vol. 6, no. 15, pp. 8949–8955, 2014, doi: 10.1039/c4nr02311k.

[55] A. Abderrahmane, P. J. Ko, T. V. Thu, S. Ishizawa, T. Takamura, and A. Sandhu, "High photosensitivity few-layered MoSe2 back-gated field-effect phototransistors," *Nanotechnology*, vol. 25, no. 36, pp. 0–4, 2014, doi: 10.1088/0957-4484/25/36/365202.

[56] W. J. Yu *et al.*, "Highly efficient gate-tunable photocurrent generation in vertical heterostructures of layered materials," *Nat. Nanotechnol.*, vol. 8, no. 12, pp. 952–958, Dec. 2013, doi: 10.1038/nnano.2013.219.

[57] H. S. Lee *et al.*, "MoS 2 nanosheet phototransistors with thickness-modulated optical energy gap," *Nano Lett.*, vol. 12, no. 7, pp. 3695–3700, 2012, doi: 10.1021/nl301485q.

[58] B. W. H. Baugher, H. O. H. Churchill, Y. Yang, and P. Jarillo-Herrero, "Optoelectronic devices based on electrically tunable p-n diodes in a monolayer dichalcogenide," *Nat. Nanotechnol.*, vol. 9, no. 4, pp. 262–267, 2014, doi: 10.1038/nnano.2014.25.

[59] M. A. Green, "Photovoltaics: Technology overview," *Energy Policy*, vol. 28, no. 14, pp. 989–998, 2000, doi: 10.1016/S0301-4215(00)00086-0.

[60] X. Wu, Y. hua Wang, P. ling Li, and Z. zhao Xiong, "Research status of MoSe2 and its composites: A review," *Superlattices Microstruct.*, vol. 139, no. September 2019, 2020, doi: 10.1016/j.spmi.2020.106388.

[61] D. Vikraman *et al.*, "Construction of dye-sensitized solar cells using wet chemical route synthesized MoSe2 counter electrode," *J. Ind. Eng. Chem.*, vol. 69, pp. 379–386, Jan. 2019, doi: 10.1016/j.jiec.2018.10.001.

[62] G. Ding, J. He, G. Y. Gao, and K. Yao, "Two-dimensional MoS2-MoSe2 lateral superlattice with minimized lattice thermal conductivity," *J. Appl. Phys.*, vol. 124, no. 16, Oct. 2018, doi: 10.1063/1.5051067.

[63] A. Pospischil, M. M. Furchi, and T. Mueller, "Solar-energy conversion and light emission in an atomic monolayer p-n diode," *Nat. Nanotechnol.*, vol. 9, no. 4, pp. 257–

261, 2014, doi: 10.1038/nnano.2014.14.

[64] J. Morales, "Electrochemical studies of lithium and sodium intercalation in MoSe2," *Solid State Ionics*, vol. 83, no. 1–2, pp. 57–64, Jan. 1996, doi: 10.1016/0167-2738(95)00234-0.

[65] D. Vikraman, S. Hussain, K. Prasanna, K. Karuppasamy, J. Jung, and H.-S. Kim, "Facile method to synthesis hybrid phase 1T@2H MoSe2 nanostructures for rechargeable lithium ion batteries," *J. Electroanal. Chem.*, vol. 833, pp. 333–339, Jan. 2019, doi: 10.1016/j.jelechem.2018.12.013.

[66] S. M. Auerbach, K. A. Carrado, and P. K. Dutta, *Handbook of Layered Materials*. CRC Press, 2004. doi: 10.1201/9780203021354.

[67] J. Ge *et al.*, "MoSe 2 /N-Doped Carbon as Anodes for Potassium-Ion Batteries," *Adv. Energy Mater.*, vol. 8, no. 29, Oct. 2018, doi: 10.1002/aenm.201801477.

[68] J. M. Soon and K. P. Loh, "Electrochemical double-layer capacitance of MoS2 nanowall films," *Electrochem. Solid-State Lett.*, vol. 10, no. 11, pp. 250–254, 2007, doi: 10.1149/1.2778851.

[69] S. K. Balasingam, J. S. Lee, and Y. Jun, "Few-layered MoSe2 nanosheets as an advanced electrode material for supercapacitors," *Dalt. Trans.*, vol. 44, no. 35, pp. 15491–15498, 2015, doi: 10.1039/c5dt01985k.

[70] H. Tang, K. Dou, C. C. Kaun, Q. Kuang, and S. Yang, "MoSe2 nanosheets and their graphene hybrids: Synthesis, characterization and hydrogen evolution reaction studies," *J. Mater. Chem. A*, vol. 2, no. 2, pp. 360–364, 2014, doi: 10.1039/c3ta13584e.

[71] J. Zhang, T. Wang, P. Liu, Y. Liu, J. Ma, and D. Gao, "Enhanced Catalytic Activities of Metal-Phase-Assisted 1T@2H-MoSe2 Nanosheets for Hydrogen Evolution," *Electrochim. Acta*, vol. 217, pp. 181–186, 2016, doi: 10.1016/j.electacta.2016.09.076.

[72] A. Eftekhari, "Molybdenum diselenide (MoSe2) for energy storage, catalysis, and optoelectronics," *Appl. Mater. Today*, vol. 8, pp. 1–17, 2017, doi: 10.1016/j.apmt.2017.01.006.

[73] T. F. Jaramillo, K. P. Jørgensen, J. Bonde, J. H. Nielsen, S. Horch, and I. Chorkendorff, "Identification of active edge sites for electrochemical H2 evolution from MoS2 nanocatalysts," *Science (80-.).*, vol. 317, no. 5834, pp. 100–102, 2007, doi: 10.1126/science.1141483.

[74] J. Yu *et al.*, "Recent advancements in two-dimensional transition metal dichalcogenide materials towards hydrogen-evolution electrocatalysis," *Green Energy Environ.*, 2024, doi: 10.1016/j.gee.2024.08.009.

[75] Z. Gholamvand *et al.*, "Comparison of liquid exfoliated transition metal dichalcogenides reveals MoSe 2 to be the most effective hydrogen evolution catalyst," *Nanoscale*, vol. 8, no. 10, pp. 5737–5749, 2016, doi: 10.1039/C5NR08553E.

[76] W. Zhai, Y. Ma, D. Chen, J. C. Ho, Z. Dai, and Y. Qu, "Recent progress on the long-term stability of hydrogen evolution reaction electrocatalysts," *InfoMat*, vol. 4, no. 9, pp. 1–43, 2022, doi: 10.1002/inf2.12357.

[77] S. Anju and P. V. Mohanan, "Biomedical applications of transition metal dichalcogenides (TMDCs)," *Synth. Met.*, vol. 271, no. September, p. 116610, 2021, doi: 10.1016/j.synthmet.2020.116610.

[78] Q. Yue, Z. Shao, S. Chang, and J. Li, "Adsorption of gas molecules on monolayer MoS2 and effect of applied electric field," *Nanoscale Res. Lett.*, vol. 8, no. 1, p. 425, Dec. 2013, doi: 10.1186/1556-276X-8-425.

[79] J. Kong *et al.*, "Nanotube Molecular Wires as Chemical Sensors," *Science (80-.).*, vol. 287, no. 5453, pp. 622–625, Jan. 2000, doi: 10.1126/science.287.5453.622.

[80] D. J. Late, T. Doneux, and M. Bougouma, "Single-layer MoSe2 based NH3 gas sensor," *Appl. Phys. Lett.*, vol. 105, no. 23, 2014, doi: 10.1063/1.4903358.

[81] B. Cho *et al.*, "Charge-transfer-based gas sensing using atomic-layer MoS2," *Sci. Rep.*, vol. 5, no. 2, p. 8052, 2015, doi: 10.1038/srep08052.

[82] B. Liu, L. Chen, G. Liu, A. N. Abbas, M. Fathi, and C. Zhou, "High-performance chemical sensing using Schottky-contacted chemical vapor deposition grown monolayer MoS2 transistors," *ACS Nano*, vol. 8, no. 5, pp. 5304–5314, 2014, doi: 10.1021/nn5015215.

[83] Y. Han *et al.*, "Design of Hetero-Nanostructures on MoS2 Nanosheets to Boost NO2 Roomerature Sensing," *ACS Appl. Mater. Interfaces*, vol. 10, no. 26, pp. 22640–22649, 2018, doi: 10.1021/acsami.8b05811.

[84] A. Mishra, J. Narang, C. S. Pundir, R. Pilloton, and M. Khanuja, "Morphology-Preferable MoSe2 Nanobrooms as a Sensing Platform for Highly Selective Apta-Capturing of Salmonella Bacteria," *ACS Omega*, vol. 3, no. 10, pp. 13020–13027, 2018, doi: 10.1021/acsomega.8b01074.

[85] A. Azadbakht and A. R. Abbasi, "Impedimetric aptasensor for kanamycin by using carbon nanotubes modified with MoSe2 nanoflowers and gold nanoparticles as signal amplifiers," *Microchim. Acta*, vol. 186, no. 1, p. 23, Jan. 2019, doi: 10.1007/s00604-018-3130-x.

CHAPTERII:

Computational Methods

II-1-Introduction:

The description of theories and theoretical approximations utilized in numerical computations will be the main topic of this chapter. Since the resolution of the multi-electron Schrödinger equation, which is the closest to the real physical system, is necessary for the theoretical calculation of various physical and chemical properties of materials, it must be simplified to a system of one-electron equations. For this approximation, the density functional theory (DFT) are used, which is one of the most significant computational theories adopted for various approximations and the most significant computational methods applied in simulation programs to find the fundamental energy states of atomic systems.

However, the use of specific approximations varies depending on the system and the kind of properties being investigated. For example, the pseudopotential approach is utilized for semiconductors and supercell systems, and the **Quantum Espresso** package can be used to make the nemuric summation.

II-2- Total Hamiltonian for the Crystal:

The crystal system is formed by a collection of nuclei and electrons that interact with each other. The Schrödinger equation defines the stable state of the crystal system [1], and make the ability to specify the wave function's energy. The Schrödinger equation is formulated as follows:

$$H\psi(R,r) = E\psi(R,r) \qquad \text{(II-1)}$$

Where:R : Represents the positions of the nuclei.

r: Denotes the positions of the electrons.

E:Represent the total energy of system.

H: The entire crystal Hamiltonian caused by The electrostatic interaction between electrons and nuclei and denoted by :

$$\text{(II-2)} \quad H = T_e + T_n + V_{ee} + V_{en} + V_{nn}$$

$$H = \sum_i \frac{-h^2}{2m}\Delta_i + \sum_k \frac{-h^2}{2M}\Delta_k + \sum_{i\neq j} \frac{e^2}{8\pi\varepsilon_o\left|\vec{r}_i - \vec{r}_j\right|} - \sum_{i,k} \frac{z_k e^2}{4\pi\varepsilon_0\left|\vec{R}_k - r_i\right|} + \sum_{k\neq l} \frac{z_k z_l e^2}{8\pi\varepsilon_0\left|\vec{R}_k - \vec{R}_l\right|} \qquad \text{(II-3)}$$

T_e : The electron kinetic energy.

T_n : The nuclei kinetic energy.

V_{ee} : The electron-electron interaction energy (pairwise).

V_{en} **:** The interaction energy between electrons and nuclei.

V_{nn} **:** The nucleus-nucleus interaction energy (pairwise).

e : The charge of an electron.

m : The mass of an electron.

M : The mass of a nucleus.

r_i, r_j : The positions of the i-th and j-th electrons, respectively.

R_k, R_l : The positions of the k-th and l-th nuclei, respectively.

z_k, z_l : The atomic numbers of the k-th and l-th nuclei, respectively.

The Schrodinger equation cannot be solved generally due to a large amount of variants 3(Z+1)N, where N and Z are the number of atoms and atomic number, respectively.

Robert Oppenheimer and Max Born proposed an approximation to make the Schrodinger equation solutions simpler, which will be discussed in the next title [2].

II-3- Born-Oppenheimer Approximation:

It is also known as the adiabatic approximation. In this approximation, the nucleus is statically stable because the electron mass is negligible in comparison to the nucleus's mass and the nucleus velocity is also negligible in comparison to the electron velocity. In this scenario, the Hamiltonian is expressed in terms of the electron variations and takes the form [3]:

$$H = T_e + V_{ee} + V_{en} \tag{II-4}$$

$$H = \sum_i \frac{-h^2}{2m}\Delta_i + \sum_{i\neq j}\frac{e^2}{8\pi\varepsilon_o\left|\vec{r}_i - \vec{r}_j\right|} - \sum_{i,k}\frac{z_k e^2}{4\pi\varepsilon_0\left|\vec{R}_k - r_i\right|} \tag{II-5}$$

The Schrödinger equation in this approximation is written as follows:

$$H_e\psi_e(R,r) = E_e\psi_e(R,r) \tag{II-6}$$

Despite this simplification, the complexity of electron-electron interaction makes solving the Schrodinger equation challenging; therefore, an alternative approximation, such as the Hartre-Fock approximation, is necessary.

II-4- Hartree-Fock Approximation:

In 1928, Can Hartree originally presented the one-electron approximation as a solution to the problem of many electrons. Based on the independent electron hypothesis, this approximation suggests that each electron evolves in an average potential that is produced by the other electrons and the nuclei[4].

A sum of Hamiltonians can then be used to express the Hamiltonian:

(II-7) $H_e = \sum_{i=1}^{n} H_i$

An individual electron's Hamiltonian can be written as follows:

$$H_i = -\frac{h^2}{2m}\Delta_i + u_i(\vec{r}_i) + V_i(\vec{r}_i) \quad \text{(II-8)}$$

$u_i(\vec{r}_i)$ indicates an electron's i potential energy in the field of all nuclei k, as given by the following relation:

(II-9) $u_i(r_i) = -\sum_k \frac{z_k}{\left|\vec{r}_i + \vec{R}_k^0\right|}$

Where, $\vec{R}_K^{\,0}$ indicates the position of the nuclei.

As for $V_i(\vec{r}_i)$, it represents the effective potential and given by:

$$V_i(\vec{r}_i) = \frac{1}{2}\sum_j \frac{1}{\left|\vec{r}_i + \vec{r}_j\right|} \quad \text{(II-10)}$$

The electrical system's wave function is expressed as follows since it is the product of the electrons' wave functions:

(II-11) $\psi(\vec{r}_1, \vec{r}_2, \vec{r}_3, ...\vec{r}_n) = \psi(\vec{r}_1)\psi(\vec{r}_2)\psi(\vec{r}_3)...\psi(\vec{r}_n)$

In this context, the sum of the energies corresponding to each electronic state is considered the total energy:

(II-12) $E = E_1 + E_2 + E_3 + ...E_n$

Thus, the Schrodinger equation for an electron is written as follows:

$$\varepsilon_i\psi_i(r) = \left[-\frac{\hbar}{2m} - \sum_k \frac{z_k}{\left|\vec{r}_i + \vec{R}_k^0\right|} + \frac{1}{2}\sum_j \frac{1}{\left|\vec{r}_i + \vec{r}_j\right|}\right]\psi_i(r) \quad \text{(II-13)}$$

Since the electrons are regarded as having no spin in this approximation, the solutions are not antisymmetric. Fock corrected this by proposing the Pauli exclusion principle [5], which makes the electronic wave function antisymmetric with regard to the exchange of two electrons and expressed as a Slater determinant made up of mono-electronic functions.

$$\psi(\vec{r}_1,\vec{r}_2,\vec{r}_3,..\vec{r}_n)=\frac{1}{\sqrt{n!}}\begin{vmatrix}\psi_1(\vec{r}_1) & \psi_1(\vec{r}_2)\cdots\cdots\psi_1(\vec{r}_n)\\ \psi_2(\vec{r}_1) & \psi_2(\vec{r}_2)\cdots\cdots\psi_2(\vec{r}_n)\\ \vdots & \vdots \quad\quad \vdots\\ \psi_n(\vec{r}_1) & \psi_n(\vec{r}_2)\cdots\cdots\psi_n(\vec{r}_n)\end{vmatrix} \quad \text{(II-14)}$$

In which the normalizing constant is $\frac{1}{\sqrt{n!}}$

Although this approximation is used in quantum chemistry to treat atoms and molecules, solids cannot be treated with it. However, the density functional theory (DFT) a more advanced and potent approach has emerged.

II-5-Density Functional Theory (DFT):

This theory's model dates back to 1927, when Thomas and Fermi developed it [5, 6].It took on its current form in 1964 thanks to studies by Kohn and Hohenberg in 1964 [8] and Kohn and Sham in 1965 [9], and it will become the most popular approach in condensed matter physics and quantum chemistry this century.

According to this theory, the electronic density $\rho(r)$ is an essential variable, and every system's total energy may be represented as a functional of the electronic density.

II-5-1-Thomas-Fermi model:

In 1928, Thomas [6] and Fermi [10] proposed a model that divides the **Brillouin** region into very small divisions, with the electron density in each divided region being considered constant. This model determines the total energy of a heterogeneous electron gas as a function of electron density, suggestingthat it is proportional to $[\rho(r)]^{\frac{5}{3}}$.

This theory disregards electronic bonding and is a local approximation of the electron density.

II-5-2- Dirac model:

In 1930, Dirac[11]introduced their model to enhance the Tomas-Fermi model. They suggested that exchange effects might be explained by adding a factor derived from the exchange energy density in a homogenous gas of electrons. The Dirac model's primary problem is its inability to replicate an atom layer's electrical structure.

II-5-3- Theorems of Hohenberg and Kohn:

The term DFT was first introduced in 1964 with the publication of Hohenberg and Khan's publications [8].Finding a mathematical relationship between a system's energy, principal state, and electron density is the main notion of their theorem.They suggest two lemmas that can be applied to any system of interacting particles evolving in an external potential.

Lemma 1*:* Since the ground state of the electron density ρ(r) represents the external potential, the energy functional is given as a function of ρ(r). Consequently, a system's ground state energy in an external potential with multiple electrons is stated as follows:

$$E = E[\rho(r)] \tag{II-15}$$

Lemma 2 (variational principle) : The exact density of the ground state is the density that gives rise to the precise energy of the ground state, which is the minimal value of the total energy functional. And, the density of the ground state $\rho_0(r)$ determines the other ground state characteristics. Consequently, the ground state's total energy $E[(\rho_0(r)]$ is expressed as follows:

$$E[(\rho_0(r)] = \min E[\rho(r)] \tag{II-16}$$

The function of the total energy of the fundamental state is expressed as follows:

$$E[(\rho\ (r)] = F[\rho\ (r)] + \int V(r)\rho\ (r)dr \tag{II-17}$$

Where, $V(r)$: The external potential.

$F[\rho\ (r)]$: Represents the Hohenberg-Kohn density functional, which doesn't reveal anything about the excited state; it just establishes the ground state's characteristics and it’s not precisely defined. This is how it was presented:

$$F[\rho(r)] = T[\rho(r)] + V_{ee}[\rho(r)] \tag{II-18}$$

Where, $T[\rho(r)]$: The kinetic energy of systeme.

$V_{ee}[\rho(r)]$: The potential of electron-electron interaction.

However, this theory does not specify the analytical expression for these two quantities.

The Hohenberg-Kohn theorems has generally demonstrated its efficacy in "ab initio" computations used to investigate the electrical characteristics of materials.

II-5-4- Kohn-Sham equations

In 1965, Khan and Sham [9]suggested a hypothetical system for independent electrons whose ground state and electron density were identical to those of the real system of interacting electrons in order to calculate the Hohenberg-Kohn functional.

kohn and Shamadded that an imagined non-interacting system was used in place of the real interactive system, with the density being the same.

To apply the Kohn-Sham theory, we write as follows:

$$E[\rho(r)] = T_S[\rho(r)] + E_H[\rho(r)] + V_{ext}[\rho(r)] + E_{XC}[\rho(r)] \quad \text{(II-19)}$$

Where: $T_S[\rho(r)]$Represents the kinetic energy in the Slater determinant for non-interacting electrons, which is expressed as follows:

$$T_S[\rho(r)] = \sum_i \left\langle \psi_i \left| -\frac{\hbar^2}{2m}\nabla_r^2 \right| \psi_i \right\rangle \quad \text{(II-20)}$$

$E_H[\rho(r)]$ Represents the Coulomb interaction between electrons, often known as the Hartree term, it's presented by the following expression:

$$E_H[\rho(r)] = \frac{1}{2}\iint \frac{\rho(r)\rho(r')}{|r-r'|} dr dr' \quad \text{(II-21)}$$

$V_{ext}[\rho(r)]$ contains the Coulomb interaction between nuclei and electrons as well as the interaction between nuclei.

$E_{XC}[\rho(r)]$ represents the exchange-correlation term, which comprises the total mistake arising from the non-interacting kinetic energy as well as the Coulomb interactions. It is expressed as:

$$E_{XC}[\rho(r)] = \int \rho(r)\varepsilon_{XC}[\rho(r)] dr \quad \text{(II-22)}$$

The exchange-correlation energy is linked to the exchange-correlation potential, which can be determined with the following formula:

$$V_{XC}[\rho(r)] = \frac{\delta E_{XC}[\rho(r)]}{\delta\rho(r)} \quad \text{(II-23)}$$

From this, the Kohn-Sham equation can be derived as follows:

$$\left[-\frac{\hbar^2}{2m}\nabla_r^2 + V_{eff}(r)\right]\psi_i = \varepsilon_i\psi_i \quad \text{(II-24)}$$

ψ_i

Where ε_i $V_{eff}(r)$ represents theLagrange multiplier, and the solution is referred to as the Kohn-Sham orbitals, and indicates The effective potential that each electron feels as a result of the other electrons and the nuclei is determined by:

$$V_{eff}(r) = V_{ext}(r) + V_H + V_{XC}(r) \qquad \text{(II-25)}$$

II-5-5-Solutions of Kohn-Sham equations

The independent electron wave functions determine the electron density, which in turn determines the potential obtained from the density.

This determines the V_{XC} potential in the Khon-Sham equation. For iteration to solve these equations, self-consistency must be approached. An initial charge density $\rho_{in}(r)$ and an initial estimate for the Kohn-Sham orbitals ψ_i are needed for this.

Following the computation of the effective potential, $V_{eff}(r)$ the Kohn-Sham equations were solved to yield the revised density $\rho_{new}(r)$. Should the result fail to meet the convergence condition, the process is repeated by mixing the initial and new charge densities. An illustration of the self-consistent cycle can be viewed in **Figure II.1.**

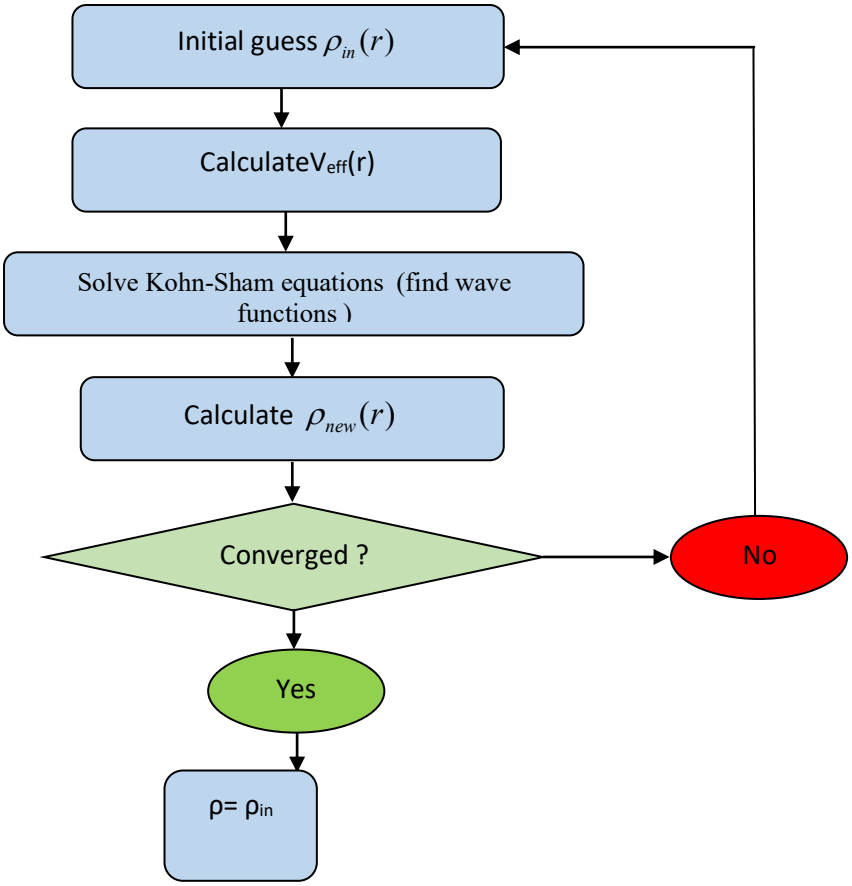


Figure II.1: Schematic representation of the self-consistency cycle in Kohn-Sham density functional theory calculations.

II-5-6- Functional Exchange-correlation:

The Kohn-Sham results only determine the ground state's minimum potential, known as the Kohn-Sham potential $V_{KS}(r) = V_{\min}^{eff}$, and the exchange-correlation energy of the Khon-sham equations is unknown. This result made it difficult to apply DFT in practice, so it was necessary to propose a formulation for the exchange-correlation energy $E_{XC}[\rho(r)]$ that attracted the attention of researchers in order to propose approximations, some of which are as follows:

II-5-6-1- Local Density Approximation (LDA):

In 1965, Khon and Sham suggested this approximation[12], assuming that the electron density varied slowly enough toward the system's interior and considered the heterogeneous electronic system as a homogeneous one. The energy-correlation exchange function can be described locally as follows:

$$E_{XC}^{LDA}[\rho(r)] = \int \varepsilon_{XC}^{LDA}[\rho(r)]\rho(r)dr \qquad \text{(II-26)}$$

Where ε_{XC} indicates a particle's exchange-correlation energy in a uniform gas of electrons with density $\rho(r)$, which can be divided Into separate exchange and correlation components:

$$\varepsilon_{XC}^{LDA}[\rho(r)] = \varepsilon_{X}^{LDA}[\rho(r)] + \varepsilon_{C}^{LDA}[\rho(r)] \quad \text{(II-27)}$$

We can use the following expression to compute the exchange energy $\varepsilon_X[\rho(r)]$ analytically:

$$\varepsilon_{X}^{LDA}[\rho(r)] = -\frac{3}{4}\left(\frac{3}{\pi}\rho(r)\right)^{\frac{1}{3}} \quad \text{(II-28)}$$

Although the exchange-correlation energy $\varepsilon_{XC}[\rho(r)]$ functional form is undetermined quantum simulations based on the homogeneous electron gas have given an accurate numerical approximation, which has been used in Monte Carlo calculations [13].

Furthermore, other methods have been developed to obtain correlation energy approximations utilizing various analytical forms, such as Vosko-Wilk-Nusair (VWN)[14], Perdew-Zunger (PZ81)[15], Cole-Perdew (CP)[16], and Perdew-Wang (PW92) [17].

II-5-6-2-Generalized Gradient Approximation (GGA) :

The LDA approximation is improved by the GGA approximation, which also restores the LDA approximation's proven and validated characteristics.

The exchange-correlation term in GGA approximation is taken into consideration as a function of the density $\rho(r)$ and its gradient $\nabla(\rho)$, which also accounts for the density's inhomogeneity. The following is how the exchange-correlation energy $E_{XC}^{GGA}[\rho(r)]$ is expressed in the GGA approximation [18, 19]:

$$E_{XC}^{GGA}[\rho(r)] = \int f_{XC}[\rho(r), \nabla\rho(r)]\rho(r)dr \quad \text{(II-29)}$$

Where, f_{XC} represents an enhancement factor and is a function of the local density and its gradient.

on the other hand, the exchange energy in GGA approximation difinedas :

$$E_{X}^{GGA} = \int \rho(r)\varepsilon_{X}^{LDA}(\rho) f_X(s)dr \quad \text{(II-30)}$$

The factor f_X has various forms, including Wu-Cohen (WC)[20], Engel-Vosko (EV)[21] , Becke (B88)[18], Perdew-Wang (PW91) [22], and Perdew-Burke-Ernzerhof (PBE)[19].

Because of its accuracy and adaptability, we only employed the PBE functional in our work. It is important to note that the GGA approximation, in all of its variations, has shown

remarkable efficiency in computations concerning metal magnetism, molecular bonding, and the electronic properties of semiconductors, metals, and surfaces.

II-5-5-1-a- Approximation PBE-GGA:

The GGA is enhanced by the PBE approximation[19].

Its first and second order gradients, which are part of its enhancement factor, and the local electron density define it. The following presents this factor's form:

$$f_x(s) = 1 + \kappa - \frac{\kappa}{1 + \mu s^2 / \kappa} \qquad \text{(II-31)}$$

Where, s presents the reduced density gradient, difined by:

$$s = \frac{|\nabla \rho|}{2 k_F \rho} \qquad \text{(II-32)}$$

k_F is the Fermi wave vactor, known as :

$$k_f = (3\pi^2 \rho)^{\frac{1}{3}} \qquad \text{(II-33)}$$

And, the empirical constants $\kappa = 0{,}804$ and $\mu = 0{,}21951$ where, selected to meet physical requirements.

As compared to LDA and previous GGA functionals, the PBE-GGA approximation balances theoretical consistency, computational efficiency, and precision.

The GGA-PBE version has specifically improved the solids compression coefficient and structural characteristics. It is commonly utilized in the study of magnetic and surface properties and in the computation of electronic properties like energy levels and band gaps, particularly for semiconductors and transition metal compoundes.

It is sufficiently precise for application in phase transitions, molecular bonding, and two-dimensional materials.

II-6- The Plane Wave (PW):

The free Schrödinger equation can be solved using the plane wave function, which is used in DFT to represent the electrons in a crystal[23]. It looks like this:

$$\varphi_k(r) = e^{ikr} \qquad \text{(II-34)}$$

where, r presents the position vector in space.

k is the wave vector associated with the momentum of the electron.

e^{ikr} is a periodic function, ideal for describing electrons in a crystal.

The electronic wave function, or the real wave function of the electron in a crystal, must be defined since the electron in a crystal is not free and senses the periodic potential of the atoms. This can be done by solving the Schrödinger equation [24]. The electronic wave function must be periodic according to the Bloch lattice, and it represented as follows:

$$\psi_k(r) = u_k(r)e^{ikr} \tag{II-35}$$

where, u_k is a periodic function that can be expressed as a Fourier series in the basis of reciprocal vectors G and has the same periodicity as the crystal lattice :

$$u_k(r) = \sum_G C_G e^{iGr} \tag{II-36}$$

Where C_G is the Fourier coefficient wich dependent to the crystal potential and the electronic state.

Replacing this expression in the Bloch equation:

$$\psi_k(r) = \sum_G C_G e^{i(k+1)r} \tag{II-37}$$

II-7-Pseudopotential Approximation:

There are two kinds of electrons: valence electrons, which exist outside the core, and core electrons, which are attached to the inner shells of atoms. Since core electrons usually do not take part in the chemical reactions, it is computationally costly and takes a long time for the calculation to converge when all electrons are included. In the pseudopotential approximation, core electrons are neglected within the framework of DFT theory, only valence electrons are taken into account.

Fermi first put forth the concept of pseudopotential in relation to nuclear interactions in 1934[25].

Additionally, Phillips [26], Hellmann [27], and Gombás [28]created this method in 1940–1950 to make electrical wave computations easier. Cohen and Heine [29]then, used the idea to calculate the electronic structures of solids in 1960. Then, in the 1990, Troullier-Martins and Vanderbilt [30] improved pseudopotentials to increase their accuracy and effectiveness in ab initio computations.

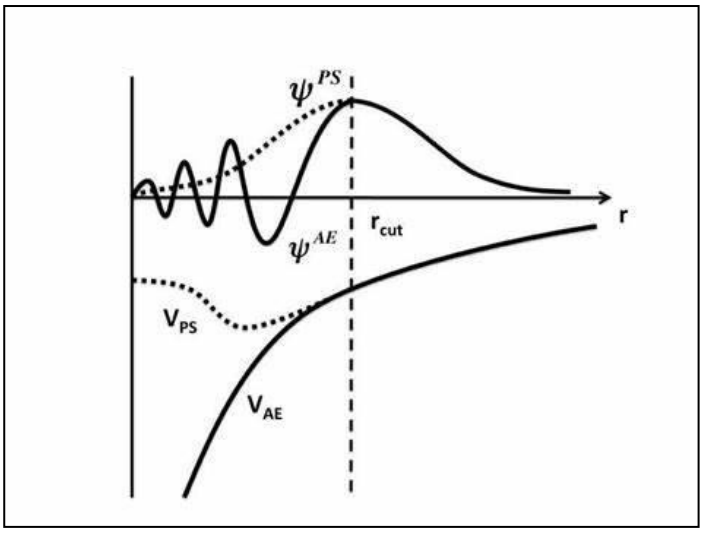


Figure II-2: Schematic illustration of the pseudopotential concept, where, ψ^{PS} , ψ^{AE}, V_{PS} , V_{AE} and r_{cut} corresponding the pseudo-wavefunction, all electron-wavefunction, pseudo-potential, all electron-potential and the cutoff radius, respectively.

A pseudo-wave function is used in place of the all-electron wave function which is strongly oscillates near the nucleus due to the Coulomb potential in this approximation, and the pseudopotential for all electrons is used in place of the total potential for all electrons.

In the **Figure II-2** shows the diagram for these variables. The pseudo-wave function ψ^{PS} and the all-electron wave function ψ^{AE} which is are identical outside the specified cutoff radius, as the graph illustrates.

The all-electron potential V_{AE} and the pseudopotential V_{PS} share the same dispersion characteristics. This highlights the significance of selecting the cutoff radius r_{cut} with care[31,32].

The general form of pseudopotential is given as :

$$V_{PS}(r) = V_{local}(r) + \sum_{l} |l\rangle V_l^{NL}(r)\langle l| \quad \text{(II-38)}$$

Where, $V_{local}(r)$ is the local potential.

V_l^{NL} is the nonlocal potential, wich depends on the engular moment l.

The benefit of using a very limited number of plane waves to represent the pseudo wave functions in Fourier space is that it would significantly minimize the need for numerical calculations. The pseudopotential's form is selected to ensure that the energies of all electron wave functions and pseudo wave functions are equal [33].

It discovered several kinds of pseudo potential, including Norm-Conserving, Ultra-Soft pseudopotentials and Pojected Augmented-wave.

II-7-1- Norm-Conserving Pseudopotential (NC)

Hamann, Schluter, and Chiang (HSC) introduced norm-conserving pseudopotentials in 1979 [34], with the goal of making quantum mechanical computations easier by using a pseudopotential to describe the core electron effect. The reason these pseudopotentials are referred to as "norm-conserving" is that both the real charge and the real wave function's characteristics are preserved in the core region.

The norm-conservative approach guarantees a good reproduction of the electronic forces and characteristics by requiring that the integral of the pseudo electron density in a region equal that of the real electron wave. The following is the norm-conserving condition :

$$\int_{r\le r_c} \left|\psi_l^{PS}(r)\right|^2 dr = \int_{r\le r_c} \left|\psi_l(r)\right|^2 dr \quad \text{(II-39)}$$

The NC pseudopotential exhibits conserved charge, good convergence, and great precision but it is costly since it needs a large number of plane waves.

II-7-2- Ultra-Soft Pseudopotential (US):

David Vanderbilt developed the ultrasoft psodopotential in 1990 [35], to lower the cost of ab initio calculations, minimize the high number of plane waves used in the NC pseudopotential, and accurately depict the wave states of valence electrons, particularly for elements with d and f orbitals.

The number of plane waves required is decreased by this pseudopotential's relaxation of the norm conservation criterion, which permits even smoother pseudo-wave functions. Although ultrasoft pp can speed up calculations and are perfect for complicated systems and metals, they can occasionally be less precise than Norm-Conserving pseudopotentials.

II-7-3-Projected Pseudo-Potential PAW (Projector Augmented Wave):

Introduced by Blöchl in 1994, the PAW [36], the PAW (Projector Augmented-Wave) method is an advanced approach that enhances the accuracy of ab initio calculations, particularly in DFT.

This method combines excellent precision with a reduction in computational cost. The basis of the PAW is a lineartransformation between two spaces: the all-electron space, which contains the real wave function $\psi(r)$, which is highly oscillatory close to the nuclei, and

the pseudo space, which contains smooth pseudo-wave functions $\psi^{PS}(r)$ wich is simple to represent with plane waves. The first space is utilized for computations throughout the crystal, but the second space is only utilized in the areas near the nucleus [37], The PAW expression that follows is used to transform between the two spaces:

$$\psi = \psi^{PS} + \sum_i (\varphi_i - \overline{\varphi}_i)\left\langle \widetilde{P}_i \middle| \psi^{PS} \right\rangle \text{(II-40)}$$

Where, φ_i : all-electron function in the region near the nucleus.

$\overline{\varphi}_i$: pseudo-function in the region near the nucleus.

$\widetilde{P}_i$:projector of PAW.

The pseudopotential PAW is very precise for electrical and optical properties, and is especially suitable for transition metals, lanthanides, and complicated materials like superalloys and transition metals dichalcogenides [38].

II-8- Plan Wave-Pseudopotential (PW-PP):

Combining the pseudopotential approach (PP) with plane waves (PWs) is advantageous as long as the former are straightforward and well-defined, while the latter reduce the complexity associated with core electrons and the number of plane waves needed in nemuric calculations.

In density functional theory (DFT), the PW-PP approach is frequently used to calculate a material's electronic structure. Compatible with **Quantum ESPRESSO**, **ABINIT**, and **VASP**, among other **DFT packages**.

II-9- Calculation Code:

An ab initio simulation is a computational method to estimate a material's physical and chemical properties using the fundamental principles of quantum mechanics rather than experimental parameters[39].

It primarily uses the Schrödinger equation and Density Functional Theory (DFT) to compute the electronic structure, total energy, interatomic forces, and other properties of materials.

An ab initio simulation program is chosen based on the type of material researched, the computational method required, and the computing resources available. For example, for studying the physical properties such as electronic, phononic, optical properties,..) of bulk and

two- dimential solid materials using the DFT and the PW-PP method, we can utilize several simulation programs such as ABINIT and **Quantum ESPRESSO.**

Quantum ESPRESSO is a modeling software whose name is separated into two parts: "**Quantum**" relates to quantum mechanics, and "**ESPRESSO**" refers to an open source package produced for electronic structure simulation, optimization, ..etc[40].

The program focuses on solving DFT problems with methods and algorithms that accurately describe chemical systems [41], It's based on the plane wave and pseudopotential (PW-PP) method [42]. The codes are also constructed using periodic boundary conditions, which means the system is treated as repeating periodically in space.

Basic calculations that can be performed using Quantum Espresso include the following[40] :

- **Relaxation step.** In Quantum ESPRESSO, relaxing is the process of adjusting atomic locations and lattice characteristics to reduce the total energy and forces acting on the atoms. This confirms that the system reaches its most stable configuration before doing any further electrical structure computing.
- **The Self-Consistent Field (SCF) calculation**. Whichis an important stage in Density Functional Theory (DFT) computations. It computes the ground-state electron density by iteratively solving the Kohn-Sham equations until self-consistency occurs [9].
- **Magnetic ground state calculations**.Including**spin-orbit coupling**and**non-collinear magnetism**[45,46].Quantum ESPRESSO involves using the DFT framework to determine if a material is ferromagnetic (FM), antiferromagnetic (AFM), or nonmagnetic (NM) based on spin polarization.
- **Response properties**. These include phonon frequencies and eigenvectors [47], phonon dispersions[48], electron-phonon interactions [49], effective charges, and dielectric tensors [50]. These properties describe how the system responds to external perturbations, such as vibrations, electric fields and magnetic fields.
- **Optical properties and spectroscopic properties.**This involves the calculation of optical response characteristics, such as absorption and scattering of light, as well as spectroscopic features like spectra that describe the interaction of light with the material [51, 52].
- **Electronic Band Structure Calculations**.It describes the link between electron energy levels and momentum, which contributes to the determination of important

properties like as conductivity, band gaps, and effective masses. It is essential for semiconductors, metals, insulators, and two-dimensional materials.

- **Density of States (DOS)**.It describes the number of electronic states available at each energy level. It is useful for analyzing electrical structure, band gaps, metallic vs. insulating behavior, and orbital hybridization.
- **Electron Density and Charge Distribution.** describehow electrons are spatially distributed in a material**.** This is important for understandingchemical bonding, charge transfer, and electronic structure**.**
- **Mechanical Properties**. Mechanical characteristics define how a material reacts to external forces including stress, strain, and deformation. These qualities are critical for determining material stability, elasticity, and mechanical strength.
- **Defect and Impurity Calculations**. Its help to Studing the effects of point defects, impurities, dopant in materials and formation energies.
- **Calculating other properties using external packages**. Such as excitonic effects with YAMBO, Seebeck coefficient, electrical conductivity from band structure with BoltzTraP2, and band structure interpolation with WANNIER90, among others. These extra packages are used to broaden the scope of computations, allowing for a more thorough examination of electronic structure, magnetic properties, and other complex behaviors in materials.

II-9-1- Structure of the input data in QUANTUM ESPRESSO software:

Quantum ESPRESSO (QE) uses text input files to define the calculations. Each input file is divided into sections. Each section contains lists of different names and maps that are determined by the needs of the researcher. The names indicate the materials or systems studied, while the maps represent parameters or settings used in the calculations.

Due to their multiplicity, we will mention the most important of them, on which we have relied in our calculations, Here, we used the example of Si crystal.

a- CONTROL Namelist : Which contain global simulation settings.

```
&CONTROL
  calculation = 'scf'   ! Type of calculation: 'scf', 'nscf', 'relax', 'vc-
relax'
  prefix = 'Si'         ! Prefix for output files
pseudo_dir = './pseudo'   ! Directory for pseudopotentials
outdir = './output'    ! Directory for saving results
  verbosity = 'high'    ! Output level: 'low', 'medium', 'high'
```

```
/
```

b- SYSTEM Namelist :It defines the physical system parameters.

```
&SYSTEM
ibrav = 2              ! Bravais lattice index (2 = FCC)
celldm(1) = 10.2       ! Lattice constant in Bohr
nat = 2                ! Number of atoms
ntyp = 1               ! Number of atomic species
ecutwfc = 50.0         ! Plane-wave energy cutoff (Ry)
  occupations = 'smearing'
  smearing = 'gaussian'
  degauss = 0.01         ! Smearing value for metallic systems
/
```

c- ELECTRONS Namelist : Controls electronic convergence

```
&ELECTRONS
conv_thr = 1.0d-8    ! Self-consistency convergence threshold
mixing_beta = 0.7    ! Mixing parameter for SCF cycles
diagonalization = 'david'  !Diagonalizationmethod
/
```

d- ***ATOMIC_SPECIES :***It describes atomic elements and their pseudopotentials with the format :Element, Atomic Mass, Pseudopotential File.

```
ATOMIC_SPECIES
Si  28.0855Si.pbe-nc.UPF
```

e- ATOMIC_POSITIONS: *Defines atomic positions in different units.*

```
ATOMIC_POSITIONS {angstrom}
Si  0.000.00  0.00
Si  1.351.35  1.35
```

f- ***K_POINTS:*** *Defines k-point sampling for Brillouin zone integration:*

```
K_POINTS automatic
  4 4 4  1 1 1
```

II-9-2- QUANTUM ESPRESSO algorithm :

The **Figure II-3**illustrates the general sequence of the **QUANTUM ESPRESSO** algorithm based on Density Functional Theory (DFT)**.** It begins with the initialization of essential input parameters such as the atomic structure and exchange-correlation functionals. At the core of the process lies the Self-Consistent Field (SCF) cycle, which involves solving the Kohn-Sham equations iteratively: an initial electron density is used to solve the equations, yielding new wavefunctions, from which an updated electron density is computed. This cycle repeats until self-consistency is achieved. Once a stable solution is reached, post-

SCFcalculations are performed to extract key physical properties such as bandstructure, density of states (DOS), and optical or vibrational characteristics. Finally, the algorithm outputs results including the total energy, optimized atomic structure, and forces and stresses within the system.

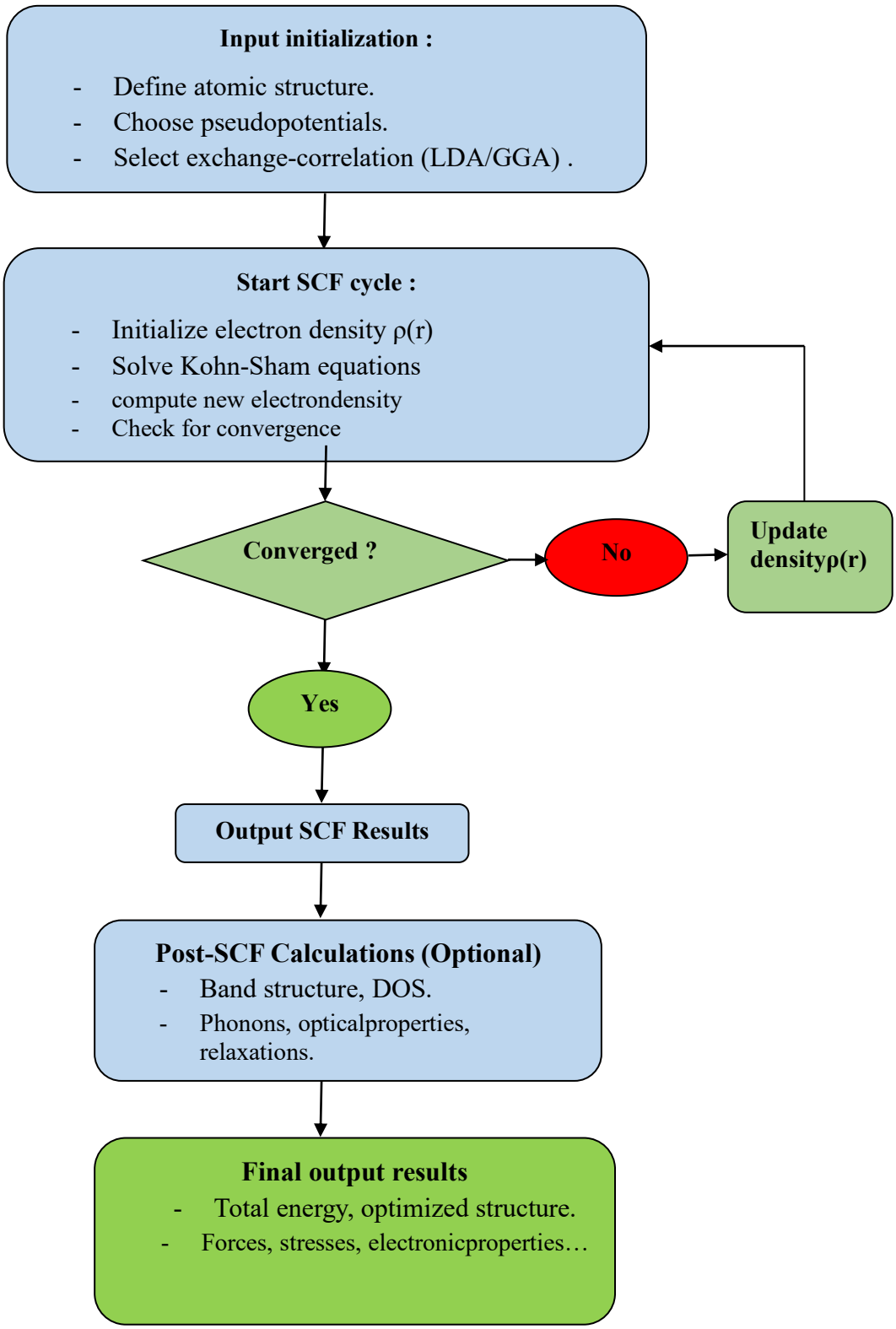


Figure II-3: Schematicrepresentation of the QUANTUM ESPRESSO algorithm.

References:

[1] H. Mathieu, *Physique des Semiconducteurs et des Composants électronique*, 4eme ed. masson, 1998.

[2] S. V. Kireev, Piotr S and Medvedev, *La physique des semiconducteurs*. Mir, 1975.

[3] D. Terme, S. Beitrag, D. Grund, and V. Standpunkte, “Der physik 1.,” 1927.

[4] D. R. Hartree, “The Wave Mechanics of an Atom with a Non-Coulomb Central Field,” *Math. Proc. Cambridge Philos. Soc.*, vol. 24, no. 1, pp. 89–110, 1927.

[5] V. Fock, ?“Selfconsistent field? mit Austausch f?r Natrium,” *Zeitschrift fr Phys.*, vol. 62, no. 11–12, pp. 795–805, Nov. 1930, doi: 10.1007/BF01330439.

[6] L. H. Thomas, “The calculation of atomic fields,” *Math. Proc. Cambridge Philos. Soc.*, vol. 23, no. 5, pp. 542–548, 1927, doi: 10.1017/S0305004100011683.

[7] E. Fermi, “Eine statistische Methode zur Bestimmung einiger Eigenschaften des Atoms und ihre Anwendung auf die Theorie des periodischen Systems der Elemente,” *Zeitschrift für Phys. Phys.*, vol. 48, no. 1–2, pp. 73–79, Jan. 1928, doi: 10.1007/BF01351576.

[8] P. Hohenberg and W. Kohn, “Inhomogeneous Electron Gas,” *Phys. Rev.*, vol. 136, no. 3B, pp. B864–B871, Nov. 1964, doi: 10.1103/PhysRev.136.B864.

[9] W. Kohn and L. J. Sham, “Self-Consistent Equations Including Exchange and Correlation Effects,” *Phys. Rev.*, vol. 140, no. 4A, pp. A1133–A1138, Nov. 1965, doi: 10.1103/PhysRev.140.A1133.

[10] E. Fermi, “Eine statistische Methode zur Bestimmung einiger Eigenschaften des Atoms und ihre Anwendung auf die Theorie des periodischen Systems der Elemente,” *Zeitschrift f?r Phys.*, vol. 48, no. 1–2, pp. 73–79, Jan. 1928, doi: 10.1007/BF01351576.

[11] P. A. M. Dirac, “Note on Exchange Phenomena in the Thomas Atom,” *Math. Proc. Cambridge Philos. Soc.*, vol. 26, no. 3, pp. 376–385, Jul. 1930, doi: 10.1017/S0305004100016108.

[12] D. D. Koelling and B. N. Harmon, “A technique for relativistic spin-polarised calculations,” *J. Phys. C Solid State Phys.*, vol. 10, no. 16, pp. 3107–3114, Aug. 1977, doi: 10.1088/0022-3719/10/16/019.

[13] D. M. Ceperley and B. J. Alder, "Ground State of the Electron Gas by a Stochastic Method," *Phys. Rev. Lett.*, vol. 45, no. 7, pp. 566–569, Aug. 1980, doi: 10.1103/PhysRevLett.45.566.

[14] S. H. Vosko, L. Wilk, and M. Nusair, "Accurate spin-dependent electron liquid correlation energies for local spin density calculations: a critical analysis," *Can. J. Phys.*, vol. 58, no. 8, pp. 1200–1211, Aug. 1980, doi: 10.1139/p80-159.

[15] J. P. Perdew and A. Zunger, "Self-interaction correction to density-functional approximations for many-electron systems," *Phys. Rev. B*, vol. 23, no. 10, pp. 5048–5079, 1981, doi: 10.1103/PhysRevB.23.5048.

[16] L. A. Cole and J. P. Perdew, "Calculated electron affinities of the elements," *Phys. Rev. A*, vol. 25, no. 3, pp. 1265–1271, Mar. 1982, doi: 10.1103/PhysRevA.25.1265.

[17] J. P.Perdew and Y. Wang, "Perdew Wang 1992.Pdf." p. 6.

[18] A. D. Becke, "Density-functional exchange-energy approximation with correct asymptotic behavior," *Phys. Rev. A*, vol. 38, no. 6, pp. 3098–3100, Sep. 1988, doi: 10.1103/PhysRevA.38.3098.

[19] J. P. Perdew, K. Burke, and M. Ernzerhof, "Generalized Gradient Approximation Made Simple," *Phys. Rev. Lett.*, vol. 77, no. 18, pp. 3865–3868, Oct. 1996, doi: 10.1103/PhysRevLett.77.3865.

[20] Z. Wu and R. E. Cohen, "More accurate generalized gradient approximation for solids," *Phys. Rev. B*, vol. 73, no. 23, p. 235116, Jun. 2006, doi: 10.1103/PhysRevB.73.235116.

[21] J. P. Perdew *et al.*, "Atoms, molecules, solids, and surfaces: Applications of the generalized gradient approximation for exchange and correlation," *Physical Review B*, vol. 46, no. 11. pp. 6671–6687, 1992. doi: 10.1103/PhysRevB.46.6671.

[22] J. P. Perdew and Y. Wang, "Accurate and simple analytic representation of the electron-gas correlation energy," *Phys. Rev. B*, vol. 45, no. 23, pp. 13244–13249, Jun. 1992, doi: 10.1103/PhysRevB.45.13244.

[23] N.W. Ashcroft & N.D. Mermin, "Ashcroft mermin ," in *Solid state physic*, 1976.

[24] R. M. Martin, *Electronic Structure*. Cambridge University Press, 2004. doi:

10.1017/CBO9780511805769.

[25] E. Fermi and G. Gallavotti, “An attempt to a β rays theory (translation),” *Z.Phys*, vol. 88, pp. 161–177, 1934, [Online]. Available: http://inspirehep.net/record/1593707

[26] J. C. Phillips and L. Kleinman, “New Method for Calculating Wave Functions in Crystals and Molecules,” *Phys. Rev.*, vol. 116, no. 2, pp. 287–294, Oct. 1959, doi: 10.1103/PhysRev.116.287.

[27] “Enführung in die Quantenchemie,” *Nature*, vol. 141, no. 3572, pp. 667–668, Apr. 1938, doi: 10.1038/141667a0.

[28] L. Szasz, “Pseudopotential Theory of Atoms and Molecules. I. A New Method for the Calculation of Correlated Pair Functions,” *J. Chem. Phys.*, vol. 49, no. 2, pp. 679–691, Jul. 1968, doi: 10.1063/1.1670125.

[29] B. J. Austin, V. Heine, and L. J. Sham, “General Theory of Pseudopotentials,” *Phys. Rev.*, vol. 127, no. 1, pp. 276–282, Jul. 1962, doi: 10.1103/PhysRev.127.276.

[30] N. Troullier and J. L. Martins, “Efficient pseudopotentials for plane-wave calculations,” *Phys. Rev. B*, vol. 43, no. 3, pp. 1993–2006, Jan. 1991, doi: 10.1103/PhysRevB.43.1993.

[31] D. R. Hamann, M. Schlüter, and C. Chiang, “Norm-Conserving Pseudopotentials,” *Phys. Rev. Lett.*, vol. 43, no. 20, pp. 1494–1497, 1979, doi: 10.1103/PhysRevLett.43.1494.

[32] G. B. Bachelet, D. R. Hamann, and M. Schlüter, “Pseudopotentials that work: From H to Pu,” *Phys. Rev. B*, vol. 26, no. 8, pp. 4199–4228, Oct. 1982, doi: 10.1103/PhysRevB.26.4199.

[33] M. Ferhat, A. Zaoui, M. Certier, and H. Aourag, “Electronic structure of BN, BP and BAs,” *Phys. B Condens. Matter*, vol. 252, no. 3, pp. 229–236, Jul. 1998, doi: 10.1016/S0921-4526(98)00149-5.

[34] G. B. Bachelet, H. S. Greenside, G. A. Baraff, and M. Schlüter, “Structural-energy calculations based on norm-conserving pseudopotentials and localized Gaussian orbitals,” *Phys. Rev. B*, vol. 24, no. 8, pp. 4745–4752, Oct. 1981, doi: 10.1103/PhysRevB.24.4745.

[35] D. Vanderbilt, "Soft self-consistent pseudopotentials in a generalized eigenvalue formalism," *Phys. Rev. B*, vol. 41, no. 11, pp. 7892–7895, Apr. 1990, doi: 10.1103/PhysRevB.41.7892.

[36] P. E. Bloechl, "Projector augmented-wave method," *Physical Review B*, vol. 50, no. 24. pp. 17953–17979, 1994.

[37] P. E. Blöchl, "Electrostatic decoupling of periodic images of plane-wave-expanded densities and derived atomic point charges," *J. Chem. Phys.*, vol. 103, no. 17, pp. 7422–7428, Nov. 1995, doi: 10.1063/1.470314.

[38] Y.-P. Wang and H.-P. Cheng, "First-principles simulations of a graphene-based field-effect transistor," *Phys. Rev. B*, vol. 91, no. 24, p. 245307, Jun. 2015, doi: 10.1103/PhysRevB.91.245307.

[39] T. D. Kühne, "Second generation Car–Parrinello molecular dynamics," *WIREs Comput. Mol. Sci.*, vol. 4, no. 4, pp. 391–406, Jul. 2014, doi: 10.1002/wcms.1176.

[40] P. Giannozzi *et al.*, "QUANTUM ESPRESSO: A modular and open-source software project for quantum simulations of materials," *J. Phys. Condens. Matter*, vol. 21, no. 39, 2009, doi: 10.1088/0953-8984/21/39/395502.

[41] R. M. D. and E. Gross, *Density Functional Theory An Approach to the Quantum Many-Body Problem*. Springer Berlin Heidelberg, 1990.

[42] W. E. Pickett, "Pseudopotential methods in condensed matter applications," *Comput. Phys. Reports*, vol. 9, no. 3, pp. 115–197, 1989, doi: 10.1016/0167-7977(89)90002-6.

[43] R. P. Feynman, "Forces in Molecules," *Phys. Rev.*, vol. 56, no. 4, pp. 340–343, Aug. 1939, doi: 10.1103/PhysRev.56.340.

[44] O. H. Nielsen and R. M. Martin, "Stresses in semiconductors: Ab initio calculations on Si, Ge, and GaAs," *Phys. Rev. B*, vol. 32, no. 6, pp. 3792–3805, 1985, doi: 10.1103/PhysRevB.32.3792.

[45] A. C. O. F. C. Hartree-fock, S. Rex, J. Joiusaari, and P. Lazzeretti, "The NMR chemical shift tensor provides much more insight than its isotropic average . It is now ex- perimentally accessible both through solid-state and liquid-crystal-solvent NMR experiments , through measurements of spin-lattice relaxation and via mo- (," vol. 123, pp. 339–350, 1988.

[46] R. Car and M. Parrinello, "Unified Approach for Molecular Dynamics and Density-Functional Theory," *Phys. Rev. Lett.*, vol. 55, no. 22, pp. 2471–2474, Nov. 1985, doi: 10.1103/PhysRevLett.55.2471.

[47] R. Liu *et al.*, "Frequencies, eigenvectors, and single-crystal selection rules of k =0 phonons in YBa 2 Cu 3 O 7 − δ : Theory and experiment," *Phys. Rev. B*, vol. 37, no. 13, pp. 7971–7974, May 1988, doi: 10.1103/PhysRevB.37.7971.

[48] R. Meo, A. D. Corso, P. Giannozzi, and S. Cozzini, "Calculation of Phonon Dispersions on the Grid Using Quantum ESPRESSO," *Chem. Mater. Sci. Appl. Grid Infrastructures*, vol. 24, no. September, pp. 165–183, 2009, [Online]. Available: http://users.ictp.it/~pub_off/lectures/lns024/10-giannozzi/10-giannozzi.pdf%0A

[49] R. E. Prange and L. P. Kadanoff, "Transport Theory for Electron-Phonon Interactions in Metals," *Phys. Rev.*, vol. 134, no. 3A, pp. A566–A580, May 1964, doi: 10.1103/PhysRev.134.A566.

[50] S. Scandolo, P. Giannozzi, C. Cavazzoni, S. de Gironcoli, A. Pasquarello, and S. Baroni, "First-principles codes for computational crystallography in the Quantum-ESPRESSO package," *Zeitschrift für Krist. - Cryst. Mater.*, vol. 220, no. 5–6, pp. 574–579, May 2005, doi: 10.1524/zkri.220.5.574.65062.

[51] P. Friedel, M. S. Hybertsen, and M. SchÏter, "Local empirical pseudopotential approach to the optical properties of Si/Ge superlattices," *Phys. Rev. B*, vol. 39, no. 11, pp. 7974–7977, 1989, doi: 10.1103/PhysRevB.39.7974.

[52] P. Schwerdtfeger, J. S. McFeaters, M. J. Liddell, J. Hrušák, and H. Schwarz, "Spectroscopic properties for the ground states of AuF, AuF+, AuF2, and Au2F2: A pseudopotential scalar relativistic Mo/ller–Plesset and coupled-cluster study," *J. Chem. Phys.*, vol. 103, no. 1, pp. 245–252, Jul. 1995, doi: 10.1063/1.469637.

CHAPTER III:

Results and Discussion

III-1-Introduction

In the first chapter, we have shown the importance of 2D transition metal dichalcogenides (2D-TMDCs). They have very important characteristics that suggest them as potential candidates for a wide range of applications in electronic and optoelectronic devices. In this way they have recently attracted significant attention; researchers have explored ways to expand their functionality by introducing various defects. Among this wide family of materials, the molybdenum diselenide ($MoSe_2$) has occupied an important part of the research effort.

In this chapter, we present the results obtained concerning the structural, electronic, and optical properties of the pristine $MoSe_2$ monolayer, as well as its modified forms with different defects. These defects include the substitution of molybdenum (Mo) atom with arsenic (As) atom, the presence of a vacancy at a molybdenum site, and the incorporation of an interstitial As atom.

We specifically investigate the 2H phase of $MoSe_2$ due to its stability. Arsenic (As) doping was selected for its intriguing properties, motivating us to contribute to the study of its effects. Notably, our calculations indicate that the introduced defects do not alter the structural dimensions of $MoSe_2$ crystal.

III-2- Computational Details

The calculations in this work were performed using density functional theory (DFT) within the generalized gradient approximation (GGA). To describe the electronic exchange-correlation effects, we employed the Perdew-Burke-Ernzerhof (PBE) functional. The projector-augmented wave (PAW) method and ultrasoft (US) atomic pseudopotentials (PPs) were utilized[1,2],with pseudopotentials extracted from the Standard Solid State Pseudopotentials (SSSP) library.

All computations were carried out using the Quantum ESPRESSO (QE) software package[1].

A $4\times4\times1$ supercell consisting of 48 atoms was constructed, comprising 32 selenium (Se) atoms and 16 molybdenum (Mo) atoms. When substituting a Mo atom with an arsenic (As) atom, the defect concentration was set to 6,25% relative to the number of Mo atoms. A vacuum layer of 15A° was included in the Z direction to erase interactions between periodic images.

All computational parameters were chosen to ensure convergence. The first Brillouin zone was sampled using a Monkhorst-Pack K-point mesh of $2\times2\times1$ for the self-consistent field

(SCF) calculations, while a denser K-point grid of $8\times8\times1$ was used for the density of states (DOS) and projected density of states (PDOS) calculations[3].

A plane-wave energy cutoff of 50 Ry was applied. The convergence thresholds for forces and total energy were set to $2\ .10^{-3}$ Ry and 10^{-6} Ry, respectively. Additionally, the Murnaghan equation of state was used to determine the minimum energy value[4].

III-2- Test of convergence:

To ensure the accuracy of the calculations, a convergence test is required for different parameters. This involves calculating the total energy of the system while varying key parameters such as the cutoff energy (E_{cutoff}) and the number of K-points in the Monkhorst-Pack mesh. **Figure III.1** and **FigureIII.2** present the total energy (in Ry) as a function of the number of K-points and the selected cutoff energy within the first Brillouin zone.

From the two graphs, we can conclude that the optimal number of K-points is $8\times8\times1$ for the primitive cell, which corresponds to $2\times2\times1$ for the $4\times4\times1$ supercell. Regarding the cutoff energy, a minimum estimate of 30 Ry can be chosen.

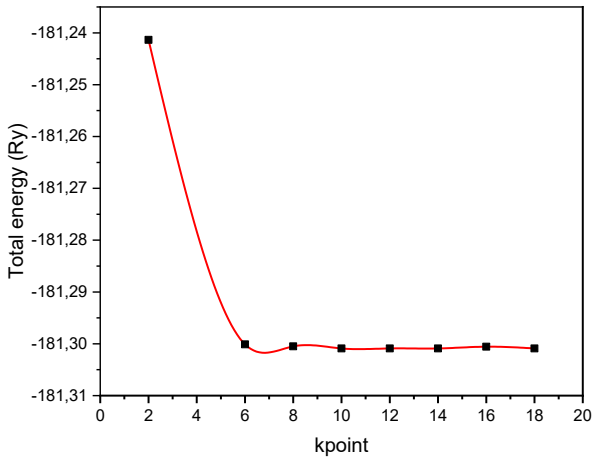


Figure III.1: Convergence test of the total energy as a function of the number of k-points in the first Brillouin zone.

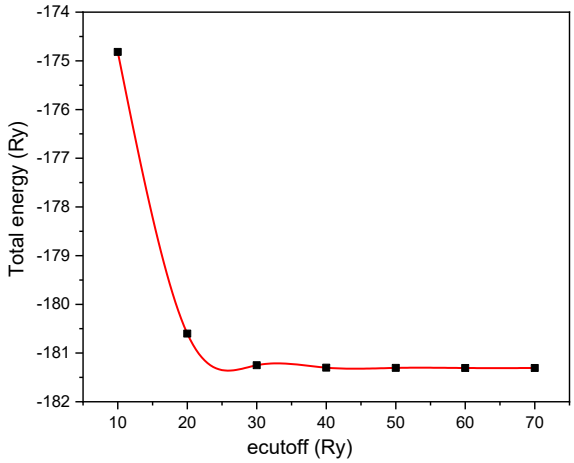


Figure III.2 : Convergence test of the total energy as a function of ecutoff energy.

III-3- Structural Properties :

The calculation of structural properties is crucial for determining other physical properties of a material. This calculation aims to find the equilibrium cell size corresponding to the minimum energy E_0, using the Murnaghan equation, given by the following relation[4]:

$$E(V) = E_0 + \frac{B}{B'(B'+1)}\left[V\left(\frac{V_0}{V}\right)^{B'} - V_0\right] + \frac{B}{B'}(V - V_0) \qquad \text{(III-1)}$$

Here, E(V) represents the total energy at volumeV, while $E_0$and V_0 correspond to the energy and volume at equilibrium, respectively. B_0 and B_0' denote the bulk modulus (compressibility coefficient) and its first derivative, respectively, which are given by the following two relationships[3]:

$$B = V\frac{\partial^2 E}{\partial V^2} \qquad \text{(III-2)}$$

And

$$B' = \frac{\partial B}{\partial P} \qquad \text{(III-3)}$$

$MoSe_2$ crystallizes in a hexagonal structure, where the 2H-$MoSe_2$ phase belongs to the space group P63/mmc (No. 194). **Figure III.3** presents the structure of a $MoSe_2$ monolayer: (a) a top view of the supercell, (b) a side view of the supercell, and (c) the primitive structure. The monolayer 2H-$MoSe_2$ structure was first optimized to determine its equilibrium lattice parameters, including the lattice constants a and c, the Se–Mo bond length, and the nearest Se–Se distance. These results are summarized in **Table III.1.**

Additionally, **Figure III.4** illustrates the variation of total energy as a function of the volume of the primitive $MoSe_2$ structure.

We note that the obtained structural parameters, lattice constants a=3,32A° and c=13,46A°, monolayer thickness (d_{Mo-Mo}=3,38 A°), and bond length (d_{Mo-Se}=2,67 A°) are in good agreement with previously reported theoretical and experimental values[5-12]. The relative error remains small, indicating the reliability of our calculations.

The bulk modulus $B_0$and its first derivativeB_0'of the bulk *2H-MoSe₂* structure were found to be 111.8 GPa and 3.84, respectively. Notably, the value of B_0'falls within the typical range of 3 to 5, consistent with other solid material.

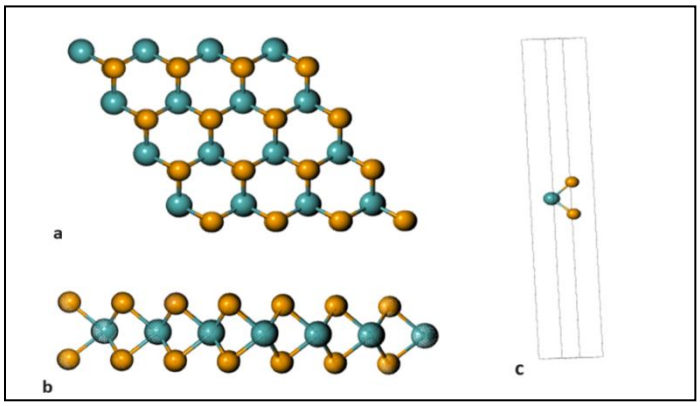


Figure III. 3: the structure of MoSe2 monolayer where (a) top view of the supercelle, (b) side view of the supercell and (c) is the premative structure, the atom of Selenuimare shown with yellow and of the molebdenum with green.

Table III.1: Structural parameters of 2H-MoSe2, including the lattice constants a (A°) and c (A°), the monolayer thickness d_{Mo-Mo}(A°), and the bond length d_{Mo-Se}(A°).

	Our calculation	Auther calculation	Exp	Relative error(%)
a(A°)	3.32	3.36[8], 3,29[10], 3.327[9], 3.25, 3.33[12]	3.29[7], 3.288[5]	1.01
c (A°)	13.46	12.98[8], 12,93[10], 13.175[9]	12.93[6], 12,92[5]	1.03
d_{Mo-Mo} (A°)	3.34	3.38[8], 3.35, 3,32[12]	-	-
d_{Mo-Se} (A°)	2.67	2.58[8], 2.55[9], 2.541[10], 2.535[11], 2.51[12]	2,49[5]	-

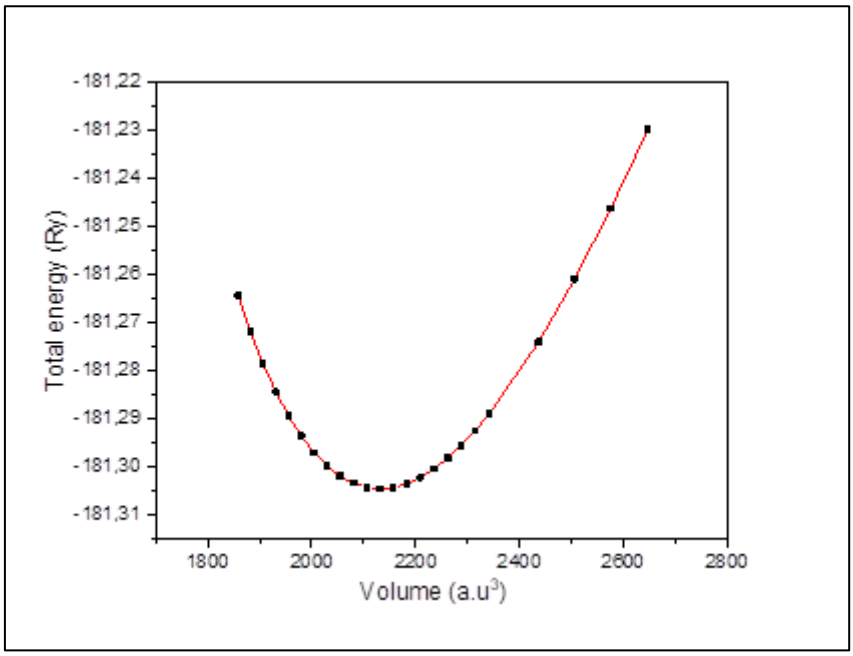


Figure III.4: Variation of total energy as a function of volume for the primitive monolayer $MoSe_2$.

- **Structure of $MoSe_2$ Monolayer with Defect :**

From the primitive structure, we constructed a supercell and introduced three types of defects: (i) the doped As(Mo) structure, where a molybdenum (Mo) atom is substituted with an arsenic (As) atom; (ii) aMo vacancy structure,where a molybdenum atom is removed; and (iii) an interstitial Asstructure,where(As) atom positioned at the centre of the hexagonal cell. These structures are illustrated in **Figure III.5**.

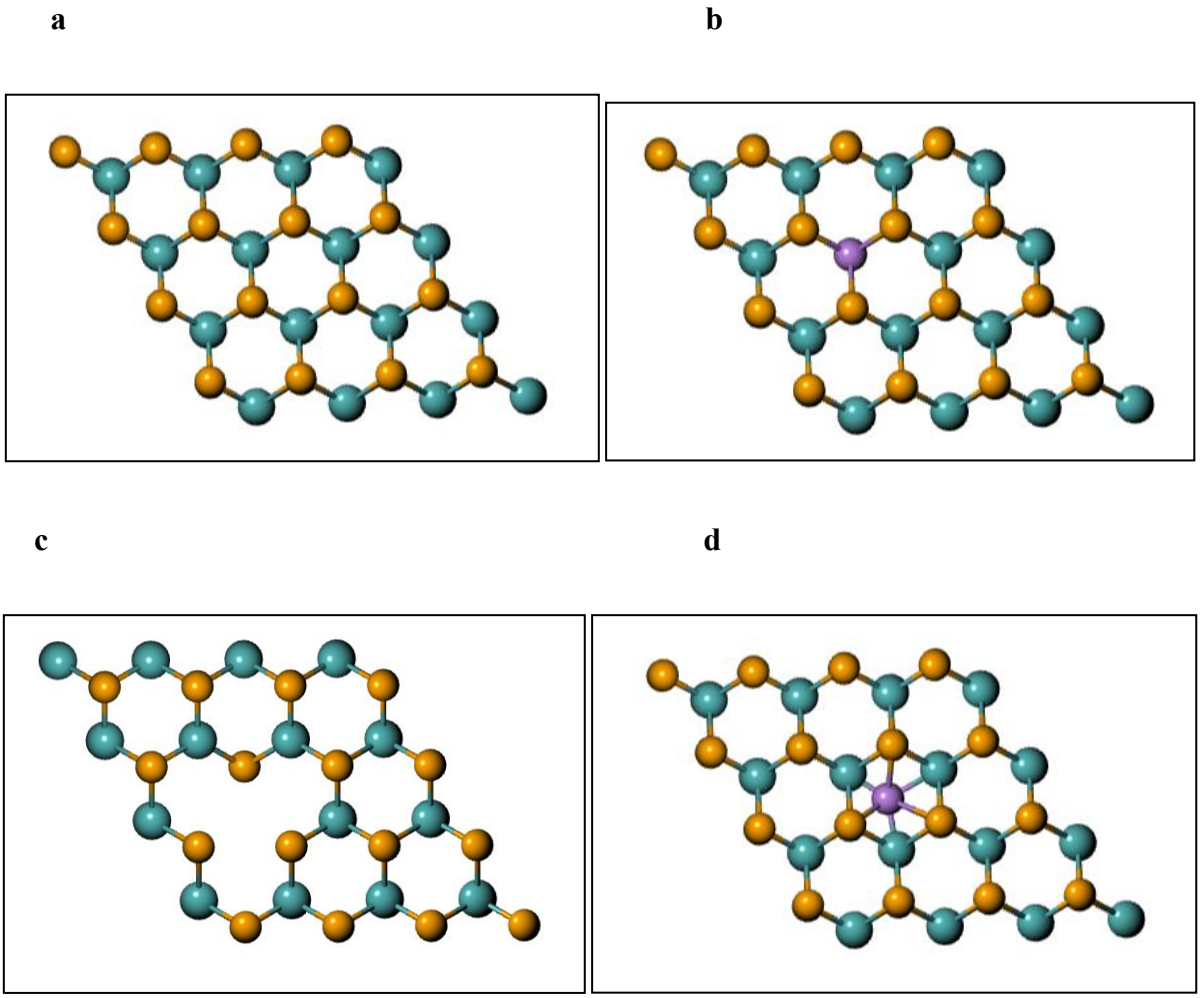


Figure III.5:Structure of the $MoSe_2$ monolayer supercell: (a) pristine structure, (b) As(Mo)-doped structure, (c) Mo vacancy, and (d) interstitial As.

III-4-Formation Energy of Structures with Defects:

The formation energies for the defferent defects of monolayer $MoSe_2$ were calculated asdone in [8]:

$$E_f = E_{def} - E_{pure} - \sum_i n_i \mu_i \qquad \text{(III-4)}$$

Where E_{def}represents the total energy of the supercell containing a single defect, E_{pure} is the total energy of the pristine $MoSe_2$ supercell of the same size, μ_i is the chemical potential of species i, and $n_i$denotes the number of atoms added $(n_i>0)$ or removed $(n_i<0)$ from the system[8,13, 14].

For the calculation of chemical potentials, we consider the bulk (bcc) phase for Mo and Se, and the rhombohedral phase for *As*. The values of the chemical potentials are primarily governed by experimental growth conditions. Due to the absence of experimental values. These were used as references in the defect formation energy calculations. To determine the

possible states, we consider Se-rich conditions, where μ_{Mo} and μ_{Se} are related through the following thermodynamic equation:

$$\mu_{MoSe2} = \mu_{Mo} + 2\mu_{Se} \quad \text{(III-5)}$$

Where μ_{MoSe2} represents the energy required to form $MoSe_2$ from its elemental constituents in their most stable phases. This approach is consistent with previous DFT studies that consider phase stability and defect energetics in transition metal dichalcogenides, e.g., Komsa and Krasheninnikov[15] ;S. Halder et al[13].

The values of the chemical potentials are presented in **Table III-2**, while the formation energies of the different studied structures under Se-rich conditions are provided in **Table III-3**.

Table III- 2: Chemical potentials of Mo, Se and As atoms expressed in (Ry).

	Chemical potential (Ry)
μ_{Mo}	−139.746
μ_{Se}	−20.777
μ_{As}	−20.456

Table III- 3: Formation energies of different structures under Se-rich conditions in (eV).

Structure	**Formation energy (eV)**	**Auther calculation (eV)**
As(Mo) doped	1,839	2,01 for Sb atom[8]
Mo vacancy	2,670	3,6[13], 2,42[8], 3,2 in MoS_2[16]
As interstitial	17,422	-

It can be observed that As(Mo) doped structure is a favourable configuration due to its low formation energy of 1.839 eV. The Mo vacancy system is also a stable configuration, as studied in [17].

In contrast, the formation energy of the As interstitial defect is as high as 17.422 eV, suggesting that while the formation of this defect is possible, it is likely to be a metastable state.

III-5- Electronic Properties:

It is essential to describe the electronic structure, as studying the electronic properties enables the determination of key characteristics such as the energy gap, band structure, density of states (DOS), and partial density of states (PDOS).

The electronic structure of a material is influenced by its atomic composition, bonding, crystal symmetry, defects, and external conditions.

III-5-1-Band Structures

The band structure allows us to determine the nature of all possible electronic states by representing the electron energy as a function of the wave vectork in the reciprocal lattice. The analysis is typically simplified by focusing on high-symmetry points within the first Brillouin zone. This concept is fundamental in solid-state physics and is crucial for understanding the electrical, optical, and thermal properties of materials.

- **From Bulk to Monolayer Band Structure**

The **Figure III.6** presents the band structure of the bulk primitive cell and monolayer of $MoSe_2$, where the bandstructure is calculated along high-symmetry points $\Gamma - M - K - \Gamma$ in the Brillouin zone [18], As shown in **Figure III.6(a),** the valence band maximum is located at a high-symmetry point, while the conduction band minimum lies between the K point and Γ point, indicating an indirect band gap semiconductor.

In contrast, for the monolayer structure, **Figure III.6(b)** shows that both the valence band maximum and conduction band minimum are at the K point, revealing a direct band gap semiconductor. The values of the energy gap are presented in the **Table III-4.**

Table III-4: Energy gap values of bulk $MoSe_2$ and its monolayer.

	Our calculations	Auther calculations	Exprimental calculations
Bulk $MoSe_2$	1.47	1.43[19], 1.36[20]	1.56[21], 1.25[21], 1.42[22]
Monolayer $MoSe_2$	1.39	1.36[19], 1.41[8], 1.34, 1.40[23]	1.5[21], 1.58[23], 1.56[24]

From the**Table III-4**we can see that the band gap decreases with the increase of layers number, Our results are very consistent with the results obtained by theoretical[8, 19,20,23]and experimental measurements[21-24], which were determined using modulated photoreflectance spectroscopy and experimental other methods.

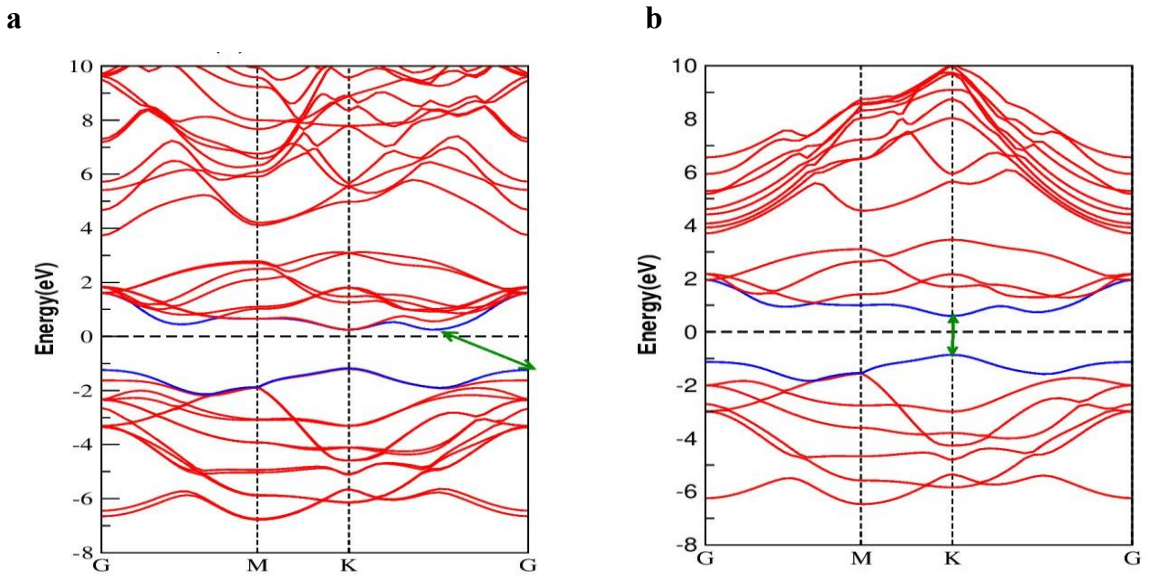


Figure III.6: band structure of the primitive structure of MoSe2 where : (a) for bulk structure and (b) for a monolayer structure.

- **Band Structure of $MoSe_2$ Monolayer with Defect**

Figure III.7 presents the band structure of (a) the pristine $MoSe_2$ monolayer, (b) the As(Mo)-doped system, (c) the Mo vacancy system, and (d) the As interstitial system, respectively. It is evident that all structures exhibit semiconducting behavior with a direct band gap, where the valence band maximum (VBM) and conduction band minimum (CBM) are both located at the *K* point of the high-symmetry Brillouin zone. Impurity levels, illustrated in red, appear due to the presence of defects. In the As(Mo)-doped system, four impurity levels emerge within the band gap, including two nearly degenerate levels, where three bands are located near the valence band maximum (VBM). For the system with a Mo vacancy, an increase in the band gap is observed along with the appearance of two distinct localized defect levels in the middle of the gap. Notably, one of these levels is positioned very close to the Fermi level, while the other aligns precisely with it. In the case of the As interstitial structure, two impurity levels emerge, accompanied by a shift of the Fermi level toward the conduction band minimum.

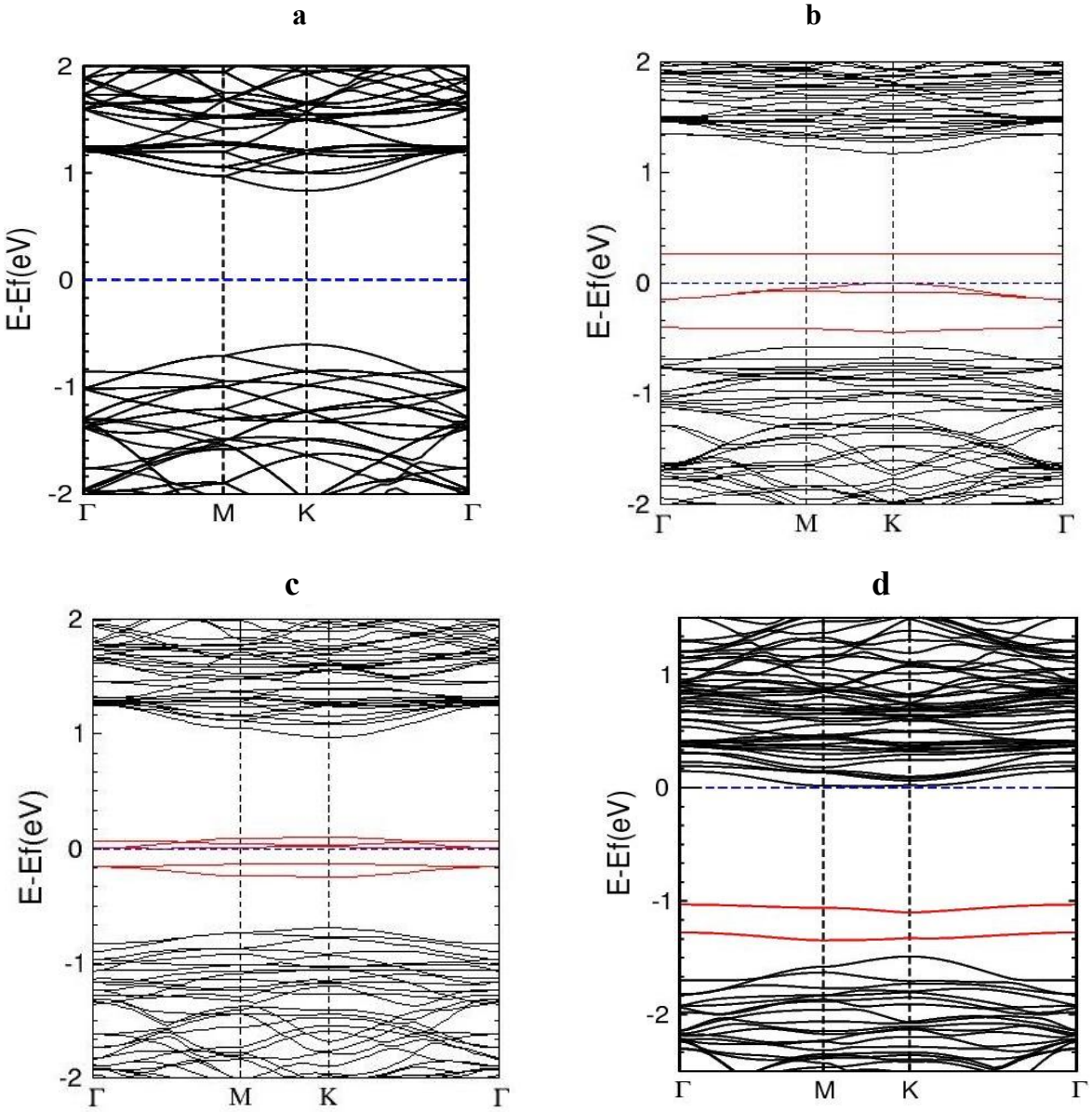


Figure III.7 :Band structure of (a) pure MoSe2 monolayer, (b) As(Mo)-doped structure, (c) Mo vacancy structure, and (d) As interstitial structure.

The values of the energy gap for all studied structures are presented in **Table III-5**. It is observed that the energy gap increases for impurity systems compared to the pristine $MoSe_2$ monolayer. This increase suggests a decrease in electrical conductivity[25]. Our results for the pristine system and the Mo vacancy system are in good agreement with previous theoretical and experimental studies.

Table III-5 : band gap of different structures in (eV).

	Energy gap (eV)		
Structure	**Our calculation**	**Other calculation**[26]	**Expremental calculation**[27]
Pure $MoSe_2$	1.41	1.57, 1.44	1.56
As(Mo) doped	1.73	-	-
Mo Vacancy	1.66	1.8	-
As Interstitial	1.51	-	-

III-5-2- Density of State and Partial Density of States (DOS and PDOS)

The density of states (DOS) represents the number of electronic states available for occupation at specific energy levels. Analyzing the total and partial density of states (PDOS) allows us to determine the origin of the states forming the valence and conduction bands. Additionally, it provides insights into the nature of bonding between atoms in the studied materials and helps evaluate the effects of impurities, defects, or dopants on the electronic structure[28].

In this study, we analyze the density of states (DOS) and partial density of states (PDOS) for the various structures investigated, as presented in**Figure III.8, Figure III.9, Figure III.10**, and**Figure III.11**.

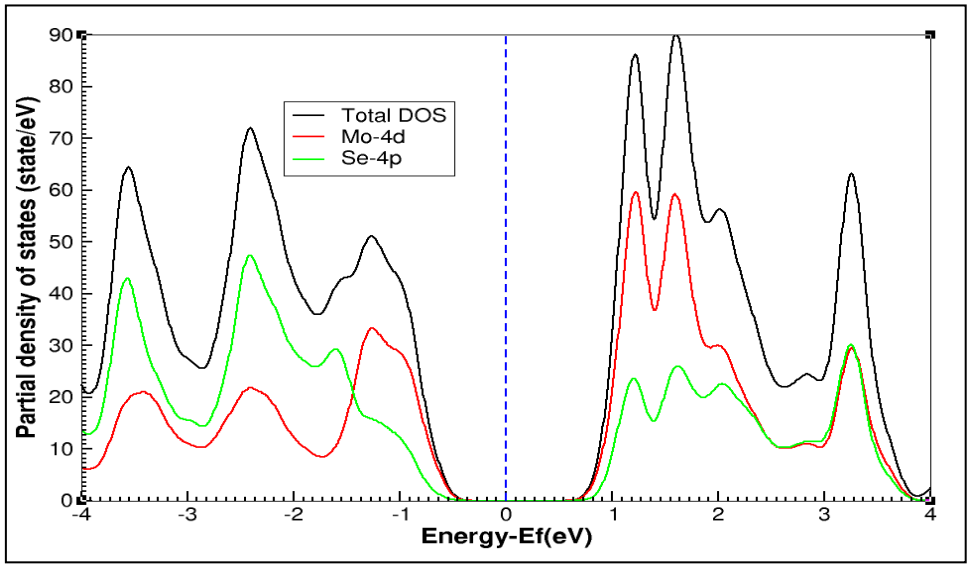


Figure III.8: Density of states (DOS) and partial density of states (PDOS) of the pristine $MoSe_2$ monolayer structure.

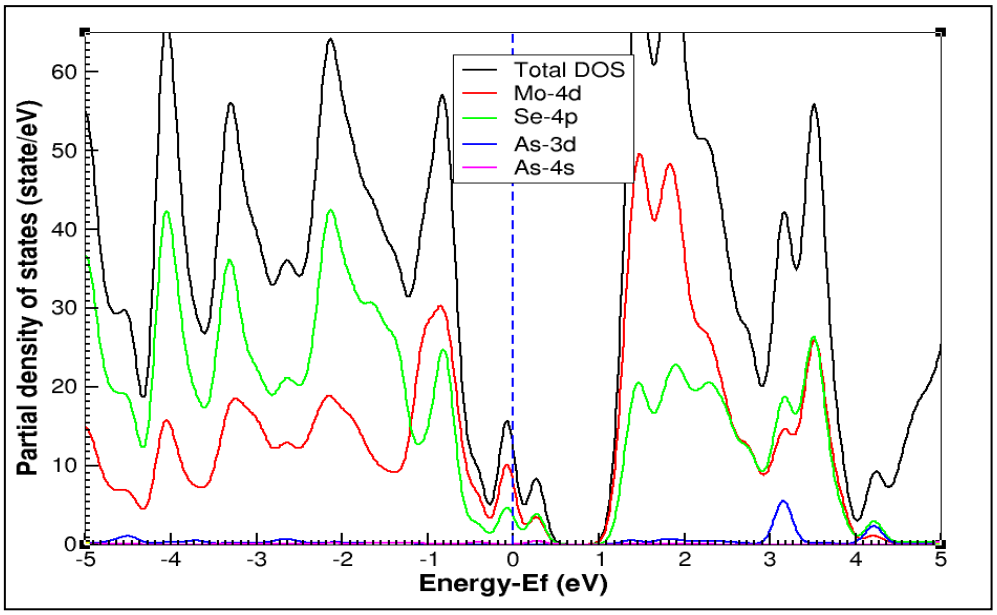


Figure III.9: Density of states (DOS) and partial density of states (PDOS) of the As(Mo) doped structure.

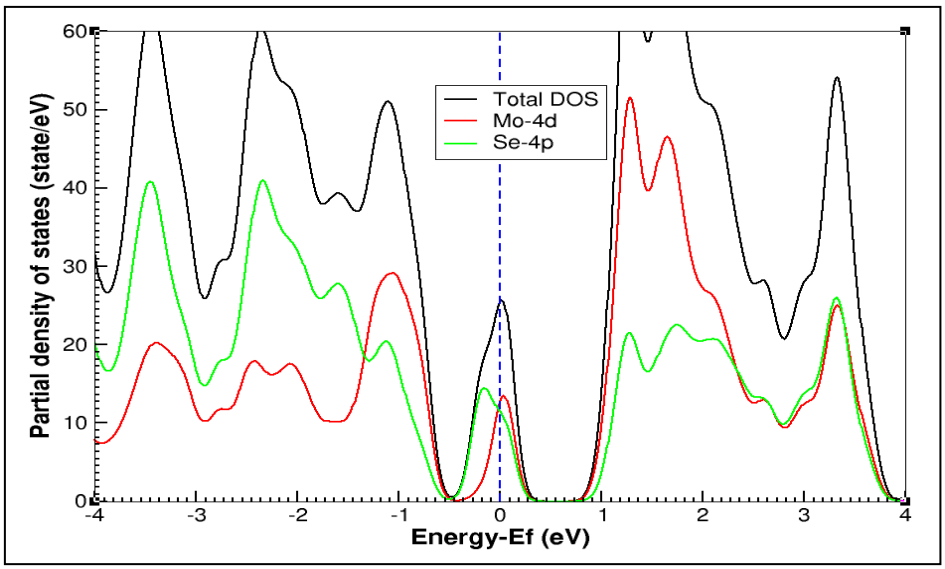


Figure III.10: Density of states (DOS) and partial density of states (PDOS) of the Mo vacancy structure.

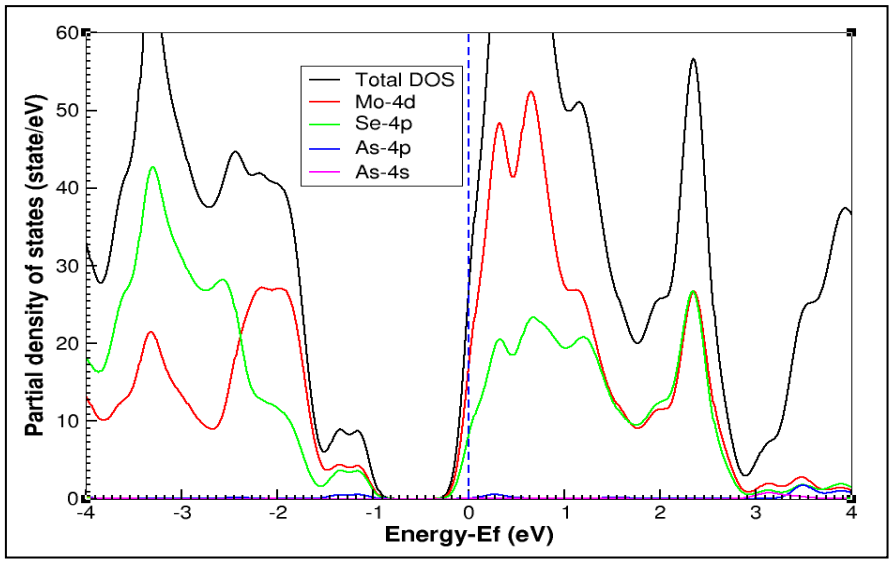


Figure III.11: Density of states (DOS) and partial density of states (PDOS) of the As interstitial structure.

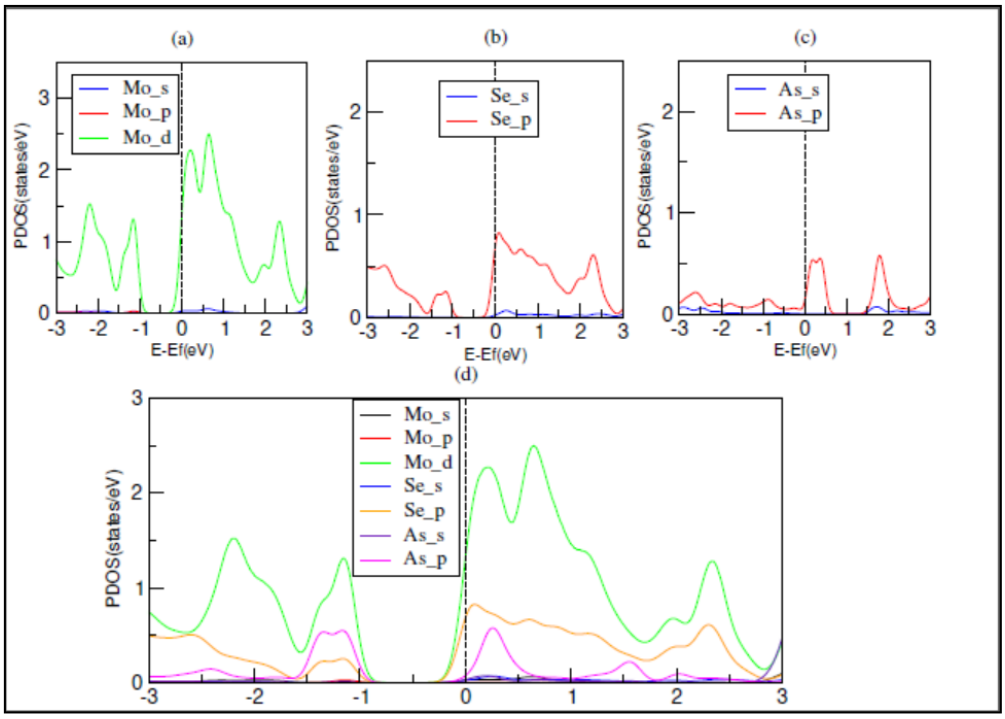


Figure III.12: Partial density of states (PDOS) in the As(Mo) doped system for: (a) Mo atom near the As position, (b) Se atom near the As position, (c) substitutional As atom, and (d) comparison of all previous cases.

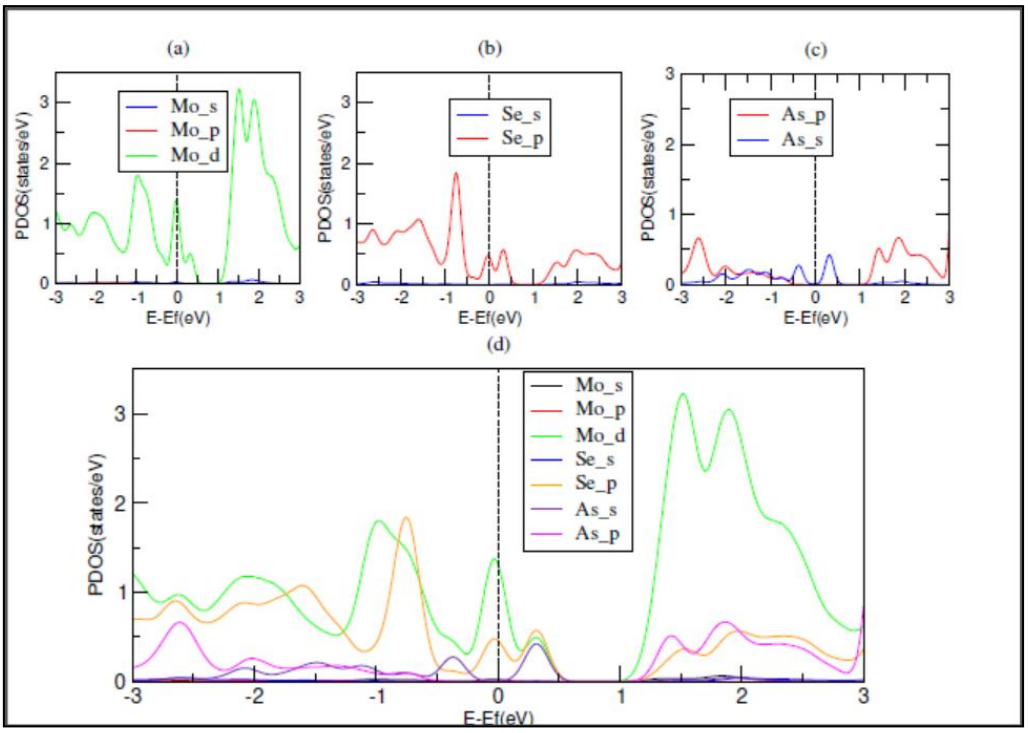


Figure III.13:Partial density of states (PDOS) in the As interstitial system for: (a) Mo atoms near the interstitial As, (b) Se atoms near the interstitial As, (c) interstitial As atom, and (d) comparison of all previous cases.

From **Figure III.8**, we observe that for the pure $MoSe_2$ structure, the position of the Fermi level suggests that this material behaves as an n-type semiconductor. Since our focus is on the DOS near the band gap, we have presented it within the range of -2 eV to +2 eV. The DOS at the top of the valence band and the bottom of the conduction band are primarily composed of Mo 4d and Se 4p orbitals. These results are in good agreement with previous studies[18,26,29, 30].

The As(Mo) doped system exhibits three defect levels within the band gap. The first and highest level is located at 0 eV (the Fermi level), while the second, slightly lower in energy, appears at +0.35 eV. Additionally, a shoulder is observed at the tail of the valence band, around -0.35 eV, as clearly shown in **Figure III.9**.

However, this Figure does not provide sufficient insight into the origin of these defect levels, as the PDOS includes contributions from all Mo and Se atoms (15 and 32 atoms, respectively), while the contribution of the single As atom remains indistinguishable,For this reason, we have plotted the PDOS per atom for Mo and Se atoms located near the As atom, as well as the PDOS for the As atom itself, as shown in **Figure III.12.**

This analysis allows us to attribute the defect level at 0 eV to Mo 4d and Se 4p orbitals, similar to the vacancy defect. Meanwhile, the defect level at +0.35 eV can be attributed to

contributions from Se 4p, Mo 4d, and As 4s orbitals, whereas the shoulder at -0.35 eV originates from As 4s and Se 4p orbitals. This indicates that introducing an As atom at a substitutional Mo site results in an increase in the band gap.

The atomic volume of arsenic (As) is smaller than that of molybdenum (Mo) and selenium (Se), which explains why the density of states (DOS) of the As(Mo)-doped system reflects a combination of both the As dopant and the Mo vacancy effects. A similar observation has been reported for the Sb(Mo)-doped system in MoS_2[8, 31], The shift of the Fermi level toward the valence band indicates that the doped material exhibits p-type semiconductor behavior. Additionally, the widening of the band gap and the introduction of new defect levels enhance optical absorption in the visible light spectral region. This modification in the electronic structure broadens the potential applications of the As(Mo)-doped system, particularly in photocatalysis and photovoltaic devices[17, 32].

From **Figure III.10**, two distinct impurity levels are observed. The first impurity level, located at 0.05 eV, can be attributed to the non-contributing Mo 4d orbital in bonding (vacancy), while the second level, appearing at -0.3 eV, is associated with the non-contributing Se 4p orbital in bonding. The positioning of the Fermi level in the system with a Mo vacancy suggests that the material exhibits p-type semiconductor behavior. These findings are in good agreement with previous studies[26, 33], further validating the electronic structure modifications induced by the vacancy defect.

Figure III.11 presents the DOS and PDOS of a monolayer $MoSe_2$ containing an interstitial As atom. The presence of this interstitial defect introduces two distinct impurity levels within the band gap, located at -1.04 eV and -1.29 eV. To elucidate the origin of these defect levels, it is essential to analyze the DOS and PDOS of the interstitial As atom, as well as the DOS and PDOS of the surrounding Mo and Se atoms, as depicted in **Figure III.13**. The analysis reveals that these defect levels primarily originate from the contributions of Mo 4d, Se 4p, and As 4p orbitals. Additionally, a notable distribution of the Mo 4d orbital is observed for the defect level at -1.04 eV. The upward shift of the Fermi level into the conduction band suggests that the $MoSe_2$ monolayer exhibits n-type doping due to the presence of the interstitial As atom. This finding highlights the potential applicability of this material in optoelectronic and electronic deviceslike certain cameras or sensors operating in the infrared spectrum, due to its narrow band gap. As well as in photocatalysis within the visible light range and solar energy applications that rely on visible light to trigger chemical reactions[33,34].

III-5-3- Difference Charge Density

The electron density representation aims to express two basic ideas:

The electron charge density at a given point, representing the number of electrons per unit volume, is determined using the following equation:

$$\rho(r,\theta,\phi) = -e\sum_{i=1}^{N} n_i \left|\Psi_i(r,\theta,\phi)\right|^2 \qquad \text{(III-6)}$$

where :n_i represents the occupation number of the *i-th* electronic state.

$\Psi_i(r,\theta,\phi)$ is the wavefunction of the*i-th* electronic state.

a- "Electronic Distribution Density" or "Probability Density" ρ(r) which is the base of the functional density theory and is calculated by equation :

$$\rho(r,\theta,\phi) = \Psi(r,\theta,\phi)x\Psi^*(r,\theta,\phi) = \left|\Psi(r,\theta,\phi)\right|^2 \qquad \text{(III-7)}$$

On the other hand, the charge density difference provides a quantitative representation of charge transfer, which is a crucial factor in understanding adsorption phenomena. This analysis allows us to examine how charge redistributes around defect sites and to assess potential modifications in the bonding nature induced by doping. By evaluating the charge density difference, we can gain insights into the electronic interactions between the dopant and the host material, shedding light on changes in local charge distribution and their impact on the overall electronic structure. The charge density difference is mathematically expressed as follows [35]:

$$\Delta\rho = \rho_d - \rho_p - \rho_x \qquad \text{(III-8)}$$

Where the ρ_d , ρ_p and ρ_x are the total charge on doped system , pure $MoSe_2$ and doping atom, respectively[36, 37].

All charge densities are computed using the same computational setup**,** including grid spacing, exchange-correlation functional, and unit cell size, to ensure numerical consistency. The resulting $\Delta\rho$ can be visualized using isosurface plots or 2D slices, where yellow regions typically represent electron accumulation and blue regions denote electron depletion. These visualizations provide direct evidence of how electronic charge is redistributed upon doping, offering atomic-scale insight into the electronic and chemical behavior of the modified material.

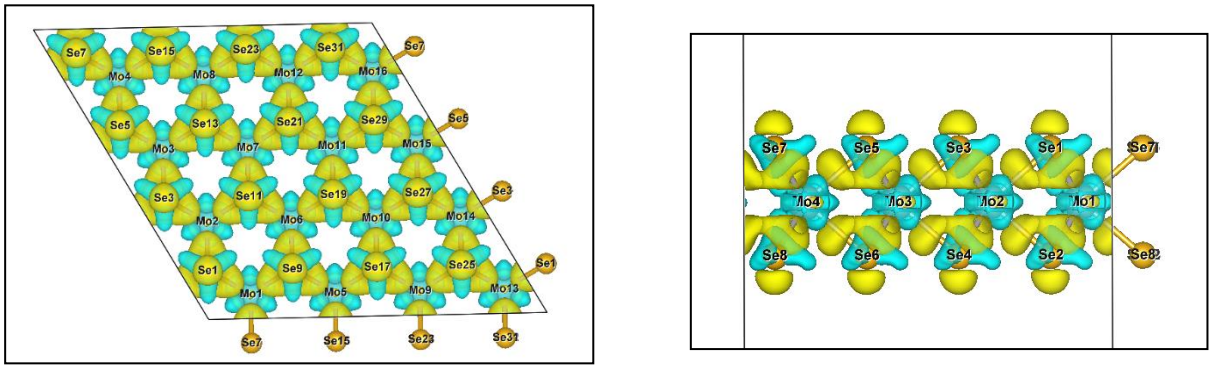


Figure III.14 :The distribution of electronic charge density isosurfaces of pure $MoSe_2$, where the blue regions represent electron depletion (loss of electrons), and the yellow regions indicate electron accumulation.

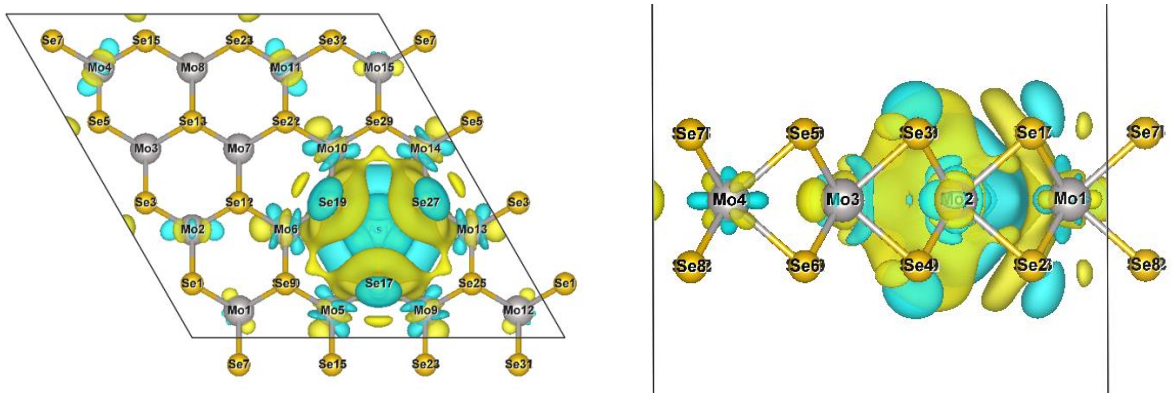
From **Figure III.14**, we observe electron accumulation between adjacent Se and Mo atoms, indicating the formation of a covalent bond. This behaviour arises due to the minimal difference in electronegativity between the two elements.

The **Figure III.15** presents top and side views of the charge density difference maps for three different structures: (a) the As(Mo)-doped system, (b) the Mo vacancy structure, and (c) the Asinterstitial structure. For the As(Mo) doped system, the charge density difference map reveals significant charge accumulation around the As atom, indicating the formation of mid-gap states. Additionally, the observed electronic accumulation between the defect site and the surrounding Se atoms suggests that the bonding remains predominantly covalent, despite the substitution of Mo by As, This behavior was confirmed by Zhao et al., who investigated the substitution of selenium atoms with arsenic in monolayer $MoSe_2$[17].

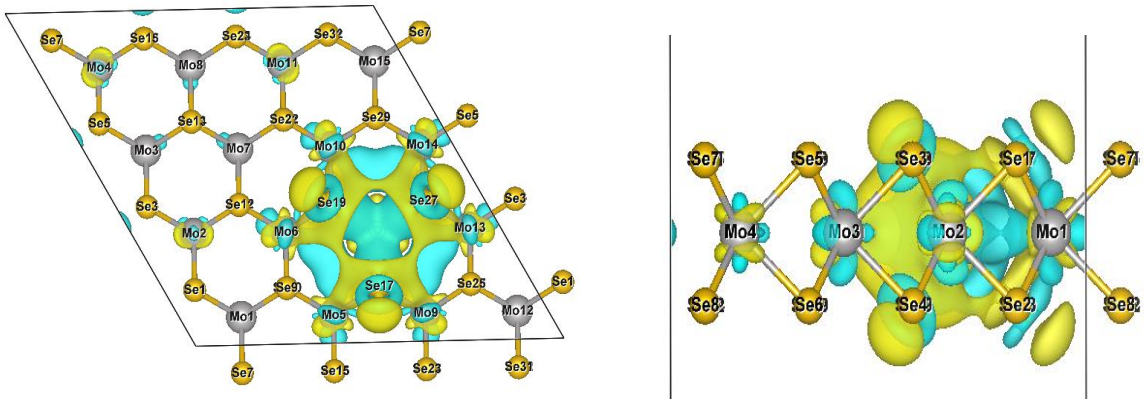
The concentration of electron density around the two atoms forming the bond implies a weakening of these bonds compared to the pristine $MoSe_2$structure[38, 39]. This bond weakening can be attributed to the relatively small electronegativity difference between As and Se, which reduces bond strength[40].

Furthermore, the presence of blue regions near the As atom site signifies charge depletion from the neighboring Mo and Se atoms, confirming a charge transfer process from the host lattice to the dopant (As)[41].

(a)



(b)



(c)

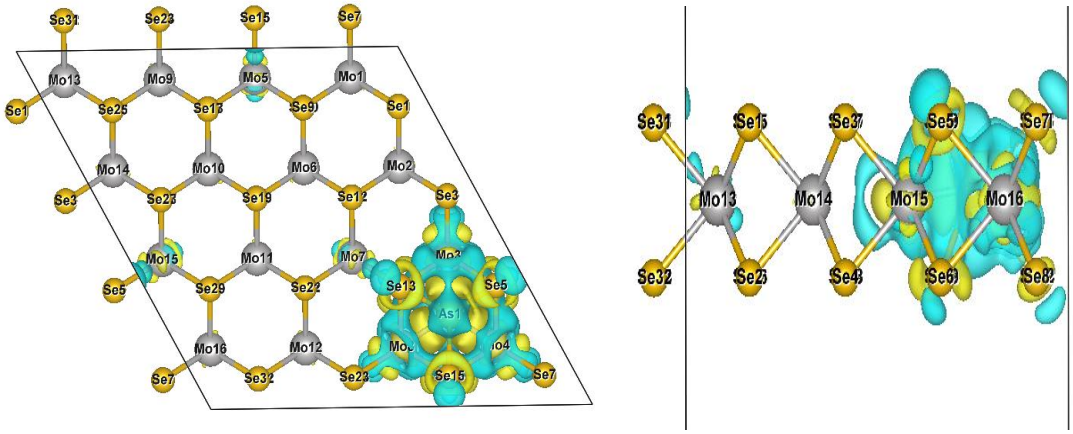


Figure III-15:Electronic charge density difference of (a) the As(Mo)-doped system, (b) the Mo vacancy system, and (c) the interstitial As system. The blue regions represent electron depletion, while the yellow regions indicate electron accumulation.

In the Mo vacancy system, the charge redistribution pattern indicates a significant perturbation in the electronic environment caused by the absence of a Mo atom. Notably, a resemblance in charge density distribution is observed between As(Mo) doped and Mo

vacancy states. This similarity arises from the fact that, in the Mo vacancy structure, a free electron that does not participate in bonding accumulates in the region where the Mo atom is missing. Such charge accumulation leads to comparable electronic characteristics between the doped and vacancy systems, highlighting the role of localized electronic states in shaping their properties. Moreover, the presence of these localized states can induce mid-gap states, which may significantly affect the material's electronic and optical behavior.

For the As interstitial structure, a notable accumulation of electrons is observed around the As atom, extending toward the neighboring Se atoms. This charge distribution indicates the formation of strong valence bonds between As and Se[42], which can be attributed to their close atomic proximity and significant charge transfer from the pristine $MoSe_2$ lattice to the interstitial As atom. The charge redistribution suggests that the presence of the interstitial As atom induces a substantial perturbation in the local electronic structure,altering the bonding characteristics within the $MoSe_2$ framework and introduces strong charge localization in the vicinity of As atom.

This structural and electronic modification contributes to the high formation energy of this configuration, as the system requires considerable energy to accommodate the interstitial As atom within the host lattice.

Generally, the modification of the electronic properties of the $MoSe_2$ structure in the presence of defects can be attributed to the localized redistribution of electronic charge. This charge rearrangement alters the bonding characteristics, induces changes in the electronic density of states, and may introduce mid-gap states, ultimately influencing the overall electronic behavior of the material.

III-6- Optical Properties

The optical properties of a material are determined by its interaction with electromagnetic waves, with the dielectric function describing the amount of light absorbed by the material. The complex dielectric function is given by[43]:

$$\varepsilon(\omega) = \varepsilon_r(\omega) + i\varepsilon_i(\omega) \quad \text{(III-9)}$$

where $\varepsilon_r(\omega)$ and $\varepsilon_i(\omega)$, ω are respectively, the real and imaginary parts of the complex dielectric function and the frequency, the two coefficients are related to the refractive index *n*, and extinction coefficient ***k*** which is given by the following relationships[44]:

$$\varepsilon_r = n^2 - k^2 \quad \text{(III-10)}$$

$$\varepsilon_i = 2nk \quad \text{(III-11)}$$

Thus, these two relationships can be deduced[45] :

:

$$n(\omega) = \sqrt{\frac{1}{2}(\varepsilon_r(\omega) + \sqrt{\varepsilon_r{}^2(\omega) + \varepsilon_i{}^2(\omega)})} \quad \text{(III-12)}$$

$$k(\omega) = \sqrt{\frac{1}{2}(\sqrt{\varepsilon_r{}^2(\omega) + \varepsilon_i{}^2(\omega)} - \varepsilon_r(\omega))} \quad \text{(III-13)}$$

The real part of the dielectric function describes the polarization response of a material to an external electric field, while the imaginary part represents the absorption of electromagnetic waves due to electronic transitions. Using the Kramers-Kronig transformation[46] the dielectric function allows for the calculation of various optical properties, including the refractive index $n(\omega)$, extinction coefficient $k(\omega)$, reflectivity $k(\omega)$, absorption coefficient $\alpha(\omega)$, and optical conductivity $\sigma(\omega)$.

In addition, a complex quantity related to the dielectric function allows us to describe the system's response to a planar electromagnetic wave. This quantity is the complex refractive index, which is given by the following relation[47-49]:

$$N(\omega) = \sqrt{\varepsilon(\omega)} = n(\omega) + ik(\omega) \quad \text{(III-14)}$$

In the case of our hexagonal anisotropic structure, the optical properties were calculated along the three crystallographic directions: (xx), (yy), and (zz)[50].All the studied optical quantities were analyzed within the energy range of 0 eV to 17 eV for the $MoSe_2$ monolayer, the As(Mo)-doped structure, the Mo vacancy structure, and the As interstitial structure.

Figures III.14 (a, b, c, and d) present the real part $\varepsilon_r(\omega)$ of the dielectric function as a function of energy for the pure $MoSe_2$ monolayer, the As(Mo) doped structure, the Mo

vacancy structure, and the As interstitial structure, respectively. Notably, in both the As(Mo) doped and Mo vacancy structures, the dielectric function exhibits a shift toward higher energies compared to the pristine $MoSe_2$ monolayer, wich suggest the increase in bandgap.This result is consistent with the behavior observed in MoS_2 doped with Sb at the Mo site, where the static dielectric constant increases from 1.42 to 2[51].

The **Table III-5** presents the values of the real part of the static dielectric function, which plays a crucial role in determining the optical properties of a solid material. This parameter, also known as theelectrical permittivity, describes how the studied medium interacts with an external electric field. The static dielectric function provides insight into the material's ability to screen electrostatic fields and influences fundamental optical characteristics such as the refractive index. According to the Penn model, the static dielectric function can be expressed as follows[50]:

$$\varepsilon_r(0) = 1 + (\hbar\omega_p / E_g)^2 \quad \text{(III-15)}$$

Where ω_p represent the the plasma frequency and the $E_g$represent the energy gap

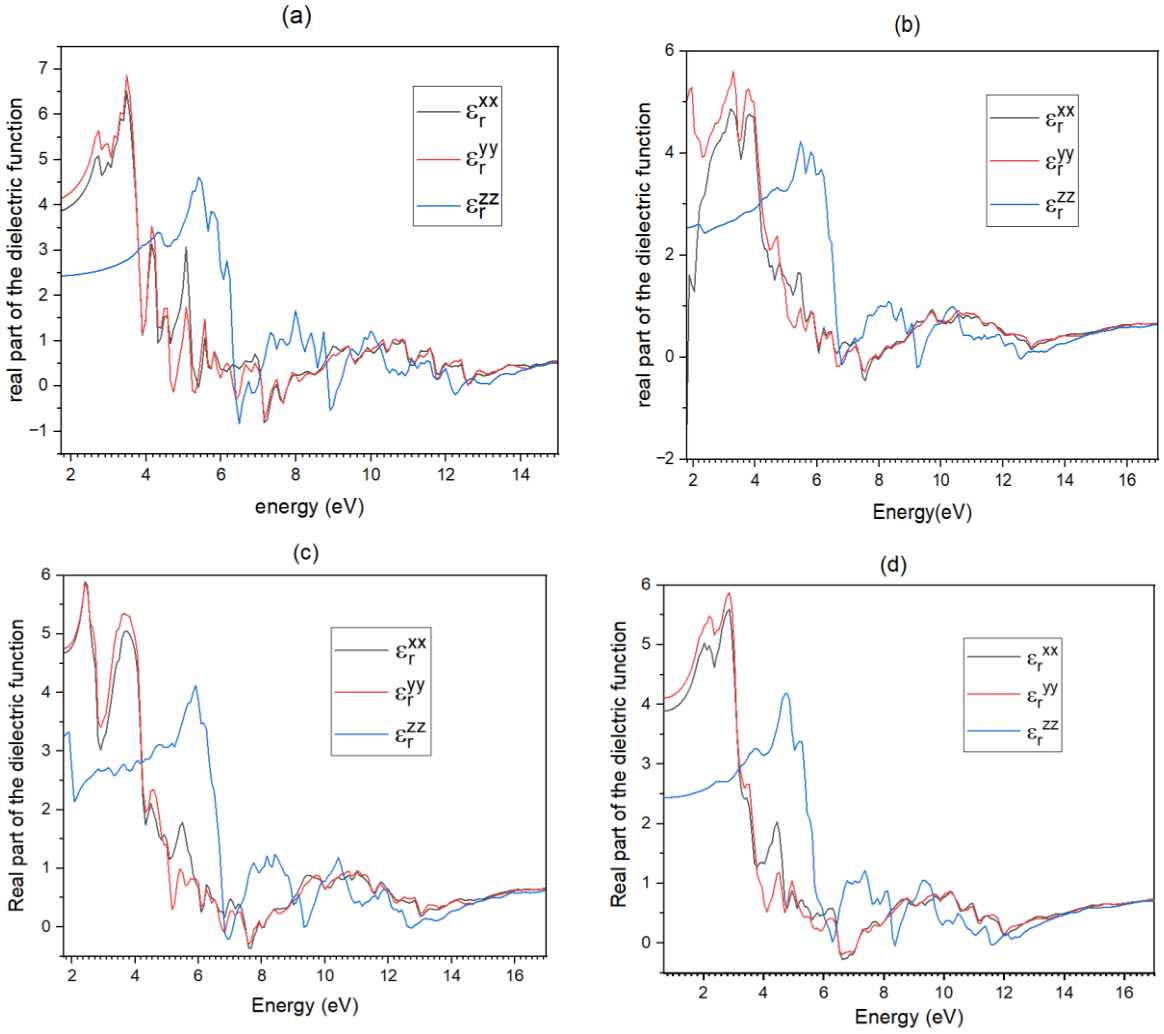


Figure III.16 : Real part of the dielectric function for (a) the pristine MoSe2 monolayer structure, (b) the As(Mo) doped structure, (c) the Mo vacancy structure, and (d) the As interstitial structure.

We observe that the $\varepsilon_r^{xx}(0)$ and $\varepsilon_r^{yy}(0)$ components are similar across all studied structures. Among them, the Mo vacancy system exhibits the highest dielectric constants $\varepsilon_r^{xx}(0)$ and $\varepsilon_r^{zz}(0)$ whereas the pure $MoSe_2$ monolayer has the lowest values $\varepsilon_r^{xx}(0)$, $\varepsilon_r^{yy}(0)$ and $\varepsilon_r^{zz}(0)$, This indicates that the pure $MoSe_2$ structure possesses the highest anisotropy, which contributes to its strong absorption properties and lowest direct band gap.

We also identified the maximum values of $\varepsilon_r(\omega)_{\max}$ and their corresponding energies in the (xx), (yy), and (zz) directions for all studied structures, as presented in **Table III-6**. The $\varepsilon_r^{xx}(\omega)_{\max}$ $\varepsilon_r^{yy}(\omega)_{\max}$ exhibits a noticeable shift toward lower energies in the doped and vacancy systems, which suggests a reduction in the optical bandgap and an increase in dielectric screening due to defect-induced states. In contrast, $\varepsilon_r^{zz}(\omega)_{\max}$ shifts toward higher

energies in most cases, except for the interstitial As system, where localized states may play a role in modifying the electronic structure. These variations directly influence the refractive index and optical absorption properties, impacting potential applications in optoelectronic devices.

Table III-5: Static Dielectric Constant in the (xx), (yy) and (zz) directions.

Structure	$\varepsilon_r^{xx}(0)$	$\varepsilon_r^{yy}(0)$	$\varepsilon_r^{zz}(0)$
Pure $MoSe_2$	3.8	4.06	2.42
doped As(Mo)	4.4	4.94	2.53
Mo vacancy	4.67	4.75	3.25
As interstitial	3.89	4.11	2.44

Table III-6 : Maximum values of and their corresponding energies in the (xx), (yy) and (zz) directions.

Structure	$\varepsilon_r^{xx}(\omega)_{max}$	$\varepsilon_r^{xx}(\omega)_{max}$ at energy (eV)	$\varepsilon_r^{yy}(\omega)_{max}$	$\varepsilon_r^{yy}(\omega)_{max}$ at energy (eV)	$\varepsilon_r^{zz}(\omega)_{max}$	$\varepsilon_r^{zz}(\omega)_{max}$ at energy (eV)
Pure $MoSe_2$	6.50	3.48	6.86	3.48	4.61	5.40
doped As(Mo)	4.86	3.21	5.25	3.79	4.22	5.46
Mo vacancy	5.89	2.40	5.85	2.4	4.12	5.91
As interstitial	5.60	2.87	2.86	2.87	4.19	4.79

The onset of optical absorption, which corresponds to the fundamental absorption threshold, occurs at 1.4 eV for the pristine $MoSe_2$ monolayer, which is in good agreement with the experimental value of 1.54 eV reported by Jorge Quereda et al[52], 1.4 by Y.Li[53] and 1.5 by kim Tae Jung et al[54]as well as withprevioustheoreticalcalculations[38, 55].

For the doped As(Mo) system, the threshold shifts to 1.74 eV, while it is found at 1.66 eV for the Mo vacancy system and 0.7 eV for the As interstitial system, where bui et al[55] found that this threshold shifts toward lower energies, reaching 1.1 eV, when an interstitial Cr atom is introduced. This threshold represents the optical transition from the highest occupied state in the valence band to the lowest unoccupied state in the conduction band.

Additionally, a strong correspondence is observed between the xx and yy components, indicating an optical isotropy in the in-plane directions, whereas the zz component exhibits distinct behavior due to the layered nature of the material, this observation was confirmed by the result of Mehdipour Hamid and Kratzer Peter[16]. The observed variations in absorption

onset can be attributed to defect-induced modifications in the electronic band structure, which have a major impact on the material's optical response.

On the other hand, we have determined the maximum values of $\varepsilon_i(\omega)_{\max}$ and the corresponding energy values, which represent the maximum absorption of the studied materials, as shown in **Table III-7**.

The energy values corresponding to $\varepsilon_i^{xx}(\omega)_{\max}$ and $\varepsilon_i^{yy}(\omega)_{\max}$ are almost identical in all studied cases and remain within the range of 3.1 eV to 4.16 eV. Meanwhile, the corresponding energy values for $\varepsilon_i^{zz}(\omega)_{\max}$ are limited to the range of 5.64 eV to 6.66 eV.

For the pristine $MoSe_2$ system, the results are very close to those reported by V. P. Vinturajet al[55] andY. Li[53].

Furthermore, the peak positions of $\varepsilon_i^{xx}(\omega)_{\max}$, $\varepsilon_i^{yy}(\omega)_{\max}$ and $\varepsilon_i^{zz}(\omega)_{\max}$ shift slightly towards higher energies for the As(Mo) doped and Mo vacancy systems compared to the pure $MoSe_2$ system.

This shift is also observed in the case of a Mo vacancy in MoS_2[16]. However, in the case of an interstitial As atom, the peak shifts slightly toward lower energies. Additionally, new absorption peaks appear in the visible region near the absorption threshold in all directions, though they are less pronounced than the main absorption peak. These secondary peaks occur at approximately 2.2 eV, 2.0 eV, and 2.74 eV for the As(Mo)-doped, Mo vacancy, and interstitial systems, respectively. The additional peaks induced by As substitution at the Mo site in $MoSe_2$ closely resembles that observed in Sb(Mo)-doped MoS_2[51], The results for the Mo vacancy are also in very good agreement with those reported by Hamid Mehdipour and Peter Kratzer[16].These results indicating the presence of additional absorption features.

These findings are based on the analysis of both the real and imaginary parts of the dielectric function.

Table III-7: Maximum values of and their corresponding energies in the (xx), (yy) and (zz) directions.

Structure	$\varepsilon_i^{xx}(\omega)_{max}$	$\varepsilon_i^{xx}(\omega)_{max}$ at energy (eV)	$\varepsilon_i^{yy}(\omega)_{max}$	$\varepsilon_i^{yy}(\omega)_{max}$ at energy (eV)	$\varepsilon_i^{zz}(\omega)_{max}$	$\varepsilon_i^{zz}(\omega)_{max}$ at energy (eV)
Pure $MoSe_2$	5,81	3,81	6, 34	3,73	5,43	6,31
doped As(Mo)	4,64	4,13	4,68	4,13	4,56	6,55
Mo vacancy	4,96	4,16	5,37	4,16	4,09	6,66
As interstitial	4,78	3,11	5,25	3,11	3,94	5,62

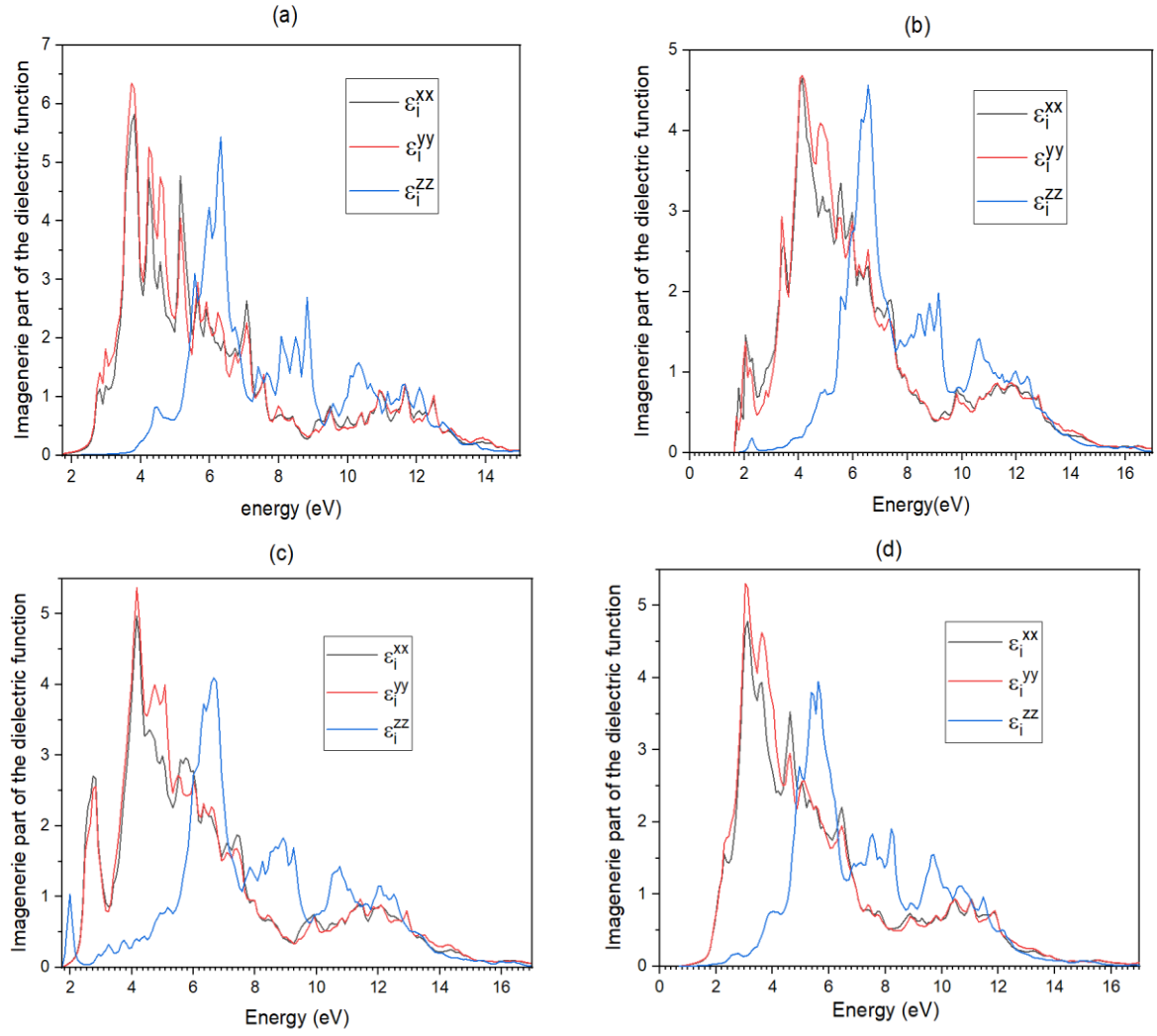


Figure III.17: Imaginary part of the dielectric function for (a) the pristine $MoSe_2$ monolayer structure, (b) the As(Mo)-doped structure, (c) the Mo vacancy structure, and (d) the interstitial As structure.

We studied the refractive index, which indicates the phase velocity of the electromagnetic wave[56],**Figure III.18** presents the variation of the refractive index components $n^{xx}(\omega)$, $n^{yy}(\omega)$ and $n^{zz}(\omega)$ as a function of photon energy.

First, we determined the static refractive index $n(0)$, where we found that it takes values of $n^{xx}(0)=1.95$, $n^{yy}(0)=2.01$ and $n^{zz}(0)=1.55$ for the pure $MoSe_2$ monolayer, this result is in agreement with the experimental study by Hsiang-Lin Liu, where they reported a refractive index $n(0)=1.9$ at a wavelength of 300 nm[57]as well as with the results of Hsu Chunwei et al[58]and with a previous theoretical study [26] , $n^{xx}(0)=2{,}1$, $n^{yy}(0)=2{,}22$ and $n^{zz}(0)=1{,}6$ for the As(Mo) doped structure, where we can see that in the case of Sb(Mo)-doped MoS_2, the refractive index also increases slightly[51], $n^{xx}(0)=2{,}16$, $n^{yy}(0)=2{,}18$ and $n^{zz}(0)=1{,}8$ for the Mo vacancy structure which is agreement with the result of Vinturaj, V P $n(0)=2{,}4$ [26], and $n^{xx}(0)=1{,}97$, $n^{yy}(0)=2{,}02$ and $n^{zz}(0)=1{,}56$ for the interstitial system. It is observed that the xx and yy components often have similar values, while the zzcomponent generally exhibits lower values. These values fall within the typical range of refractive indices for glasses, particularly optical glasses used in lenses, which range between 1.5 and 1.9**.** Additionally, it is noted that these results satisfy the following relationship:

$$n(0)=\sqrt{\varepsilon_r(0)} \quad \text{(III-16)}$$

which corresponds to the previous relationship **(III-12)**at low frequencies $(\omega=0)$ thisresult validates that structure studied acts as a typical dielectric medium in static conditions, making it suitable for optoelectronic applications[59].

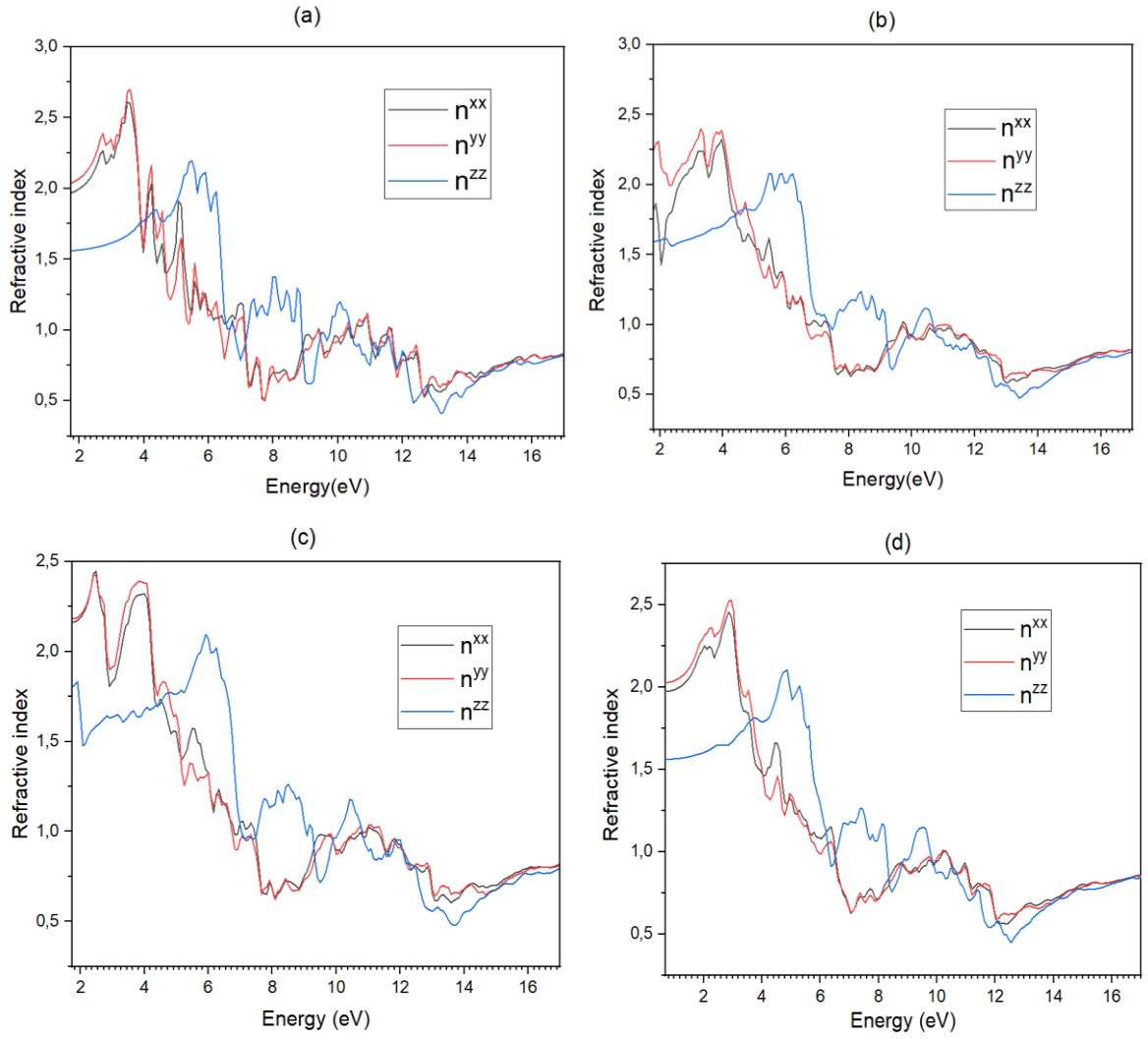


Figure III.18: Refractive index as a function of photon energy for (a) pure $MoSe_2$ monolayer structure, (b) As(Mo)-doped structure, (c) Mo vacancy structure, and (d) As interstitial structure.

The values of $n^{xx}(\omega)_{max}$, $n^{yy}(\omega)_{max}$ and $n^{zz}(\omega)_{max}$ and their corresponding energies for all studied systems are presented in **Table III-8**. We observe that both the refractive indices $n(\omega)_{max}$ and their corresponding energies generally decrease compared to the pristine $MoSe_2$ system, except for the doped As(Mo) structure, where the refractive $n^{yy}(\omega)_{max}$ and its corresponding energy increase, as well as the corresponding energy of $n^{xx}(\omega)_{max}$ in the vacancy system.

The results for the pure $MoSe_2$ and Mo vacancy systems are in close agreement with those reported by Vinturaj V. P. et al[26] It is also noteworthy that all refractive index values are relatively close, ranging between 2.08 and 3.38**.** The higher refractive index values indicate enhanced light-matter interaction, making these materials highly promising for

optoelectronicapplications. Additionally, the increase in the refractive index suggests improved optical performance[26], particularly in light absorption and transmission properties.

Table III-8 : Maximum values for refractive index and their corresponding energies in the (xx), (yy) and (zz) directions.

Structure	$n^{xx}(\omega)_{max}$	$n^{xx}(\omega)_{max}$ at energy (eV)	$n^{yy}(\omega)_{max}$	$n^{yy}(\omega)_{max}$ at energy (eV)	$n^{zz}(\omega)_{max}$	$n^{zz}(\omega)_{max}$ at energy (eV)
Pure $MoSe_2$	2,61	3,48	2,69	3,56	2,19	5,48
doped As(Mo)	2,32	3,96	3,38	3,96	2,08	5,46
Mo vacancy	2,44	2,49	2,42	2,40	2,09	5,91
Mo interstitial	2,45	2,87	2,52	2,87	2,10	4,87

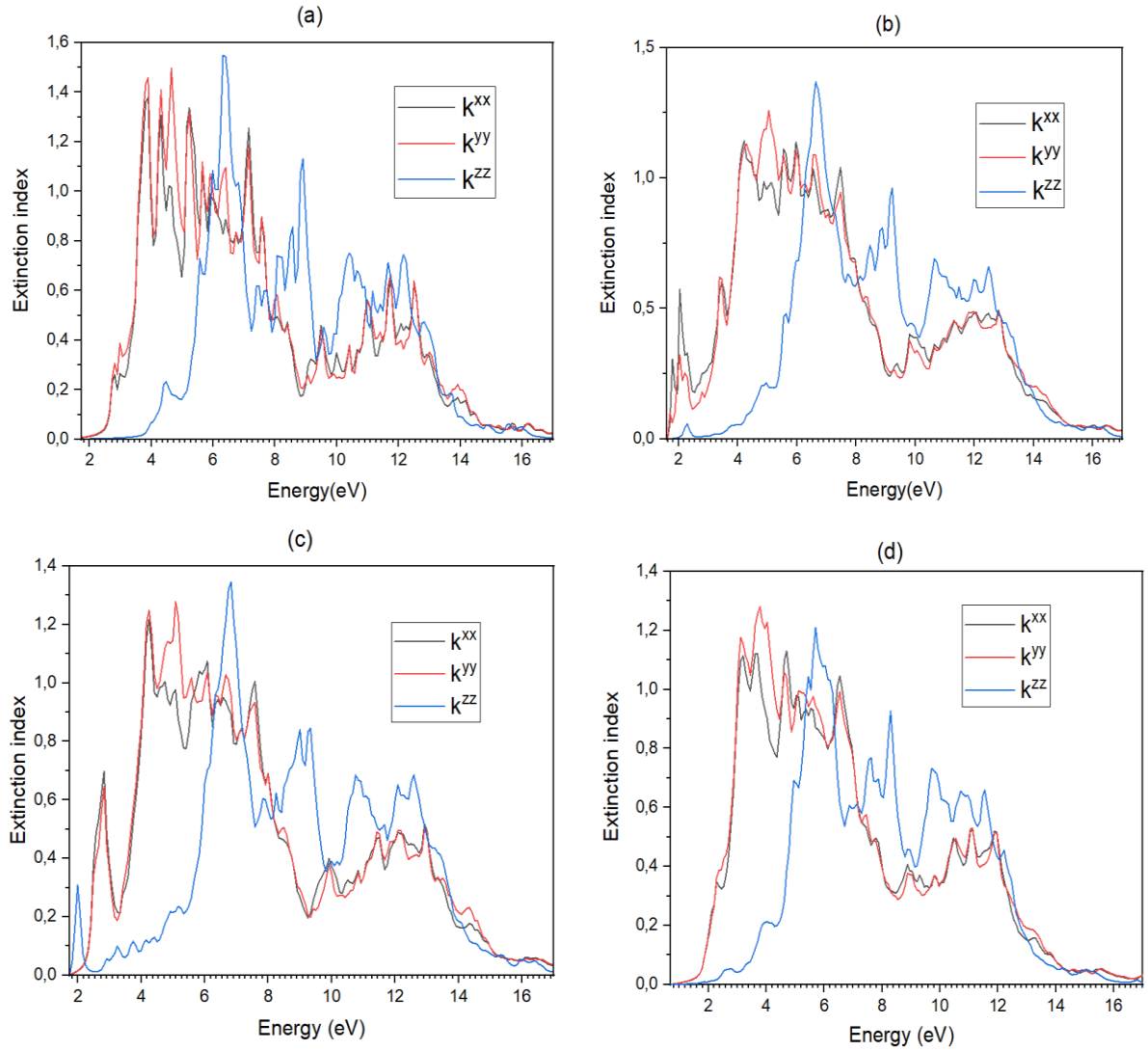


Figure III.19 : Extinction index as a function of photon energy of (a) pure $MoSe_2$ monolayer structure, (b) As(Mo)-doped structure, (c) Mo vacancy structure, and (d) As interstitial structure.

The extinction coefficient $k(\omega)$ called also the mass attenuation coefficient, the amount of absorption or attenuation of the photon is given by this coefficient, when light is propagated through the material [26, 56],The following equation establishes a direct relationship between the imaginary component of the dielectric function ε_i and the extinction coefficient $k(\omega)$ [60]:

$$k(\omega) = \frac{\lambda}{4\pi}\varepsilon_i(\omega) \qquad \text{(III-17)}$$

The **Figure III.19** illustrates the variation of the extinction coefficient $k(\omega)$ in as a function of photon energy (in eV) for all the studied cases.

We observe that these curves exhibit a similar shape to those of the imaginary part $\varepsilon_i(\omega)$ of the dielectric function, with more pronounced peaks, wich achieved the last relationship **(III-17).** The values of $k^{xx}(\omega)_{\max}$, $k^{yy}(\omega)_{\max}$, $k^{zz}(\omega)_{\max}$ along with their corresponding energies, are listed in **Table III-9**. Notably, the values of $k^{zz}(\omega)_{\max}$ and their corresponding energies are consistently higher than those of $k^{xx}(\omega)_{\max}$ and $k^{yy}(\omega)_{\max}$, except in the case of the interstitial system, where $k^{yy}(\omega)_{\max}$ is the highest. This indicates that photon absorption is most significant in the (zz) direction at higher energies[26].

For the interstitial system, the highest extinction coefficient is observed in the (yy) direction. Additionally, we note that the introduced defects lead to a decrease in the extinction coefficient values $k(\omega)$ compared to the pristine $MoSe_2$ monolayer, accompanied by a shift toward higher energies, except in the case of the interstitial As system, where shifts toward lower energies are observed in the (xx) and (yy) directions. These observations are in agreement with the study by Vinturaj V P et al [26]on the Mo vacancy system and the Nb-doped system, where it was found that the impurity peak in the Mo vacancy system has the highest extinction coefficient. However, the difference between our results and those of V. P. for the Mo vacancy system lies in the intensity of the first impurity peak, while they reported the first impurity peak as the most intense, in our calculations, a similar peak appears but it is not the highest one. The results for pure $MoSe_2$ are close to the experimental values reported by Liu Hsiang-Lin et al., who found a $k(\omega)_{\max}$ around 2 [57], and also in agreement with the theoretical results reported by Vinturaj V P et al where they found $k(\omega)_{\max} = 1.79$ [26].

Table III-9: Maximum values of and their corresponding energies in the (xx), (yy) and (zz)directions.

Structure	$k^{xx}(\omega)_{\max}$	$k^{xx}(\omega)_{\max}$ at energy (eV)	$k^{yy}(\omega)_{\max}$	$k^{yy}(\omega)_{\max}$ at energy (eV)	$k^{zz}(\omega)_{\max}$	$k^{zz}(\omega)_{\max}$ at energy (eV)
Pure $MoSe_2$	1,37	3,89	1,49	4,65	1,54	6,32
doped As(Mo)	1,14	4,21	1,25	5,04	1,36	6,63
Mo vacancy	1,21	4,24	1,27	5,07	1,34	6,83
As interstitial	1,12	4,70	1,27	3,78	1,21	5,70

Reflectivity $R(\omega)$ is one of the most significant optical properties that characterize materials, as it quantifies their optical response to incident light.It represents the ratio of the reflected light intensity to the incident light intensity $(\frac{I_r}{I_i})$ [61, 62], Mathematically, reflectivity is expressed by the following equation:

$$R(\omega)=\frac{(n(\omega)-1)^2+k(\omega)^2}{(n(\omega)+1)^2-k(\omega)^2} \quad \text{(III-18)}$$

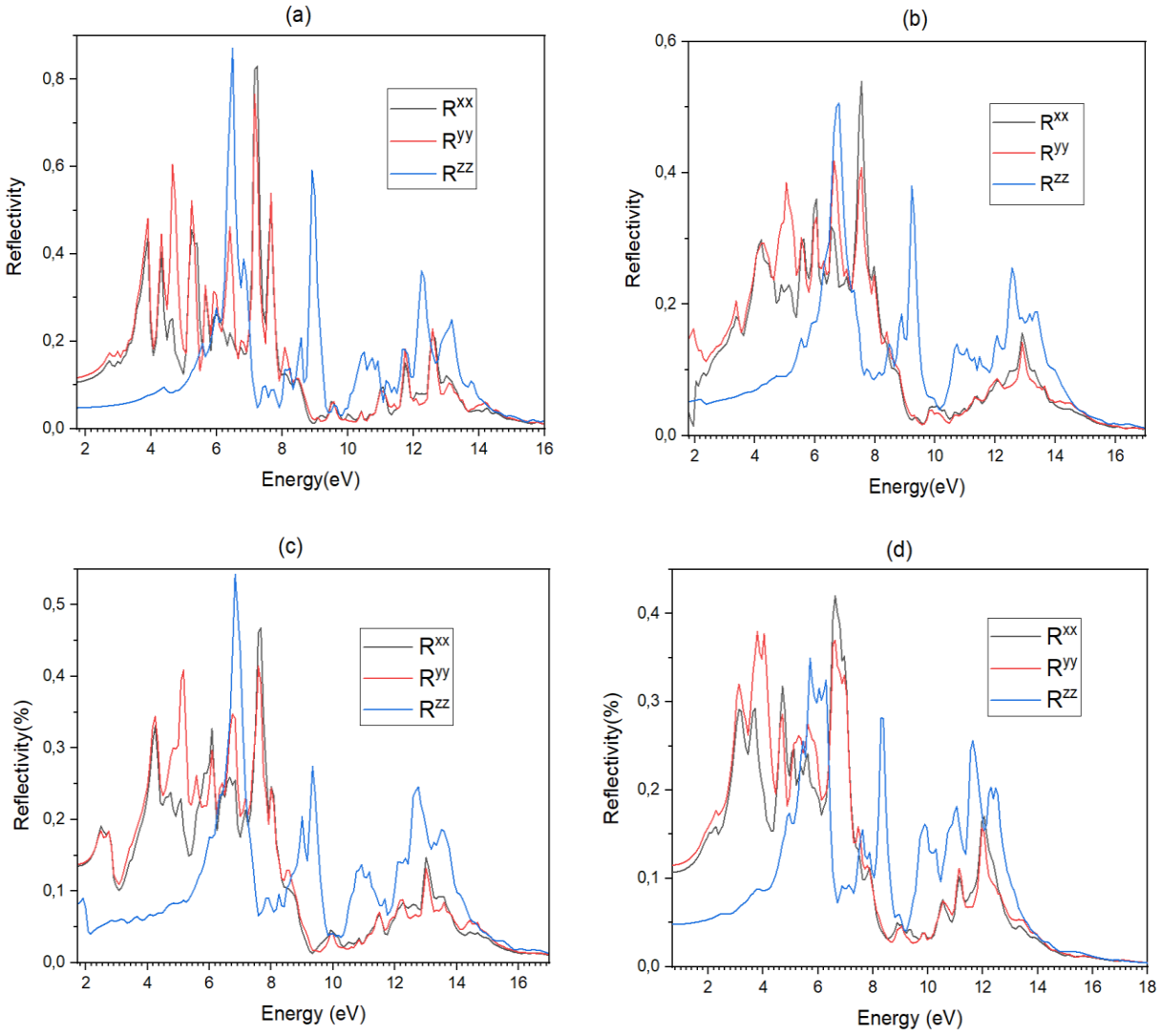


Figure III.20: Reflectivity of : (a) pure $MoSe_2$ monolayer structure, (b) doped As(Mo) structure, (c) Mo vacancy structure and (d) As interstitial structure.

The variation of reflectivity as a function of energy for our materials is shown in **Figure III.20.** First, we observe that the spectrum begins at the same threshold as the imaginary part of the dielectric function and the extinction coefficient, confirming the presence of optical transitions. The reflectivity spectrum exhibits strong peaks in the energy range of 2 eV to 9

eV for all structures, This range is consistent with other experimental [53,63,64]and theoretical[26]calculations reported in the literature, further validating the reliability of our results, indicating the presence of interband transitions in these regions.

Additionally, another set of peaks appears in the energy range of5 eV to 16 eV, but in the form of non-contiguous peaks, suggesting complex electronic transitions and possible contributions from higher-energy excitations.

The values of thestatic reflectivity $R(0)$, the most intense reflectivity peaks $R(\omega)_{max}$, and their corresponding energies are listed in Table III-10. We observe that $R(0)$ increases for systems containing defects. Additionally, the reflectivity in the zz-direction $R^{zz}(0)$ is consistently lower than $R^{xx}(0)$ and $R^{yy}(0)$ across all studied cases.Regarding impurity-containing structures, the reflectivity $R(\omega)_{max}$ decreases, while $R^{zz}(\omega)_{max}$ remains the highest, except in the case of the Asinterstitial system, where $R^{yy}(\omega)_{max}$ exhibits the largest value. Moreover, we find that $R(0)$ is inversely proportional to $R(\omega)_{max}$, highlighting the relationship between static reflectivity and peak reflectivity intensity.

Table III-10: Static reflectivity , maximum values of and their corresponding energies in the (xx), (yy) and (zz) directions.

Structure	$R^{xx}(0)$	$R^{xx}(\omega)_{max}$	$R^{xx}(\omega)_{max}$ at energy (eV)	$R^{yy}(0)$	$R^{yy}(\omega)_{max}$	$R^{yy}(\omega)_{max}$ at energy (eV)	$R^{zz}(0)$	$R^{zz}(\omega)_{max}$	$R^{ZZ}(\omega)_{max}$ at energy (eV)
Pure $MoSe_2$	10, 36 %	83%	7,23	11,35 %	76,6%	7,15	4,73 %	87,13%	6,48
doped As(Mo)	12,55 %	48,36 %	7,47	14,26 %	41,84%	6,63	5,19 %	50,63%	6,80
Mo vacancy	13,51 %	46,8%	7,66	13 ,78 %	41,41%	7,58	8,2%	54,28%	6,83
As interstitial	10,70 %	41,9%	6,62	11,5 %	38%	3,8	4,8%	34,96%	5,7

From **Table III-10**, we observe that the energies corresponding to the most intense reflectivity peaks fall within the range of 5.7 eV to 7.66 eV. However, for the interstitial structure**,** the highest peak occurs at 3.8 eV in the yy-direction, which lies outside this range.Notably, these peak energies fall within the ultraviolet (UV) region of the electromagnetic spectrum. In general, the average reflectivity values within the UV-visible spectrum indicate that the studied materials exhibit semi-transparency in this energy range[65].

Another important optical parameter is the absorption coefficient *α(ω)*, which quantifies the attenuation of light as it propagates through a material due to absorption. It determines the penetration depth of light at a specific wavelength before it is significantly absorbed. The absorption coefficient depends on both the material's electronic structure and the wavelength λ of the incident light. It can be derived from the extinction coefficient *k(ω)* using the following relation[66] :

$$\alpha(\omega) = \frac{4\pi k(\omega)}{\lambda} \quad \text{(III-19)}$$

FigureIII.21 illustrates the variation of the absorption coefficient as a function of energy for pure MoSe2 and its defective structures studied. The absorption coefficient curve increases from an energy threshold to a maximum value, after which the peaks slightly diverge for pure MoSe2. However, in the presence of defects, new peaks appear near the threshold energy. These peaks exhibit high intensity for $\alpha^{xx}(\omega)$ and $\alpha^{yy}(\omega)$ at approximately 2 eV for the As(Mo)-doped structure, 2.6 eV for the vacancy system, and 2.3 eV for the interstitial system, indicating additional electronic transitions between energy bands. Less intense peaks for $\alpha^{zz}(\omega)$ are also observed at 2.3 eV for the As(Mo)-doped system, 2 eV for the vacancy system, and 2.7 eV for the interstitial system. These energy values fall within the visible spectrum.

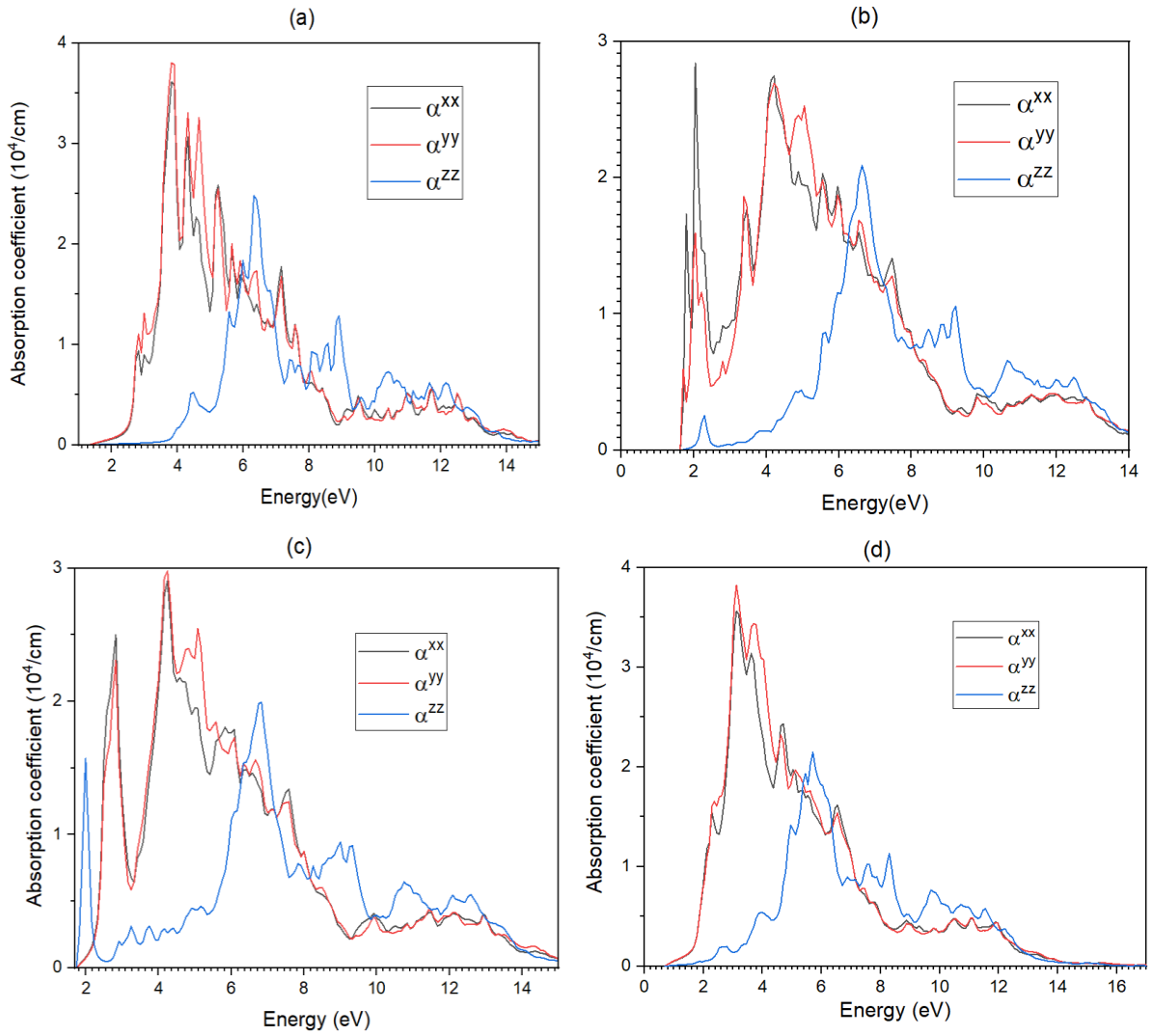


Figure III.21: Absorption coefficient of : (a) pure MoSe2 monolayer structure, (b) doped As(Mo) structure, (c) Mo vacancy structure (d) As Interstitial structure.

Table III-11 presents the absorption threshold values in the (xx), (yy), and (zz) directions, along with the electronic energy gap for pure MoSe2 and the studied defect structures. In general, we observe that the $\alpha^{xx}(\omega)$ and $\alpha^{yy}(\omega)$ absorption thresholds and the electronic bandgap are equivalent. Additionally, the absorption threshold increases in the presence of defects, except for the interstitial system, where a decrease is observed in the (xx) and (yy) directions. Notably, the absorption edges $\alpha^{zz}(\omega)$ are closely aligned with the calculated electronic bandgap. The absorption threshold obtained for pure $MoSe_2$ monolayer in our study is in close agreement with previous theoretical and experimental works, which reported values of 1.4 eV, 1.3 eV, 1.6 eV, and 1.1 eV by Yilei Li[53], Yuefeng Guo[39], Y. V. Morozov and M. Kuno[63], and Liu et al[57], respectively.

the maximum values of the absorption coefficient and their corresponding energies in the (xx), (yy), and (zz) directions for all studied systems are also listed, It is observed that the absorption $\alpha^{xx}(\omega)_{max}$ and $\alpha^{yy}(\omega)_{max}$ thresholds are equivalent, with values ranging between 3,03 eV and 4,24 eV, where these values are notably close for the doped As(Mo) and vacancy structures, whereas the maximum absorption coefficient $\alpha^{zz}(\omega)_{max}$ values range between 5.37 eV and 6.83 eV, Additionally, we observe that the absorption threshold, electronic bandgap, and maximum absorption coefficient shift towards higher energies for the doped As(Mo) and vacancy systems, a similar observation appears when MoS_2 is doped with Sb atom in Mo site[51], while they shift towards lower energies in the case of the interstitial system.

Table III-11: The absorption edge (threshold) in the (xx), (yy) and (zz) directions and the Energy gap (eV).

Structure	The absorption edge (threshold) $\alpha(\omega)$ in the directions (xx) and (yy) (eV)	The absorption edge (threshold) $\alpha(\omega)$ in the directions (zz) (eV)	Eg(eV)
Pure $MoSe_2$	1,31	1,39	1,41
doped As(Mo)	1,62	1,7	1,73
Mo vacancy	1,74	1,74	1,66
As interstitial	0,69	1,46	1,51

Table III-12 : Maximum values of and their corresponding energies in the (xx), (yy) and (zz) directions.

Structure	$\alpha^{xx}(\omega)_{max}$	$\alpha^{xx}(\omega)_{max}$ at energy (eV)	$\alpha^{yy}(\omega)_{max}$	$\alpha^{yy}(\omega)_{max}$ at energy (eV)	$\alpha^{zz}(\omega)_{max}$	$\alpha^{zz}(\omega)_{max}$ at energy (eV)
Pure $MoSe_2$	36138,19	3,81	38024,70	3,81	24826,28	6,32
doped As(Mo)	27462,68	4,21	26928,76	4,21	20893,57	6,63
Mo vacancy	29058,69	4,24	29788,95	4,24	19948,65	6,83
As interstitial	18660,70	3,03	211603,17	3,03	8,53	5,37

A similar trend can be observed in the optical conductivity $\sigma(\omega)$ curves shown in **Figure III.22**. Optical conductivity quantifies how a material responds to an external electromagnetic field in terms of electron mobility. This parameter describes interband transitions, where electrons in occupied states are excited to unoccupied states above the Fermi level upon photon absorption. This process leads to the generation of electrical conductivity in the presence of the electric field associated with the incident light. Optical conductivity is mathematically expressed by the following relation [67]:

$$\sigma = \frac{\alpha nc}{4\pi} \quad \text{(III-20)}$$

For the pristine $MoSe_2$ monolayer, our results are in good agreement with previous calculations that reported the optical conductivity in the energy range of 0 to 3 eV[53, 63].

In general, the presence of defects induces the emergence of new peaks in the UV-visible spectrum, particularly around2 eV, influencing key optical properties such as absorption, the extinction coefficient, and the imaginary part of the dielectric function. Furthermore, a pronounced optical response is observed in the UV-visible range (3–7 eV) along the xx andyy directions**,** as well as in the ultraviolet range (6–7 eV) along the zz direction.

These characteristics suggest that the studied materials hold significant potential for applications in photovoltaics, photocatalysis, and various optoelectronic technologies.

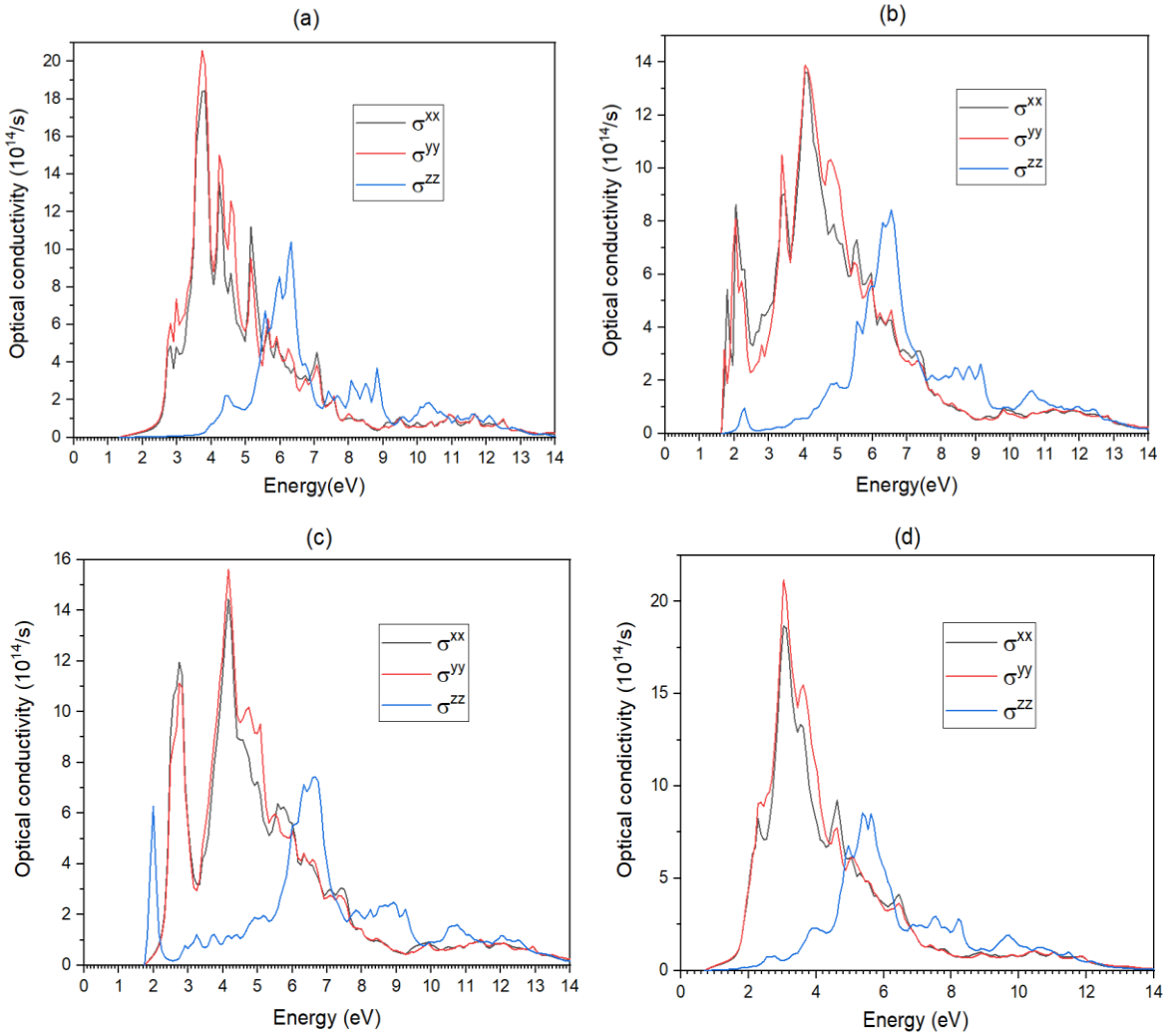


Figure III.22 : Optical conductivity of : (a) pure $MoSe_2$ monolayer structure, (b) doped As(Mo) structure, (c) Mo vacancy structure (d) As interstitial structure

Table III-13 : Maximum values of and their corresponding energies in the directions (xx), (yy) and (zz).

Structure	$L^{xx}(\omega)_{max}$	$L^{xx}(\omega)_{max}$ at energy (eV)	$L^{yy}(\omega)_{max}$	$L^{yy}(\omega)_{max}$ at energy (eV)	$L^{zz}(\omega)_{max}$	$L^{zz}(\omega)_{max}$ at energy (eV)
Pure $MoSe_2$	2,13	12,74	2.05	12,66	3,75	13,24
doped As(Mo)	1,88	13,05	1,71	12,98	2,80	13,47
Vacuancy in Mo	1,68	13,09	1,60	13,09	2,80	13,67
InterstitialAs	2,03	12,30	1,81	12,05	3,17	12,55

Finally, in **Figure III.23**, we present the energy loss function $L(\omega)$ of both pristine and defected $MoSe_2$ monolayers, analyzed along the (xx), (yy), and (zz) crystallographic directions.This parameter reflects the energy loss experienced by fast electrons traversing the material[56, 68].

Notably, electrons lose energy when their energy slightly exceeds the optical band gap, which is approximately 1.8 eV for pure $MoSe_2$ monolayer. In defected structures, additional low-intensity peaks emerge near this threshold energy, attributable to defect-induced states.

Across all studied structures, a prominent resonance peaks are observed in the 12–14 eV range, similar energy ranges have been reported in the studies of Yuefeng Guo et al[39] and Vinturaj, V. P et al [26].

However, the intensity and sharpness of peak in the mentioned range vary slightly, indicating strong UV-range plasmonic behavior. The highest peaks and their corresponding energies for the different structures are detailed in **Table III-13**.

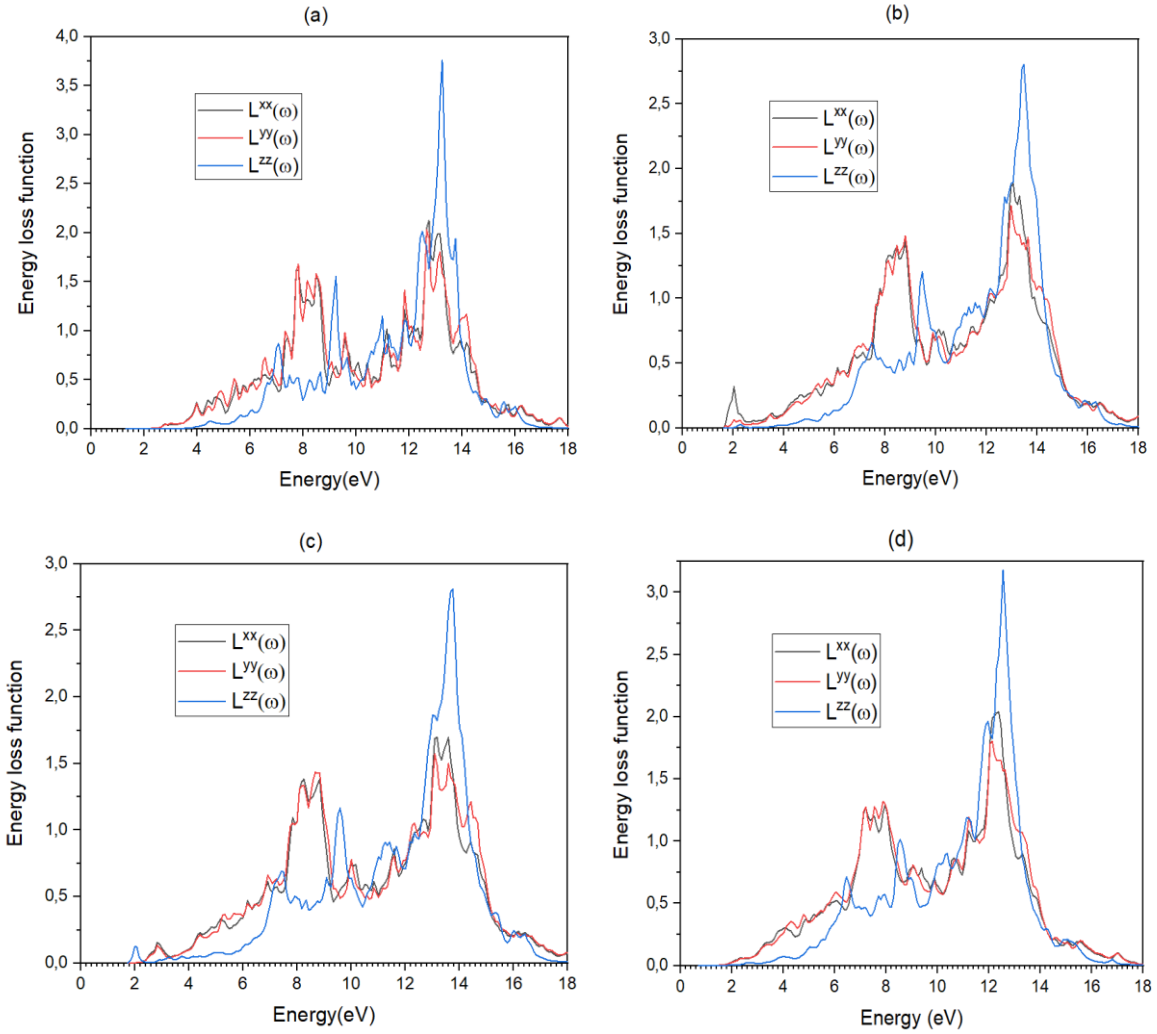


Figure III.23: Energy loss function of : (a) pure MoSe2 monolayer structure, (b) doped As(Mo) structure, (c) Mo vacancy structure (d) As interstitial.

Table III-13 indicates that introducing arsenic (As) atoms as defects in $MoSe_2$ monolayers affects the material's plasmonic resonance peaks.

Specifically, when an As atom substitutes a molybdenum (Mo) atom or when a Mo vacancy is present, the highest resonance peaks decrease in intensity and shift towards higher energies. The calculated energy loss features are also in close agreement with those reported by Vinturaj, V. P et al[26] and Yuefeng Guo[39]. Furthermore for Mo vacancy systeme, for the As-doped structure, we observe the same behavior found in Sb(Mo)-doped MoS_2 system[51].

Conversely, introducing an As atom into an interstitial site causes the highest resonance peak to shift towards lower energies. Additionally, the longitudinal component along the z-axis exhibits the most pronounced resonance peaks across all configurations, suggests that the plasmonic oscillations are more strongly coupled in this direction.Generally,the resonance peaks occur in ultraviolet for pure $MoSe_2$ monolayer and in ultraviolet and visible in impurity systems.

References

[1] P. Giannozzi *et al.*, "QUANTUM ESPRESSO: A modular and open-source software project for quantum simulations of materials," *J. Phys. Condens. Matter*, vol. 21, no. 39, 2009, doi: 10.1088/0953-8984/21/39/395502.

[2] J. P. Perdew, K. Burke, and M. Ernzerhof, "Generalized Gradient Approximation Made Simple," no. 3, pp. 3865–3868, 1996.

[3] H. J. Monkhorst and J. D. Pack, "Special points for Brillouin-zone integrations," *Phys. Rev. B*, vol. 13, no. 12, pp. 5188–5192, Jun. 1976, doi: 10.1103/PhysRevB.13.5188.

[4] F. D. Murnaghan, "The Compressibility of Media under Extreme Pressures," *Proc. Natl. Acad. Sci.*, vol. 30, no. 9, pp. 244–247, Sep. 1944, doi: 10.1073/pnas.30.9.244.

[5] J. A. Wilson and A. D. Yoffe, "The transition metal dichalcogenides discussion and interpretation of the observed optical, electrical and structural properties," *Adv. Phys.*, vol. 18, no. 73, pp. 193–335, 1969, doi: 10.1080/00018736900101307.

[6] G. Lucovsky, R. M. White, J. A. Benda, and J. F. Revelli, "Infrared-Reflectance Spectra of Layered Group-IV and Group-VI Transition-Metal Dichalcogenides," *Phys. Rev. B*, vol. 7, no. 8, pp. 3859–3870, Apr. 1973, doi: 10.1103/PhysRevB.7.3859.

[7] R. B. Murray and A. D. Yoffe, "The band structures of some transition metal dichalcogenides: Band structures of the titanium dichalcogenides," *J. Phys. C Solid State Phys.*, vol. 5, no. 21, pp. 3038–3046, 1972, doi: 10.1088/0022-3719/5/21/009.

[8] M. G. Menezes and S. Ullah, "Unveiling the multi-level structure of midgap states in Sb-doped MoX 2 (X = S, Se, Te) monolayers," vol. 2, pp. 1–16, 2021.

[9] Z. Luo, J. Hao, and J. Li, "The optical properties of MoSe2 in bulk and monolayer with different crystal orientation based on first-principles calculations," vol. 3, no. 1, pp. 51–57, 2022, doi: 10.25236/AJMC.2022.030109.

[10] E. D. Hanson *et al.*, "Phase engineering and optical properties of 2D MoSe 2 : Promise and pitfalls," *Mater. Chem. Phys.*, vol. 225, no. November 2018, pp. 219–226, 2019, doi: 10.1016/j.matchemphys.2018.11.069.

[11] X. Guan, G. Zhu, X. Wei, and J. Cao, "Tuning the electronic properties of monolayer MoS2, MoSe2 and MoSSe by applying z-axial strain," *Chem. Phys. Lett.*, vol. 730, no. March, pp. 191–197, 2019, doi: 10.1016/j.cplett.2019.06.007.

[12] Y. Ding, Y. Wang, J. Ni, L. Shi, S. Shi, and W. Tang, "First principles study of structural, vibrational and electronic properties of graphene-like MX2 (M=Mo, Nb, W, Ta; X=S, Se, Te) monolayers," *Phys. B Condens. Matter*, vol. 406, no. 11, pp. 2254–

2260, May 2011, doi: 10.1016/j.physb.2011.03.044.

[13] S. Haldar, H. Vovusha, M. K. Yadav, O. Eriksson, and B. Sanyal, "Systematic study of structural, electronic, and optical properties of atomic-scale defects in the two-dimensional transition metal dichalcogenides," *Phys. Rev. B*, vol. 92, no. 23, p. 235408, Dec. 2015, doi: 10.1103/PhysRevB.92.235408.

[14] S. Prucnal *et al.*, "Chlorine doping of $MoSe_2$flakes by ion implantation," *Nanoscale*, vol. 13, no. 11, pp. 5834–5846, 2021, doi: 10.1039/d0nr08935d.

[15] H. P. Komsa, N. Berseneva, A. V. Krasheninnikov, and R. M. Nieminen, "Charged point defects in the flatland: Accurate formation energy calculations in two-dimensional materials," *Phys. Rev. X*, vol. 4, no. 3, 2014, doi: 10.1103/PhysRevX.4.031044.

[16] H. Mehdipour and P. Kratzer, "Structural defects in a Janus MoSSe monolayer: A density functional theory study," *Phys. Rev. B*, vol. 106, no. 23, pp. 1–17, 2022, doi: 10.1103/PhysRevB.106.235414.

[17] Y. Zhao, W. Wang, C. Li, and L. He, "First-principles study of nonmetal doped monolayer $MoSe_2$ for tunable electronic and photocatalytic properties," *Sci. Rep.*, vol. 7, no. 1, pp. 1–8, 2017, doi: 10.1038/s41598-017-17423-w.

[18] A. Kumara and P. K. Ahluwalia, "Electronic structure of transition metal dichalcogenides monolayers 1H-MX_2 (M = Mo, W; X = S, Se, Te) from ab-initio theory: New direct band gap semiconductors," *Eur. Phys. J. B*, vol. 85, no. 6, pp. 18–22, 2012, doi: 10.1140/epjb/e2012-30070-x.

[19] J. Gusakova *et al.*, "Electronic Properties of Bulk and Monolayer TMDs: Theoretical Study Within DFT Framework (GVJ-2e Method)," *Phys. Status Solidi Appl. Mater. Sci.*, vol. 214, no. 12, pp. 1–7, 2017, doi: 10.1002/pssa.201700218.

[20] W. Li, C. F. J. Walther, A. Kuc, and T. Heine, "Density Functional Theory and Beyond for Band-Gap Screening: Performance for Transition-Metal Oxides and Dichalcogenides," *J. Chem. Theory Comput.*, vol. 9, no. 7, pp. 2950–2958, Jul. 2013, doi: 10.1021/ct400235w.

[21] L. A. H. Jones *et al.*, "Band Alignments, Electronic Structure, and Core-Level Spectra of Bulk Molybdenum Dichalcogenides (MoS_2 , $MoSe_2$, and $MoTe_2$)," *J. Phys. Chem. C*, vol. 126, no. 49, pp. 21022–21033, Dec. 2022, doi: 10.1021/acs.jpcc.2c05100.

[22] T. Böker *et al.*, "Band structure of MoS_2, $MoSe_2$and α-$MoTe_2$ Angle-resolved photoelectron spectroscopy and ab initio calculations," *Phys. Rev. B - Condens. Matter Mater. Phys.*, vol. 64, no. 23, pp. 1–11, 2001, doi: 10.1103/PhysRevB.64.235305.

[23] A. Kormányos *et al.*, " K · P Theory for Two-Dimensional Transition Metal Dichalcogenide Semiconductors ," *2D Mater.*, vol. 2, no. 2, p. 022001, 2015, doi: 10.1088/2053-1583/2/2/022001.

[24] X. Lu *et al.*, "Large-Area Synthesis of Monolayer and Few-Layer MoSe 2 Films on SiO 2 Substrates," *Nano Lett.*, vol. 14, no. 5, pp. 2419–2425, May 2014, doi: 10.1021/nl5000906.

[25] J. Wang, R. Zhao, M. Yang, Z. Liu, and Z. Liu, "Inverse relationship between carrier mobility and bandgap in graphene," *J. Chem. Phys.*, vol. 138, no. 8, Feb. 2013, doi: 10.1063/1.4792142.

[26] V. P. Vinturaj *et al.*, "Theoretical investigation of electronic and optical properties of doped and defective $MoSe_2$ monolayers," *Bull. Mater. Sci.*, vol. 46, no. 3, 2023, doi: 10.1007/s12034-023-02963-x.

[27] J.-J. Ma, J.-J. Zheng, W.-D. Li, D.-H. Wang, and B.-T. Wang, "Thermal transport properties of monolayer MoSe 2 with defects," *Phys. Chem. Chem. Phys.*, vol. 22, no. 10, pp. 5832–5838, 2020, doi: 10.1039/D0CP00047G.

[28] C. Middleton, B. F. E. Curchod, and T. J. Penfold, "Partial density of states representation for accurate deep neural network predictions of X-ray spectra," *Phys. Chem. Chem. Phys.*, vol. 26, no. 37, pp. 24477–24487, 2024, doi: 10.1039/D4CP01368A.

[29] A. Ramasubramaniam, "Large excitonic effects in monolayers of molybdenum and tungsten dichalcogenides," *Phys. Rev. B*, vol. 86, no. 11, p. 115409, Sep. 2012, doi: 10.1103/PhysRevB.86.115409.

[30] Y. Zhang *et al.*, "Direct observation of the transition from indirect to direct bandgap in atomically thin epitaxial $MoSe_2$," *Nat. Nanotechnol.*, vol. 9, no. 2, pp. 111–115, Feb. 2014, doi: 10.1038/nnano.2013.277.

[31] M. Zhong *et al.*, "Electronic structure and exciton shifts in Sb-doped MoS_2 monolayer," *npj 2D Mater. Appl.*, vol. 3, no. 1, p. 1, Jan. 2019, doi: 10.1038/s41699-018-0083-1.

[32] A. I. Ayesh, "H2S and SO2 adsorption on Cu doped MoSe2: DFT investigation," *Phys. Lett. A*, vol. 422, p. 127798, Jan. 2022, doi: 10.1016/j.physleta.2021.127798.

[33] Y. Zhao *et al.*, "High response and broadband photodetection by monolayer $MoSe_2$ with vanadium doping and Mo vacancies," *Appl. Surf. Sci.*, vol. 564, p. 150399, Oct. 2021, doi: 10.1016/j.apsusc.2021.150399.

[34] B. Balasubramaniam, N. Singh, P. Kar, A. Tyagi, J. Prakash, and R. K. Gupta,

"Engineering of transition metal dichalcogenide-based 2D nanomaterials through doping for environmental applications," *Mol. Syst. Des. Eng.*, vol. 4, no. 4, pp. 804–827, 2019, doi: 10.1039/C8ME00116B.

[35] R. Hou, Y. Xia, and S. Yang, "A Linear Relationship between the Charge Transfer Amount and Level Alignment in Molecule/Two-Dimensional Adsorption Systems," *ACS Omega*, vol. 5, no. 41, pp. 26748–26754, Oct. 2020, doi: 10.1021/acsomega.0c03719.

[36] Z. Cui, X. Wang, Y. Ding, C. Zhang, and M. Li, "Alkali-metal-embedded in monolayer MoS_2: optical properties and work functions," *Opt. Quantum Electron.*, vol. 50, no. 9, pp. 1–12, 2018, doi: 10.1007/s11082-018-1612-z.

[37] A. V. Kolobov, P. Fons, J. Tominaga, and S. R. Ovshinsky, "Vacancy-mediated three-center four-electron bonds in GeTe-Sb_2Te_3 phase-change memory alloys," *Phys. Rev. B*, vol. 87, no. 16, p. 165206, Apr. 2013, doi: 10.1103/PhysRevB.87.165206.

[38] D. Su *et al.*, "First-principles study of the effect of doping on the optoelectronic properties of defective monolayers of MoSe2," *J. Mol. Model.*, vol. 30, no. 2, p. 29, Feb. 2024, doi: 10.1007/s00894-023-05826-8.

[39] Y. Guo, Y. Ji, H. Dong, L. Wang, and Y. Li, "Electronic and optical properties of defective MoSe 2 repaired by halogen atoms from first-principles study," *AIP Adv.*, vol. 9, no. 2, 2019, doi: 10.1063/1.5068712.

[40] E. Blokker, X. Sun, J. Poater, J. M. van der Schuur, T. A. Hamlin, and F. M. Bickelhaupt, "The Chemical Bond: When Atom Size Instead of Electronegativity Difference Determines Trend in Bond Strength," *Chem. - A Eur. J.*, vol. 27, no. 63, pp. 15616–15622, 2021, doi: 10.1002/chem.202103544.

[41] A. Abbasi and J. J. Sardroodi, "Adsorption of O3, SO2 and SO3 gas molecules on MoS2 monolayers: A computational investigation," *Appl. Surf. Sci.*, vol. 469, pp. 781–791, Mar. 2019, doi: 10.1016/j.apsusc.2018.11.039.

[42] T. Liu, Z. Cui, X. Li, H. Cui, and Y. Liu, "Al-Doped $MoSe_2$Monolayer as a Promising Biosensor for Exhaled Breath Analysis: A DFT Study," *ACS Omega*, vol. 6, no. 1, pp. 988–995, 2021, doi: 10.1021/acsomega.0c05654.

[43] T. C. L. Paul M. Chaikin, *Principles of Condensed Matter Physics*. Cambridge University Press,1955, 1995.

[44] N. R. W Tang, SS Rassay, "Electronic and optical properties of transition-metal dichalcogenides," *Madridge J. Nanotechnol. Nanosci*, vol. 2, pp. 58--64, 2017.

[45] D. Lee, A. M. Johnson, J. E. Zucker, C. A. Burrus, R. D. Feldman, and R. F. Austin,

"High-Temperature Quasi-Continuous Operation of Optically Pumped CdZnTe/ZnTe Multiple-Quantum-Well Lasers at 620 nm," *IEEE Photonics Technol. Lett.*, vol. 4, no. 9, pp. 949–951, 1992, doi: 10.1109/68.157111.

[46] E. W. Max Born, *Principles of Optics*, 6th ed. Elsevier, 2013.

[47] C. Kittel, *Physique de l'état solide*, Ed. Dunod. 1983.

[48] F. Abelés, *Optical Properties of Solids*. North-Holland: North-Holland Pblishing Company, 1972.

[49] R. Troć, "US: Optical Conductivity and Dielectric Function," no. 2, pp. 496–504, 2009, doi: 10.1007/978-3-540-47043-4_73.

[50] "Optical properties measurement techniques solar energy materials special issue," *Sol. Energy Mater.*, vol. 18, no. 3–4, p. 231, Mar. 1989, doi: 10.1016/0165-1633(89)90057-9.

[51] Z. Cui, M. Li, E. Li, D. Ma, and B. Zhao, "First-principles study of antimony-doped monolayer molybdenum disulfide: Electronic structure and optical properties," *Phys. E Low-Dimensional Syst. Nanostructures*, vol. 104, pp. 91–97, 2018, doi: 10.1016/j.physe.2018.07.015.

[52] J. Quereda, T. S. Ghiasi, F. A. Van Zwol, C. H. Van Der Wal, and B. J. Van Wees, "Observation of bright and dark exciton transitions in monolayer $MoSe_2$ by photocurrent spectroscopy," *2D Mater.*, vol. 5, no. 1, 2018, doi: 10.1088/2053-1583/aa8aa0.

[53] Y. Li, "Measurement of the Optical Dielectric Function of Monolayer Transition Metal Dichalcogenides: MoS_2, $MoSe_2$, WS_2, and WSe_2," pp. 33–43, 2016, doi: 10.1007/978-3-319-25376-3_5.

[54] T. J. Kim, H. G. Park, V. L. Le, H. T. Nguyen, X. A. Nguyen, and Y. D. Kim, "Parameterized optical properties of monolayer $MoSe_2$," *AIP Adv.*, vol. 9, no. 12, 2019, doi: 10.1063/1.5125973.

[55] M. N. Bui *et al.*, "Optical Properties of $MoSe_2$ Monolayer Implanted with Ultra-Low-Energy Cr Ions," *ACS Appl. Mater. Interfaces*, vol. 15, no. 29, pp. 35321–35331, 2023, doi: 10.1021/acsami.3c05366.

[56] A. M. Shawahni *et al.*, "Structural, elastic, electronic and optical properties of SrTMO3 (TM = Rh, Zr) compounds: Insights from FP-LAPW study," *Materials (Basel).*, vol. 11, no. 10, pp. 1–19, 2018, doi: 10.3390/ma11102057.

[57] H. L. Liu, C. C. Shen, S. H. Su, C. L. Hsu, M. Y. Li, and L. J. Li, "Optical properties of monolayer transition metal dichalcogenides probed by spectroscopic ellipsometry,"

Appl. Phys. Lett., vol. 105, no. 20, 2014, doi: 10.1063/1.4901836.

[58] C. Hsu *et al.*, "Thickness-Dependent Refractive Index of 1L, 2L, and 3L MoS_2, $MoSe_2$, WS_2, and WSe_2," *Adv. Opt. Mater.*, vol. 7, no. 13, 2019, doi: 10.1002/adom.201900239.

[59] Y. Li *et al.*, "Measurement of the optical dielectric function of monolayer transition-metal dichalcogenides: MoS_2, $MoSe_2$," *Phys. Rev. B*, vol. 90, no. 20, p. 205422, Nov. 2014, doi: 10.1103/PhysRevB.90.205422.

[60] F. Wooten, *Optical Properties of Solids*. Elsevier, 1972. doi: 10.1016/C2013-0-07656-6.

[61] A. Shrivastava, S. Saini, and S. Singh, "Ab-Initio investigations of electronic and optical properties of Sn-hBN hetero-structure," *Phys. B Condens. Matter*, vol. 624, p. 413390, 2022, doi: 10.1016/j.physb.2021.413390.

[62] C. F. Matta and R. J. Gillespie, "Understanding and interpreting molecular electron density distributions," *J. Chem. Educ.*, vol. 79, no. 9, p. 1141, 2002, doi: 10.1021/ed079p1141.

[63] Y. V. Morozov and M. Kuno, "Optical constants and dynamic conductivities of single layer MoS2, MoSe2, and WSe2," *Appl. Phys. Lett.*, vol. 107, no. 8, pp. 3–8, 2015, doi: 10.1063/1.4929700.

[64] A. R. Beal and H. P. Hughes, "Kramers-Kronig analysis of the reflectivity spectra of 2H-MoS_2, 2H-$MoSe_2$ and 2H-$MoTe_2$," *J. Phys. C Solid State Phys.*, vol. 12, no. 5, pp. 881–890, 1979, doi: 10.1088/0022-3719/12/5/017.

[65] REGGAD Abderrahmane, "Etude par calcul AB-INITIO des propriétes structurales et optoelectroniques des Bismuthinite Bi_2S_3," 2013.

[66] A. N. Pikhtin and D. A. Yaskov, "Infrared Absorption in Gallium Phosphide," *Phys. Status Solidi*, vol. 34, no. 2, pp. 815–824, 1969, doi: 10.1002/pssb.19690340244.

[67] J. R. Schrieffer, "Why Manganites Are Interesting," 2003, pp. 1–8. doi: 10.1007/978-3-662-05244-0_1.

[68] H. K. Neupane and N. P. Adhikari, "Structure, electronic and magnetic properties of 2D Graphene-Molybdenum diSulphide (G-MoS_2) Heterostructure (HS) with vacancy defects at Mo sites," *Comput. Condens. Matter*, vol. 24, p. e00489, 2020, doi: 10.1016/j.cocom.2020.e00489.

Conclusion

Conclusion

In this research, we investigated the structural, electrical, and optical characteristics of monolayer molybdenum diselenide ($MoSe_2$) as a member of the transition metal dichalcogenides (TMDCs) of group VI, using first-principles calculations based on density functional theory (DFT). Our goal was to analyze the impact of intrinsic defects and atomic substitutions on the material's behavior for potential applications in nanoelectronics, optoelectronics, and other fields.

Our findings indicate that the structural parameters of pristine $MoSe_2$ are well-represented by DFT calculations, showing consistency with both experimental and theoretical references. The Murnaghan equation was used to optimize structural parameters such as the lattice parameter, bulk modulus, and its derivative.

The total energy was evaluated as a function of volume, and the optimal lattice constant was determined accordingly. Importantly, our calculations suggest that the overall lattice structure remains mostly unchanged upon doping or defect introduction. However, defects such as Mo vacancy, As(Mo) doping, and As interstitial atoms were analyzed. We calculated formation energies in Se-rich conditions and found that the As(Mo)-doped system is likely to form, whereas the As interstitial system is unlikely to form and is metastable.

After analyzing the band structure, density of states (DOS), and projected density of states (PDOS) of several systems, we found impurity levels near the band edges.

We interpreted these states based on the contribution of orbitals responsible for their formation.

To better understand the bonding behavior in pure and defective $MoSe_2$, we studied charge density differences. Our charge density maps indicated significant charge redistribution near defect sites, highlighting localized bonding effects. Arsenic substitution resulted in charge concentration near the dopant atom, suggesting stronger covalent bonding, whereas interstitial arsenic caused charge delocalization, influencing the surrounding electronic environment. These findings align with the modifications observed in the band structure and density of states.

To study the optical properties, we analyzed the dielectric function, refractive index, extinction coefficient, reflectivity, absorption coefficient, optical conductivity, and energy loss function. These characteristics were examined along the (xx), (yy), and (zz) directions for both pristine and defective structures. Our optical analysis demonstrated that pristine MoSe2 exhibits strong absorption in the visible and ultraviolet ranges. The presence of defects led to distinct modifications in the dielectric function and other optical characteristics. Notably, new peaks appeared, especially in the visible range, suggesting that $MoSe_2$'s optical response can

be tuned for specific applications such as solar cells and catalysts. In general, defect introduction caused a redshift in absorption peaks, highlighting the potential of defect engineering in tailoring the optical properties of $MoSe_2$. In particular, interstitial arsenic defects introduced additional localized states, further enhancing the material's optical tunability.

This study contributes to the broader understanding of TMDCs, particularly in the context of defect engineering.

By systematically analyzing the effects of vacancies, substitutions, and interstitial defects, our research provides valuable insights into the design of two-dimensional materials with tailored structural, electronic, and optical properties.

Our findings encourage further studies on similar defect-induced modifications in other TMDCs to expand our understanding of these materials. Investigating more complex defect configurations and employing machine learning techniques for property prediction may open new possibilities for optimizing material performance, especially in the field of nanomaterials, which is currently one of the most interesting topics in materials physics.